asurements
m
tellite
tforms

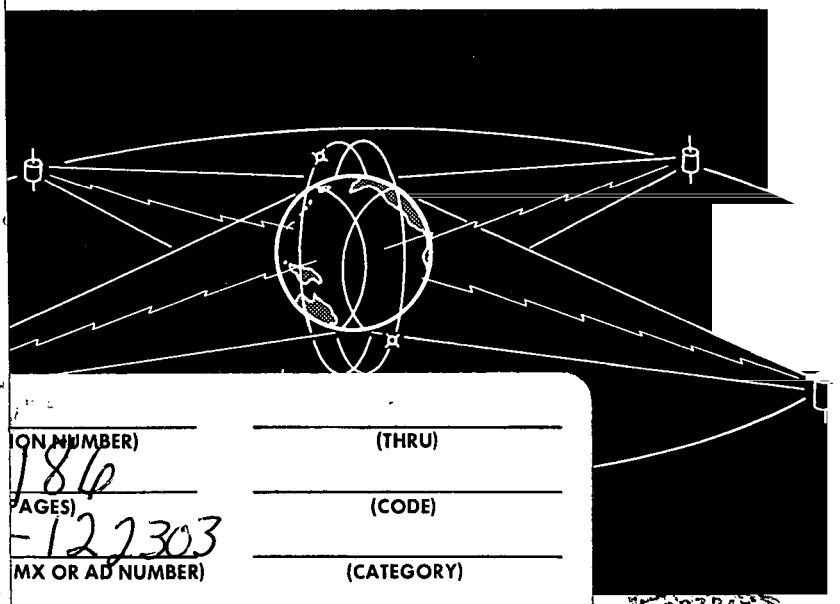

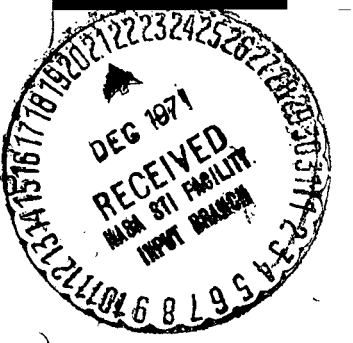

Annual Scientific Report on NAS5-11542, 1969-70

Space Science and Engineering Center
The University of Wisconsin-Madison
Madison, Wisconsin, August 1971

COVER DRAWING

The cover drawing, first used on a series of reports by COSPAR WG6, has become symbolic of a global satellite system for meteorological purposes. We chose this cover since all of our research work reported in this document is closely related to the objectives of the Global Atmospheric Research Program.

Space Science and Engineering Center,
The University of Wisconsin,
Madison, Wisconsin

METEOROLOGICAL MEASUREMENTS FROM SATELLITE PLATFORMS

Annual Scientific Report

on

NAS5-11542

1969-1970

The research in this document has been supported in whole or in part by the National Aeronautics and Space Administration.

August 1971

PRINCIPAL INVESTIGATORS

Verner E. Suomi
Thomas H. Vonder Haar

CONTRIBUTIONS BY

Anderson C. E.
Grosh R.
Hasler F.
Krauss R.
Levanon N.
Miller J. G.
Sikdar D. N.
Smith E.
Stamm A.
Stremler F.
Suomi V. E.
Vonder Haar T.

University of Wisconsin

PREFACE

As indicated by the cover photo of this report, our research has focused strongly on viable segments of a global meteorological observing system.

In addition to the contributions contained in this document, our research team is continuing to experiment with an optimum wind-finding system for geostationary satellite data application as well as with further development of the geostationary temperature sounder concept. The next report will summarize results in these areas.

All scientists and students associated with our projects deserve great thanks for their diligent efforts, innovative ideas and boundless enthusiasm. We thank especially Mr. Harold Oxley for his aid in preparing this report.

Verner E. Suomi
Thomas H. Vonder Haar

Principal Investigators

CONTENTS

RECENT DEVELOPMENTS IN SATELLITE TECHNIQUES FOR OBSERVING AND SENSING THE ATMOSPHERE

V. E. Suomi
University of Wisconsin

1. Introduction

This report on satellite techniques for observing the atmosphere must be dated August 1969. Progress in using these platforms to obtain the observations needed for the Global Atmospheric Research Programme (GARP) has been so rapid that one must be sure to give the month as well as the year of the report.

The requirements of the Global Observing System (GOS) necessary for GARP are given in the report of the Study Conference, Stockholm (GARP, 1967), and in reports prepared by COSPAR Working Group VI (1969).* These parameters and the current estimate of accuracy required are presented in Table 1. One needs the mass, motion and moisture field as functions of x, y, p and t. $(x_1, y_1)(x_2, y_2)$ and so on are points in the numerical model's grid mesh and $p_1, p_2 \ldots p_n$ are the levels in the vertical pressure coordinate. Global data of this density are required to specify the initial conditions in the model's synthetic data bank and for updating the model's data as its prediction departs from the observations of the world's weather.

Studies (Mintz 1967) have shown that the mass field, obtained by temperature measurements in the atmosphere and the pressure at a reference level, are by far the most important. Through the use of the model itself, one can predict the motion field very well, at least, down to subtropical latitudes.

---

*The COSPAR Working Group VI Report to JOC is now published as GARP Publication No. 2, "Systems possibilities for an early GARP experiment," January 1969. There is also an excellent summary in NCAR Facilities, Pub. No. 10, September 1969.

Table 1

Global Observing System (GOS) Requirements

Atmospheric state parameter	Accuracy r. m. s. error
$T(x, y, p, t)$(temperature)	$\pm$ 1°C
$V(x, y, p, t)$(wind)	$\pm$ 3 m/sec
$q_V(x, y, p, t)$ water vapour	10%
$P_0(x, y, t)$ at reference level	0·2-0·3% (3 mb at s. f. c.)
Horizontal resolution	every 400 km × 400 km (global)
Vertical resolution	8 layers (s. f. c. -10 mb)
	50 m, 1 km
	10, 50, 100 mb
	200, 500, 700 mb
Frequency	at least once per day.

2. Satellite Temperature Soundings Using Upwelling IR Methods

The outstanding success of the IR vertical temperature sounding experiments on the United States Satellite NIMBUS III (Wark and Hilleary (1969) and Hanel, R. (personal communication)) early this year is an exceedingly important breakthrough in our ability to provide the key global observations so vital to GARP. A detailed report on this exciting development has been given by D. Q. Wark, R. A. Smith, D. G. James and H. E. Fleming at this conference. Figure 1 is a reproduction of the very first sounding obtained using the observations of the IR grating spectrometer on NIMBUS III by Wark and his collaborators. It is included here because of its historic importance. Figure 2 is the first IR spectrum obtained by Hanel and his collaborators using the IR interferometer spectrometer also carried on NIMBUS III. It, also, is historic, because it can be used to infer the vertical moisture structure as well as the vertical temperature structure. It is also possible to infer a simple ozone profile.

These instruments are yielding vertical temperature profiles in clear air columns slightly more accurate (Wark and Fleming (1966)) than their developers were willing to predict before the flight. The results are much better than was thought possible during partly cloudy conditions. With these errors which are slightly less than 1.0°C r.m.s., we can consider the effects of the errors on predictability.

Figure 3 shows the growth of the r.m.s. temperature error for an initial error of 0.5°C expressed as the standard deviation in the nine-level model developed by Smagorinsky and his collaborators (1969) at ESSA's Geophysical Fluid Dynamics Laboratory. A 0.5°C initial error was used in the numerical

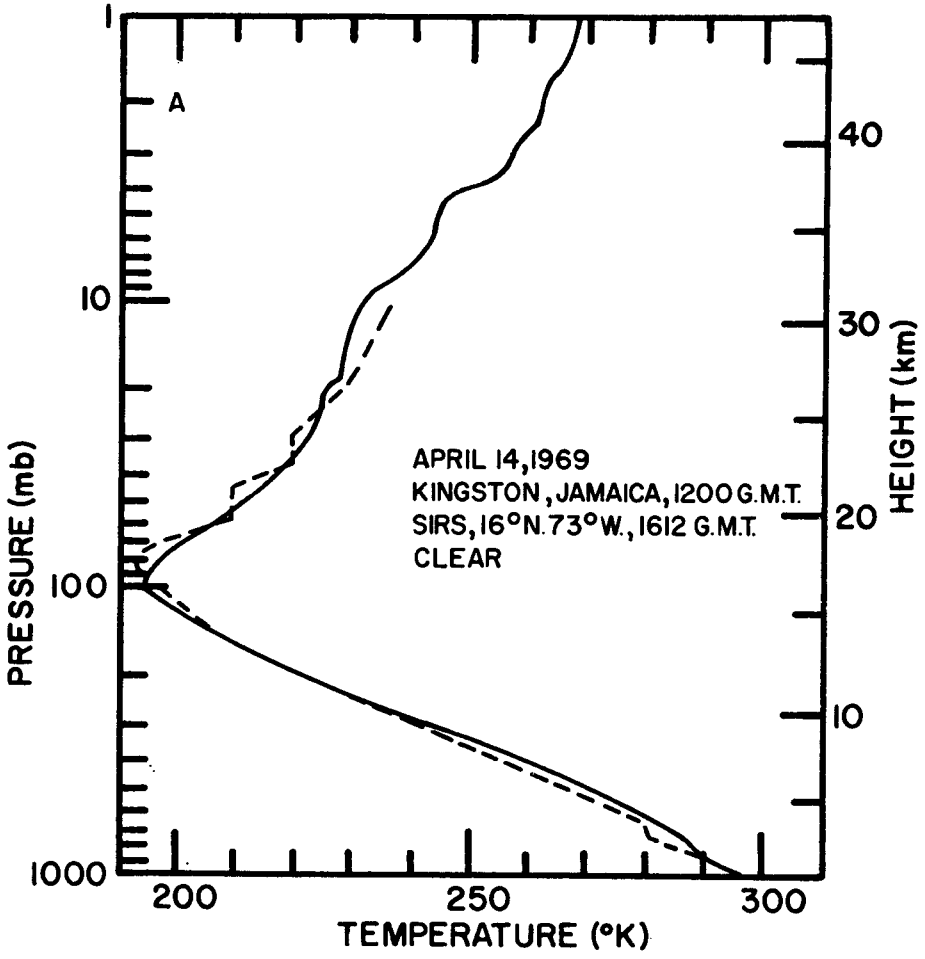

Fig. 1. Historical first sounding derived from satellite measurements. Dotted line is radiosonde derived temperature. SIRS instrument.

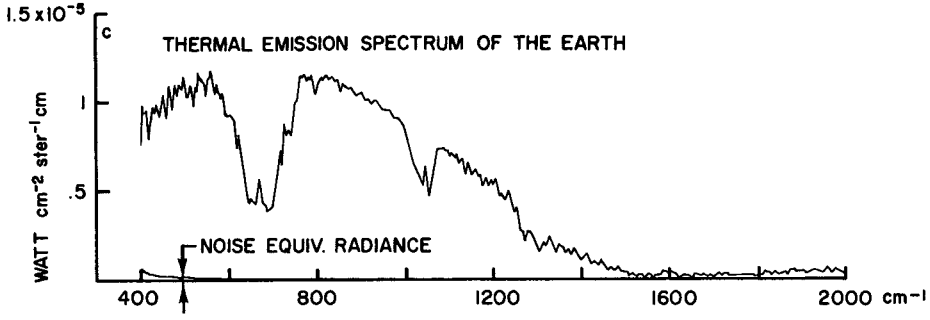

Fig. 2. First Fourier transform derived spectrum from satellite interferometer spectrometer. IRLS instrument.

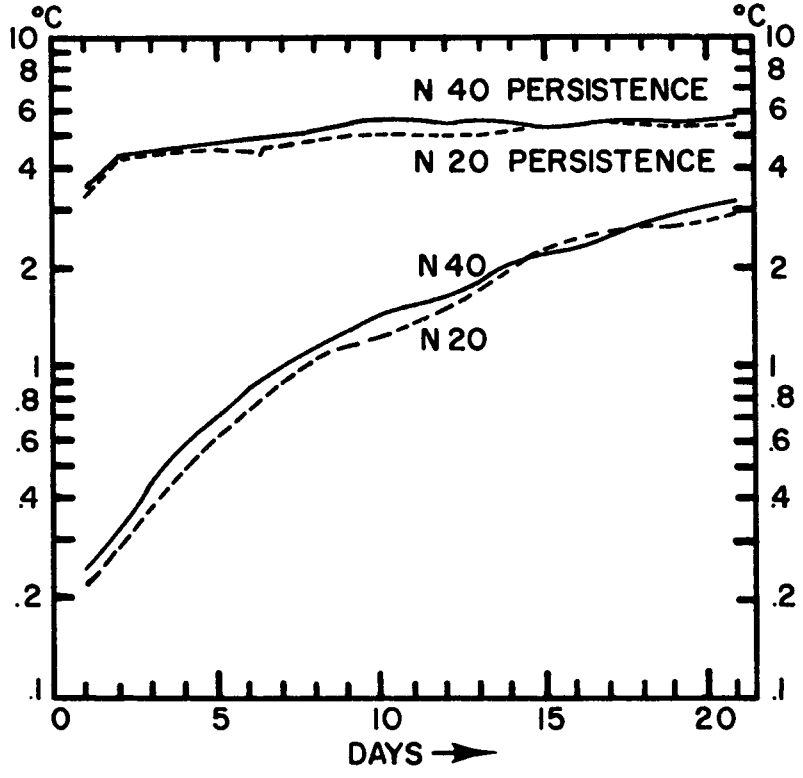

Fig. 3. Root mean square error for initial error of 0.5°C (Smagorinsky)

simulation experiment. The IR sounder's error is currently about twice as great. After an initial adjustment period of one day, the r.m.s. error in the model reduces to 0.25°C then grows with a doubling time of two days from 0.25°C to 0.5°C. The doubling time increases to seven days while the error grows from 1.0°C to 2.0°C. Experiments like this one and others using the Mintz-Arakawa model (as described in 1966 in Publication No. 1290, National Academy of Sciences, National Research Council, Washington) form the basis of the so-called "two-week prediction" stated as a goal for GARP. If the initial error cannot be reduced below the current estimate of about 1.0°C r.m.s., a significant fraction of the two-week prediction capability will be lost. While the present satellite IR temperature sounding capability does not meet the 0.5°C error limit used in the numerical experiment, it is nevertheless a very impressive beginning.

3. Balloon Radio Altimeter

In order to specify the mass field, the pressure at a reference level is needed in addition to the vertical temperature profile. Ordinarily, this is satisfied with observations of sea-level pressure using the conventional network or the observations from ships at sea. These observations are probably adequate for a large part of the globe, particularly in the Northern Hemisphere. However, in the Southern Hemisphere, very large gaps in the surface-net exist. The COSPAR Working Group VI report to JOC (1969) suggests that this gap can be filled through the use of horizontally floating superpressure balloons and suggests that a key technical element is the development of a lightweight low-power radio altimeter which would make it possible to measure the pressure at a known geometrical altitude above the sea surface. An accuracy of $\pm$ 10 meters would be required.

This development has been successfully accomplished by Levanon, Suomi and Stremler (1970) at the University of Wisconsin. Their tiny radio altimeter consists of a superregenerative receiver which also acts as the pulse transmitter.

Since the speed at which radio waves travel is known precisely, it is possible to determine the geometrical altitude accurately from the time it takes a radio-frequency pulse to travel to the ocean and return. The radio altimeter transmits about 30,000 pulses per second. The return signal is averaged for about one second for each measurement. A phase-locked loop system is used to control the pulse repetition frequency, so its period matches the period required for the signal to make the round trip. Harmonic operation where several spaced pulses are on their way to the ocean and back is used to improve the sensitivity. Figure 4 illustrates the principle of operation.

The performance of the radio altimeter exceeds the stated requirements of $\pm$ 10 m. During the flight tests on a radiosonde balloon flight, the error was

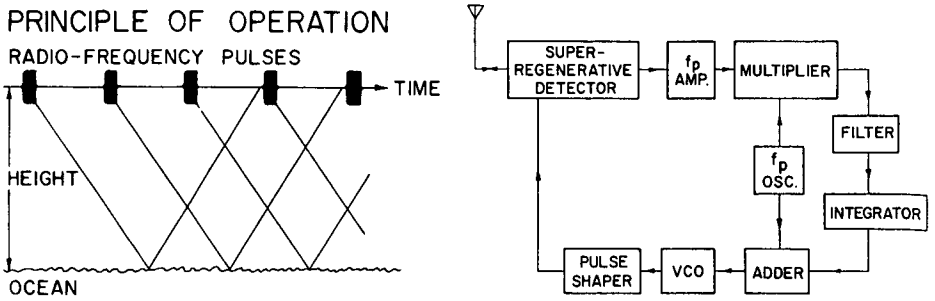

Fig. 4. Radio altimeter principle of operation

± 7 m, but this error includes the error due to pendulum action of the balloon train and also includes an error due to nonsynchronous timing with the small perturbation frequency needed for the phase-locked loop.

When these errors are removed, the height error is more like ± 1 m, if the integration time is about four seconds. Figure 5 shows two flight tests, the first on a radiosonde balloon, the second on a GHOST-type balloon. The latter flight, which was carried out by Lally (private communication, 1969) and his collaborators, was compared with ground-based precision tracking radar. It is clear that as the range distance increased, the altitude error of the ground-based radar increased. This was found to be due to a slight misalignment in the levelling of the ground-based radar-antenna platform. Figure 6 is an illustration of one of the first flight models. The electronics package weighs 130 g, the antenna another 40 g and the device requires one watt of power.* Use of additional integrated circuits will make possible a further weight reduction, but probably not any substantial power reduction. If a GHOST balloon is equipped with a sensitive pressure altimeter, it will serve as a reference surface.

It is easy to show that since a balloon floats with the wind, one equipped with both pressure and radio altimeter can be used to measure the ageostrophic wind directly.

---

*Two new transistor models have since been developed. One operates at 405 mc, the other at 1,680 mc. Their performance is about two times better than the model illustrated.

The 1-watt power consumption is for continuous operation. In actual use, a much lower duty cycle would suffice—say one minute out of each 100. Thus, a 10 mW continuous power load is more appropriate.

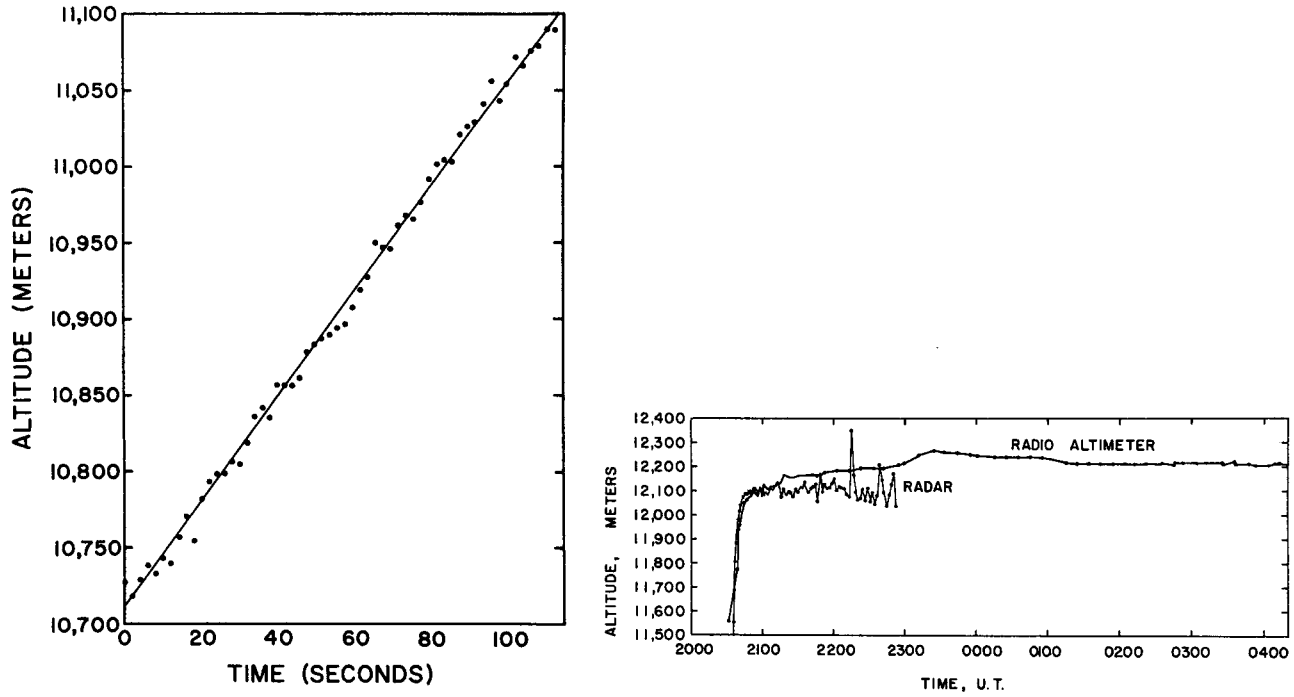

Fig. 5. Flight tests radiosonde ascent and comparison with radar using superpressure GHOST balloon

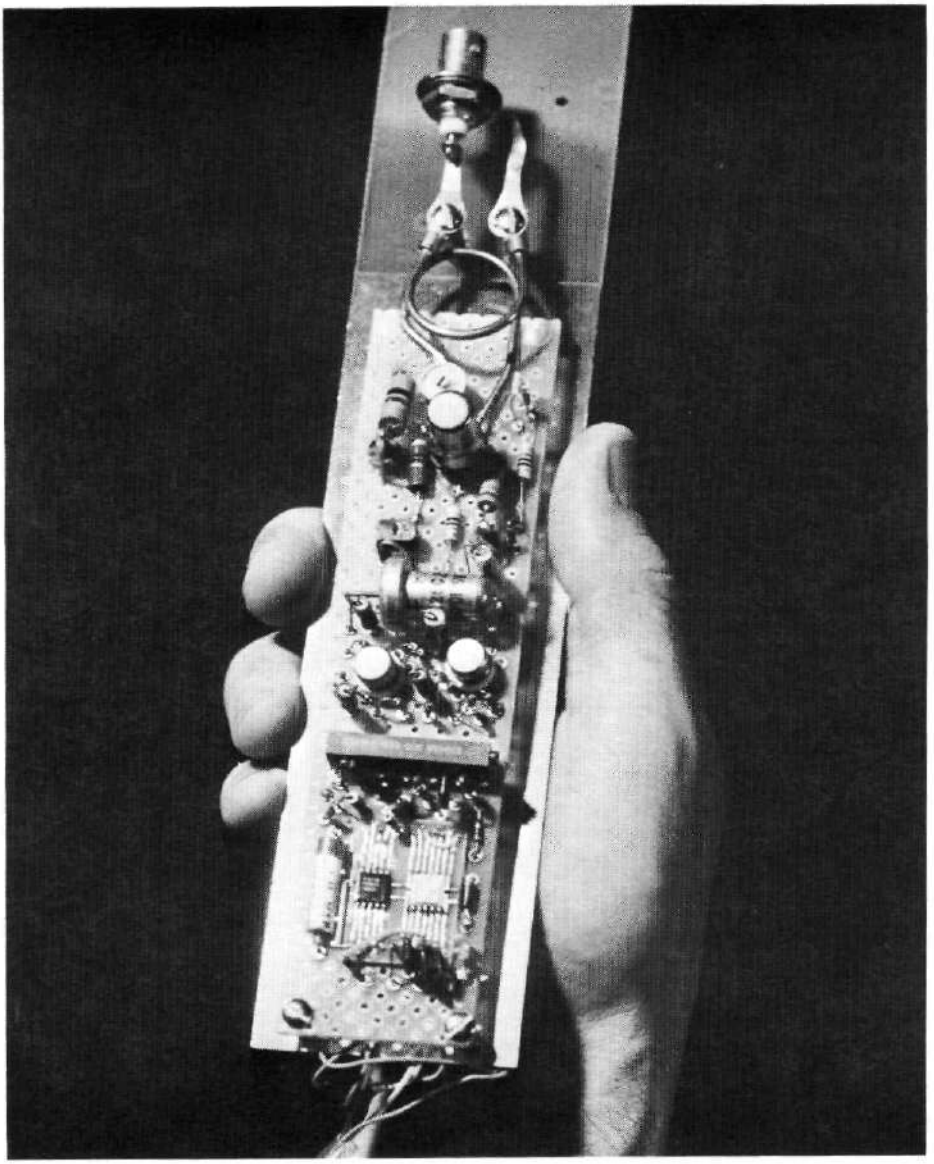

Fig. 6. Radio altimeter instrument

Thanks to the work of Lally (1969) in the United States, and Morel (1966) in France, we now know that superpressure balloons can be made to fly with lifetimes approaching a year, if the flight altitudes are in the stratosphere. Thus, the superpressure balloons can obtain the winds and also serve as a reference level. Unfortunately, experience has shown that because of icing, long balloon-lifetime does not seem possible when operating in the troposphere. The short-lifetime of GHOST-type balloons in the troposphere places an economic limit on their use for wind finding at tropospheric levels.

4. Wind from Cloud Motions

The writer first proposed the use of cloud motion as seen from a geostationary satellite as a means for determining winds, in the American Meteorological Society's Wexler Memorial Lecture (Harry Wexler's Weather World) Jan. 1967. Using this type of spacecraft, the clouds moved—not the satellite. At that lecture, the audience was shown a time lapse movie of cloud motion for 7 and 8 January 1967 using the photographs obtained from the spin-scan camera on ATS-I over the Central Pacific; with the time speed-up factor near 10,000, the cloud motion was easy to see. The audience was provided with polarizing spectacles so that two images of the earth taken at different times could be seen as a single three-dimensional image. In this arrangement, clouds moving in the westerlies appear above the earth's surface at an altitude proportional to their motion. Similarly, clouds moving in the easterlies appear below the earth's surface at a depth proportional to their motion. Many methods (Johnson 1968; Fujita, 1968; Hubert and Whitney, 1970; Hasler, 1970) can be used to measure the cloud displacements. Figure 7 illustrates the alignment steps and several methods for obtaining the cloud motion. In almost all instances, the imaging accuracy is not limited by the spin-scan camera itself, but by the apparatus used to reconstruct the images at the ground station. Another limitation results from the inability to identify easily a position in the image with its exact location on the earth. This task is comparatively easy to do manually, but is time consuming in a computer. Figures 8(a) and (b) show cloud motion for typical GARP grids over the Pacific obtained using computer developed mosaics (Vonder Haar, T. and Stamm, A., Internal report, Space Science and Engineering Center, University of Wisconsin). The figure in the bracket gives the number of individual measurements used to get the mean value for the grid point. It is clear that hundreds of individual observations of cloud motion are available and many more clouds could have been used. A key question remains, however—"How high are the clouds?"

5. IR Images from Geostationary Altitude

Images of the earth cloud systems using the spin-scan cameras on ATS-I and ATS-III are limited to daylight hours and thus the observations are not truly continuous. In addition, except possibly near the terminator zone, there is

WINDS FROM CLOUD MOTION

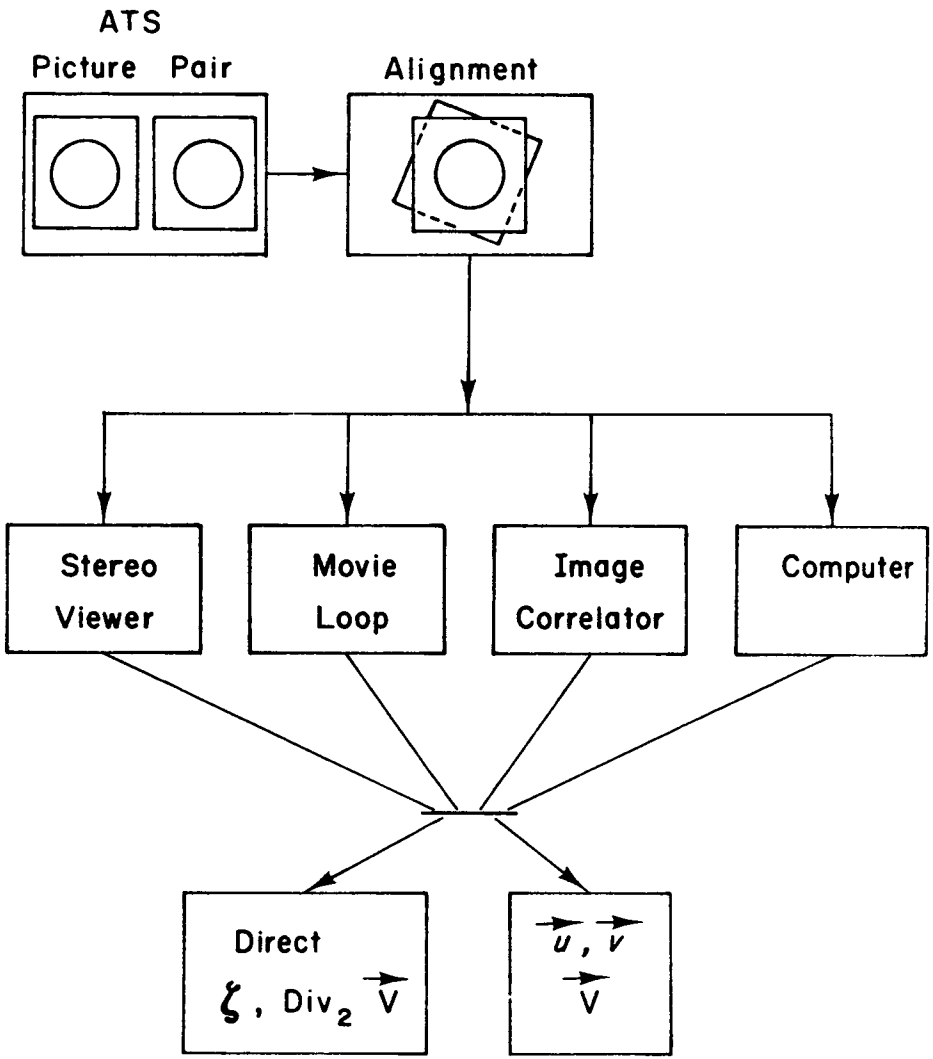

Fig. 7. Image alignment steps and methods of obtaining winds

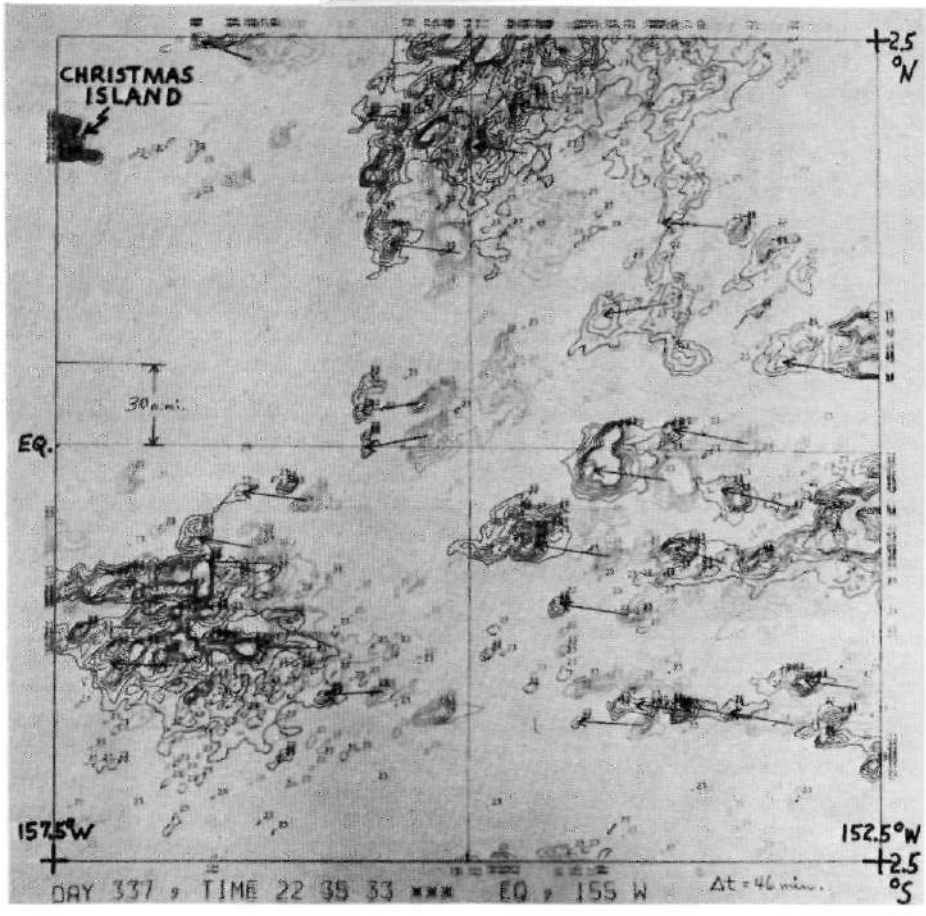

Fig. 8(a). Computer derived winds

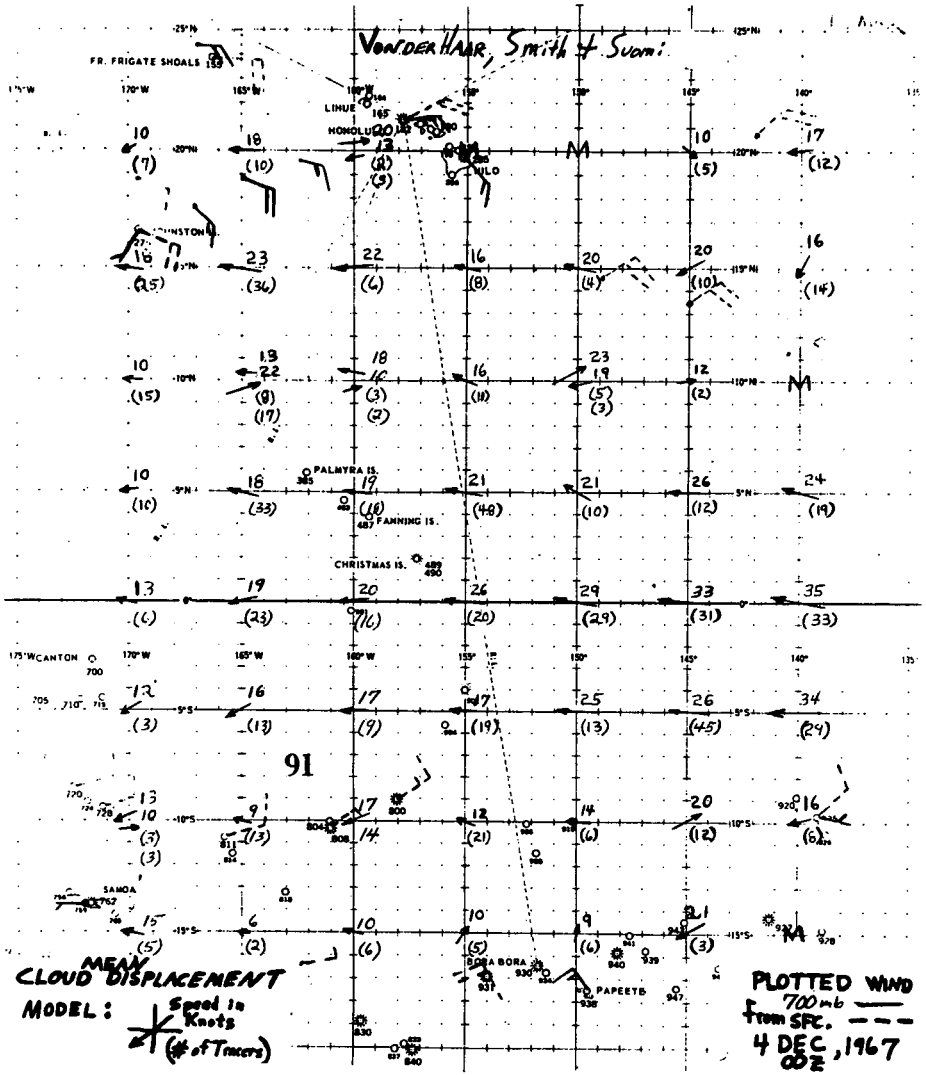

Fig. 8(b). Computer derived winds

Table 2

Long Wavelength Infrared Camera (LWIRC) Parameters

Telescope type	Ritchey-Chrétien
Aperture diameter	16 in.
Primary mirror	f/1.8 aspheric
Secondary mirror	4.8 in. diameter aspheric
Equivalent focal length	48 in. (f/3)
Effective aperture area	1.2×10^3 cm^2
Optical efficiency at 11μ (including plane scan mirror)	0.88
Field of view	0.2 mr
Modulation transfer function (Diffraction at 11μ, 0.07 mr aberration and mounting tolerance, and 0.2 mr field stop)	0.58
Latitude scan	Plane object-space mirror
Steps (full earth)	1,600 ± 50
Relay	Two germanium lenses
Entrance focal ratio	f/3
Exit focal ratio	f/2
Optical efficiency at 11μ	0.71
Overall equivalent focal length	32 in.
Detector	
Size	0.16 mm × 0.16 mm
Spectral bandpass	10.5 to 12.6μ
Nominal temperature	77°K
Minimum average detectivity over Δλ	1.4×10^{10} cm Hz$^{1/2}$ watt^{-1} (f/2 cold shield and cold filter)
Filter transmittance	0.65
Cooling	Two-stage radiator
Temperature	70°K
Signal processing	
Preamplifier noise factor	1.4
IFOV dwell time	1.9×10^{-5} sec at 100 rpm spin rate
Information bandwidth	0.1 Hz (double section filter-2% droop max.) to 26 kHz (two 40 kHz sections)

Table 2 (continued)

Signal processing (cont.)	
Equivalent noise bandwidth	56 kHz (including 1/f and generation-recombination noise)
Peak-to-steady state waveform factor	0.8
Performance	
Noise equivalent temperature difference*	5.5°K (for 200°K scene) 1.5°K (for 300°K scene)
Weight and power	
Sensor weight	117 lb
Electronics module	5 lb
Peak power	18 watt
Average power	8 watt

*Note: For 0.3 mr IFOV the NEΔT becomes: 3.1°K at 200°K
0.88°K at 300°K

little information about a cloud's altitude. This is an important deficiency in the approach which attempts to use cloud motion as a wind indicator. Studies by Hummer at Santa Barbara Research Center (in 1968) show that a spin-scan camera system operating in the ten- to twelve-micron region is possible, providing large optics (16 in. diameter primary mirror) and sensitive cooled detectors are used. Figure 9 illustrates the optical arrangement proposed. The axis of the IR telescope and the spin axis of the spacecraft are the same. In this scheme, the north-south line scan is provided by a 45°flat mirror which tilts in small uniform steps as the spacecraft spins. Table 2 gives some of the key specifications of the IR camera system. A camera system similar to this is currently being considered as part of the United States contribution to the Global Observing System. It is scheduled for launch in 1972. With such an IR imaging capability, it is possible to estimate the temperature and thus the altitude. Since one measures IR energy and not temperature, it is also necessary to know the cloud emissivity. The uncertainties in cloud emissivity, particularly for cirrus clouds (Kuhn, 1970), may seriously limit the real altitude resolution capability.

6. IR Soundings from Geostationary Altitude

Studies at the University of Wisconsin by Suomi, Krauss and Vonder Haar (1969) show that IR soundings can be obtained with the large IR telescope just described. However, the measurement of infrared radiance from the earth's atmosphere in narrow wavelength bands good enough to infer the vertical

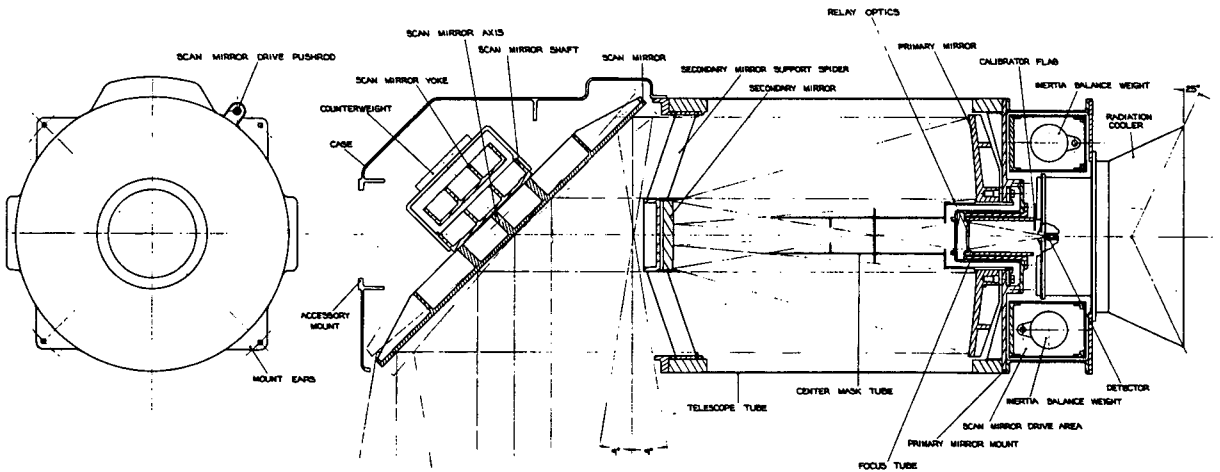

Fig. 9. Long-wavelength infrared camera (LWIRC) layout drawing

temperature profile from geostationary altitude is difficult, owing to the low energy levels encountered. At 35,800 km, random noise from the radiation detector is a large fraction of the signal from the atmosphere. Given a large optical system and very sensitive detector, we can overcome this energy deficiency by using multiple sampling in space, time or both. Too-long integration times must not be used, however, since the parameter of interest, atmospheric temperature, varies with time. Proper space sampling must also be insured since temperature varies with space as well. Despite these difficulties, the effort may be worthwhile because the atmosphere is a four dimensional system (x, y, p and t) and a continuous view adds the dimension time. To be useful the atmosphere must be sounded with an error less than 1.0°C.

One way to reduce the error is to restrict the observations to clear areas only. Thus only clear column radiances are used to reconstruct the temperature profile and errors due to the presence of cloud are removed. The NIMBUS III results are very impressive even including cloud in the field-of-view, but few would argue that the presence of cloud contributes to higher accuracy.

The central question of our study may be stated as follows. Each radiance observation will be contaminated by detector noise and may also be contaminated by "cloud noise." With a large instantaneous field of view (IFOV), it is not possible to separate the detector noise from the cloud noise. With a small IFOV, one can separate the "cloud noise" which is not random from the detector noise, which is. However, this can only be done at the price of a poorer signal-to-noise ratio. Are there enough additional clear column samples using a small IFOV to improve the S/N ratio to acceptable levels? The answer depends on the performance specifications of the instrument and on the natural occurrence of clouds.

Measurements from the NIMBUS experiments have shown that the magnitude of infrared radiance near the 15 micrometer CO_2 band varies from 50 to 110 erg cm^{-2} sec^{-1} sr^{-1} cm from band center to edge during clear sky conditions' over most of the region viewed from a geostationary satellite. These same experiments obtained measurements with relative accuracies of about 0.25 erg cm^{-2} sec^{-1} sr^{-1} cm. Vertical temperature profiles with an r.m.s. error of 1°C were obtained from them.

Several important options determine the performance of the instrument. One of the most important is the instantaneous field of view of the telescope-(IFOV).

Meteorological spacecraft configurations used in the study include:

(a) a spin-scan instrument system

(b) 16 in. optics

(c) spin rate of 100 r.p.m.

(d) cooled HgCdTe infrared detectors (near 11 micrometers for imaging; and near 14 micrometers for sounding).

Figure 10 shows how the IFOV α, error and area which must be sampled are related. If we use 0.25 erg cm^{-2} sec^{-1} sr^{-1} cm as an appropriate error limit and a 10 km resolution at NADIR, almost 10^5 sq km clear area would be required or more than 50% of a 400 km × 400 km GARP grid. On the other hand, if 15 km resolution at NADIR were used, only 15% clear area in a GARP grid would be required.

Now, since high resolution IR images are desired, the resolution for this wide spectral interval detector will be more like 6 km or 7 km at NADIR. These small steps will yield additional overlapping lines of the sounding channels. The time required to obtain a clear column radiance as a function of cloudiness is given in Table 3.

Table 3

Time Required to Obtain a Clear Column Radiance as a Function of Cloudiness

Cloud Cover (percent)	Number of completed frames	Time (sec) for sounding IR
99	11	2.88
95	3	0.79
70	2	0.52
50	1	0.26
Clear	1	0.26

Studies of ATS-I cloud data currently underway indicate that 15 km - 20 km openings in the cloud deck are optimum also. Thus, it appears that continuous soundings of the atmosphere's vertical temperature structure even in the presence of substantial clouds are feasible. Figure 11 shows a typical view of the cloud cover of the earth as seen from geostationary altitude. The numbered squares are areas where the cloud statistics were investigated in order to determine the time needed for sounding the atmosphere. Squares numbered row 4, column 4 and row 5, column 3, 4, 5 of matrix 1 are the only ones where no sounding was possible in a reasonable time. Squares numbered row 4, column 4 and row 5, column 5 of matrix 1 had complete cloud cover, and soundings only down to the cloud cover are available in these locations.

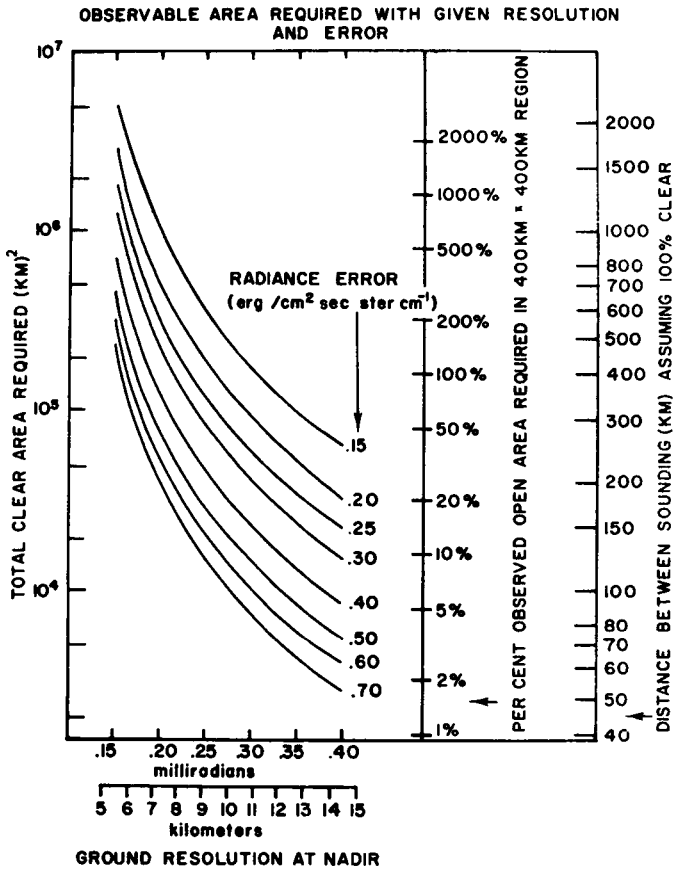

Fig. 10. Relationship between field of view and required sampling area

7. Possibilities for Measuring Surface Pressure

Hanson (1969) has studied the question, "If the atmosphere were molecular only, could we measure atmospheric parameters to sufficient accuracy using a radiance inversion technique, given the constraints of remote sensing by earth's satellite solar illumination angle, and photomultiplier noise in the measurement?"

The spin-scan cameras on geostationary satellites ATS-I and ATS-III have some very useful properties. They are really telescopic photometers with a linear output over a wide dynamic range. The photomultiplier detectors have noise proportional to the square root of the signal current. Since the satellite

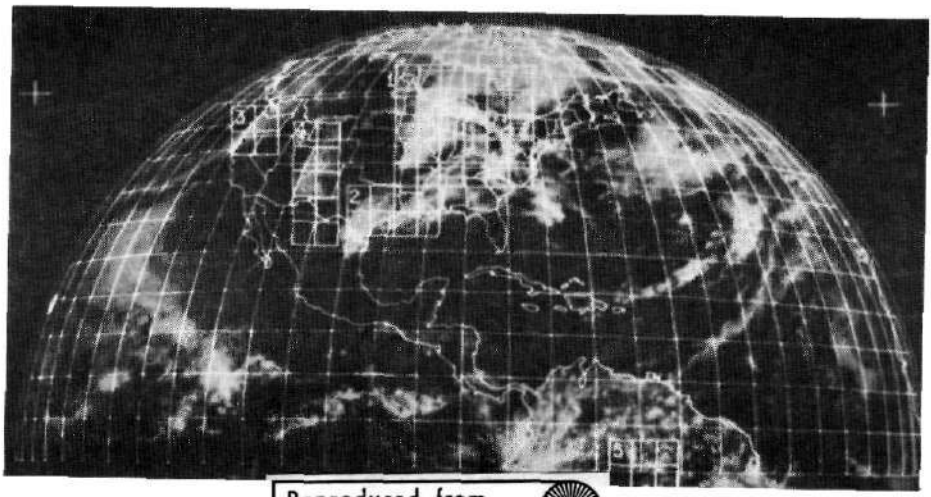

Fig. 11. GARP grids superimposed on typical cloudiness distribution

is fixed relative to the earth, the geometry is much simpler than that associated with low-orbit, fast-moving vehicles, and finally the angle of solar illumination for each point in the field of view undergoes a large, but accurately predictable change during the course of a day. The study considered the application of bi-spectral radiance measurements from a geostationary platform for the measurement of height of the cloud tops and sea-level pressure. The height and mass discriminator used was the Rayleigh scattering of the atmosphere. The study showed that the error in sea-level pressure determination due to photomultiplier noise is minimum at local noon for the point being measured. The error is largest at the subsatellite point and decreases towards the limb. Since the photomultiplier noise is random, one can use multiple samples. Over an area 200 mi × 200 mi, the error in pressure at the subsatellite point would be 1.4 mb and approach a minimum at 0.8 mb near but not at the earth's limb. These results were obtained by using channels at 0.45 μ and 0.55 μ. If the channel separation were increased to 0.36 μ and 1.67 μ, an increase in resolution by a factor of two seems possible.

The study did not consider the effects of particulate in the atmosphere. Polarization measurements could be used to identify these areas. Figure 12 shows the errors in surface pressure. These errors are very large because they apply to a single observation. In practice, a 200 mi × 200 mi square would have 10^4 observations which would reduce the error by a factor of 100.

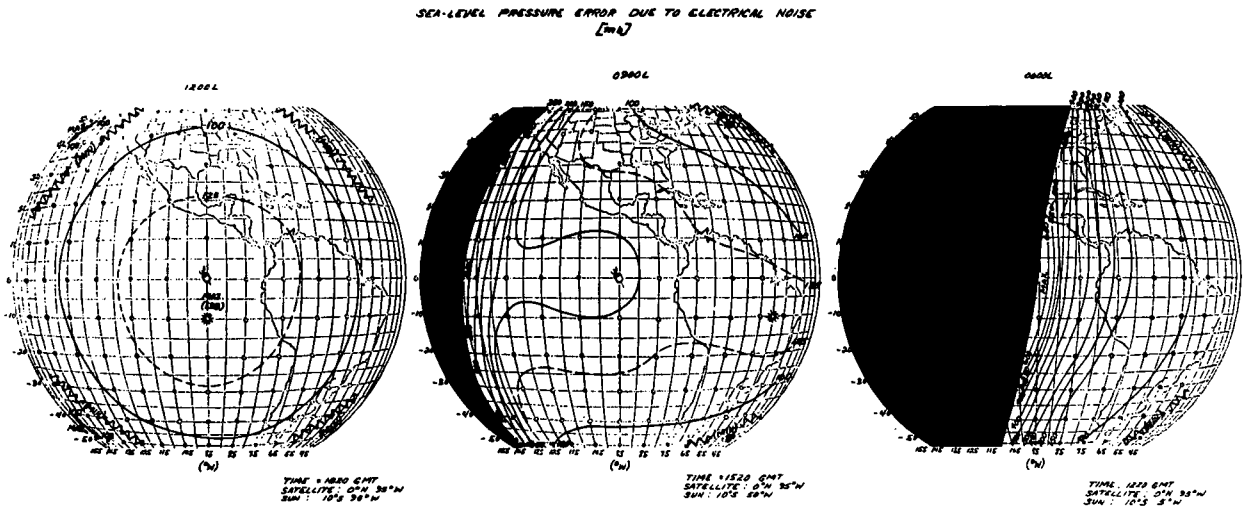

Fig. 12. Surface pressure errors due to spin-scan camera noise

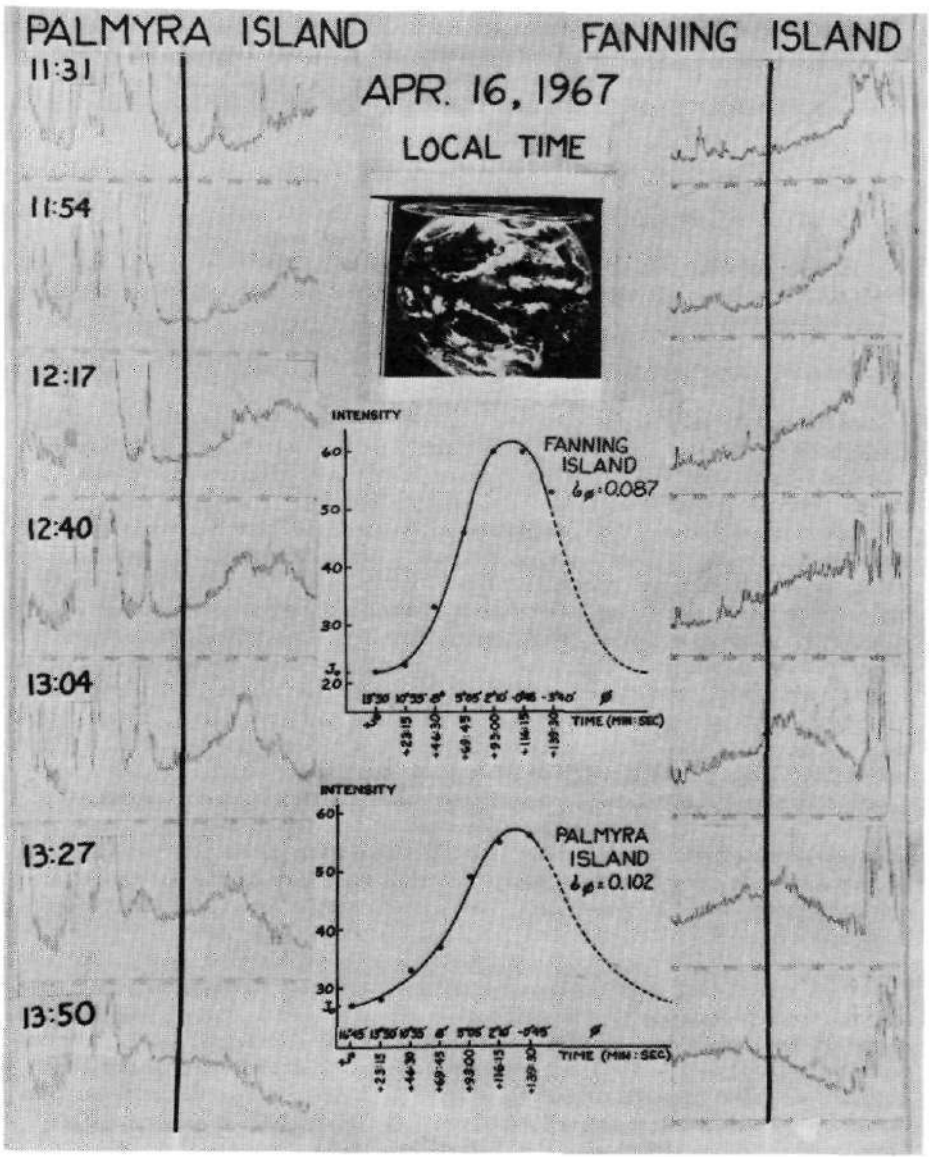

Fig. 13. Surface brightness distribution due to sun glitter

In these tests, the spin-scan camera was operated at nominal gain settings. The gain can be increased by a large factor on command. The cloud images would saturate the photomultiplier but better data at low brightness levels would be available for these pressure studies. Further tests like these are planned.

8. Observations for GARP Sub-programs

In this section, we consider developments not directly a part of the global observing system, but relevant to the observations required for the GARP Tropical sub-programs.

(a) Surface winds over the ocean

In many ATS photos one can see a bright area due to specular reflection of sunlight from the sea surface. This effect is called sun glitter or sun glint. Cox and Munk (1956) have shown that the brightness distribution is related to the statistical distribution of the sea surface slopes. They showed further that the mean-squared slope, a parameter measurable from the sun glitter, is proportional to the surface wind. Levanon (1970) has tested this relationship using the sun glitter measured with the ATS spin-scan camera. He finds that the surface wind speed can be obtained to about one meter per second. If the sun glitter is measured from a near-earth satellite, the sun glitter area will be about 100 miles across. The cross-wind brightness, due to sea slope, is uniformly distributed, but the downwind brightness distribution is skewed due to the unsymmetrical waves. It should be possible to obtain wind direction also from the sun glitter distribution in both directions. In addition, one has global coverage. From geostationary altitude, the sun glitter can be thousands of miles across. It cannot be assumed that the wind field is uniform over this large area. Levanon assumed that the wind in a local area of the open ocean was constant for about a two-hour period. He obtained the slope distributions in one direction only from the change in brightness due to the changing sun angle at the point of observation. Two sample brightness distributions are shown in Fig. 13.

It is known that specularly reflected radiance is polarized and the degree of polarization depends on the angle of incidence, which can be related to the slope of the surface wave facet. The polarization (Hariharan, T. A., private communication) is a sensitive parameter and could be expected to yield better quantitative data on wind direction. One might well obtain the surface wind direction as well as the surface wind speed from sun glitter measurements. This information together with the drift of low level trade cumulus which must be related to the wind in the upper portion of the planetary boundary layer might be used to determine friction parameters in the planetary boundary layer.

(b) Vertical heat-transfer due to convection

In the time lapse movies referred to earlier one can easily see the development of convective clouds which form thunderstorms. These thunderstorms produce an anvil cirrus cloud like the cap of a feather-edged mushroom, as the rising air meets the tropopause or other stable layer. Aircraft measurements have shown these layers to be 1 km to 1.5 km thick. A simple model can be derived where the mass of air rising through the thunderstorm stem can be estimated from the growth of the cirrus cloud shield. Sikdar (1969) has tested and applied this model to large-scale convection and has been able to obtain surprisingly good estimates of convective activity. He has used this technique to measure the heat transport from the lower troposphere to upper troposphere. Large-scale convection in cloud clusters is a key mechanism for weather of the tropics. He was able to show that the release varies with a five-day periodicity. Since the life-time of the convective elements embedded in the cluster is much shorter than this, the large-scale motion of the tropical atmosphere must control the convective heat release. Figure 14 shows the cycle of variation over a thirty-day period for the area from 120° - 180° west in two belts, 0-15° north and 0-15° south latitude. When Sikdar separates this large area into an eastern and western zone, he has a sharper phase filter. Figure 15 shows the five-day periodicity and the phase difference between the eastern and western zones of the northern belt. Yani (1968) has found a similar periodicity in the meridional components of winds in the tropics, particularly in the 200 mb region.

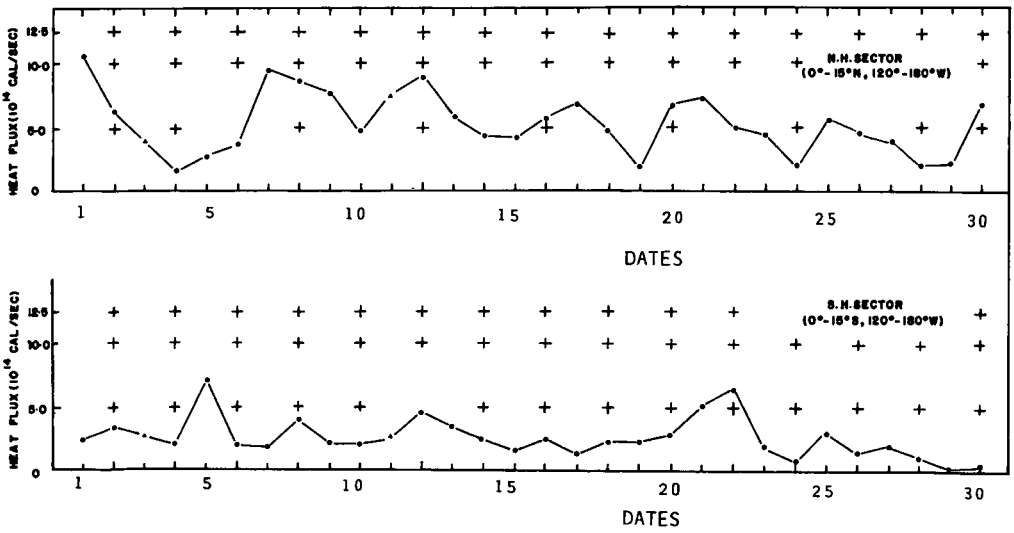

Fig. 14. Cyclic variation of convective heat release in tropical zone

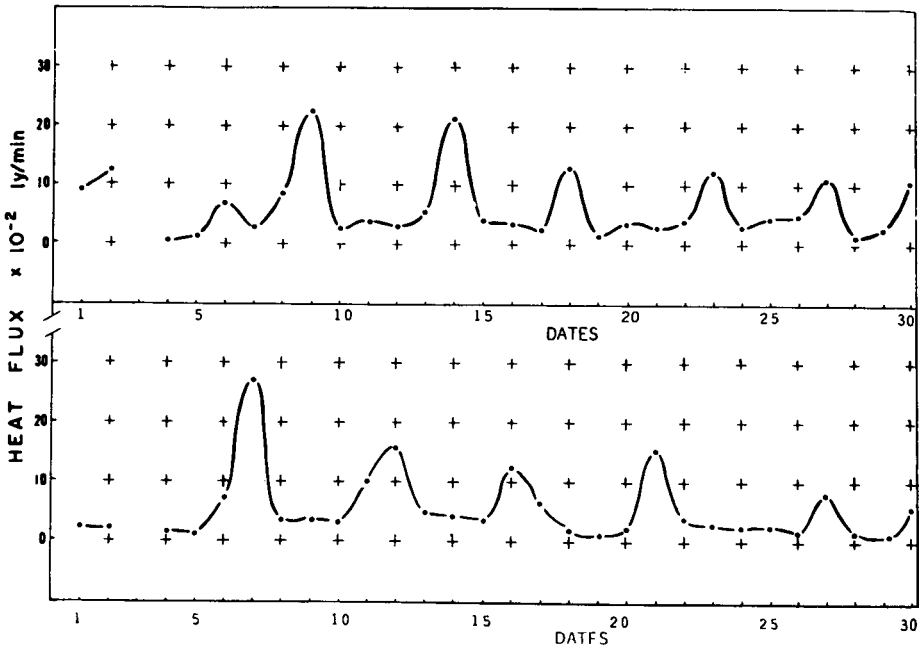

Fig. 15. Same as Fig. 14, except eastern and western half of northern zone

(c) Enhancement of images to reveal cloud cluster structure

The wide dynamic range of the photomultiplier detector on the spin-scan camera cannot be reproduced by ordinary photographic materials. Ordinarily one generates from a voltage (the signal from the camera) the spot brightness (which exposes the film) in a functional form which corrects the gamma of the film and paper used to record the image. It is possible to use an extremely nonlinear amplifier to enhance the dim portions of the picture to bring out thin clouds or to enhance the bright portion of the picture to subdue all but the brightest parts of the image. The three photos of Fig. 16 have, from top to bottom, (a) low brightness enhancement, (b) both low and high brightness enhancement, and (c) high brightness enhancement. Since thick clouds are the brightest ones, and thick clouds indicate strong convective activity, at least in the tropics, we now have a powerful way to study convective activity of cloud clusters. As mentioned earlier, Sikdar has estimated the total mass flow upward in a cloud cluster. If the photo enhancement technique can provide a good estimate of the area of the convective column, one might be able to estimate the average vertical velocities in the convective elements. This possibility is now being studied at the University of Wisconsin.

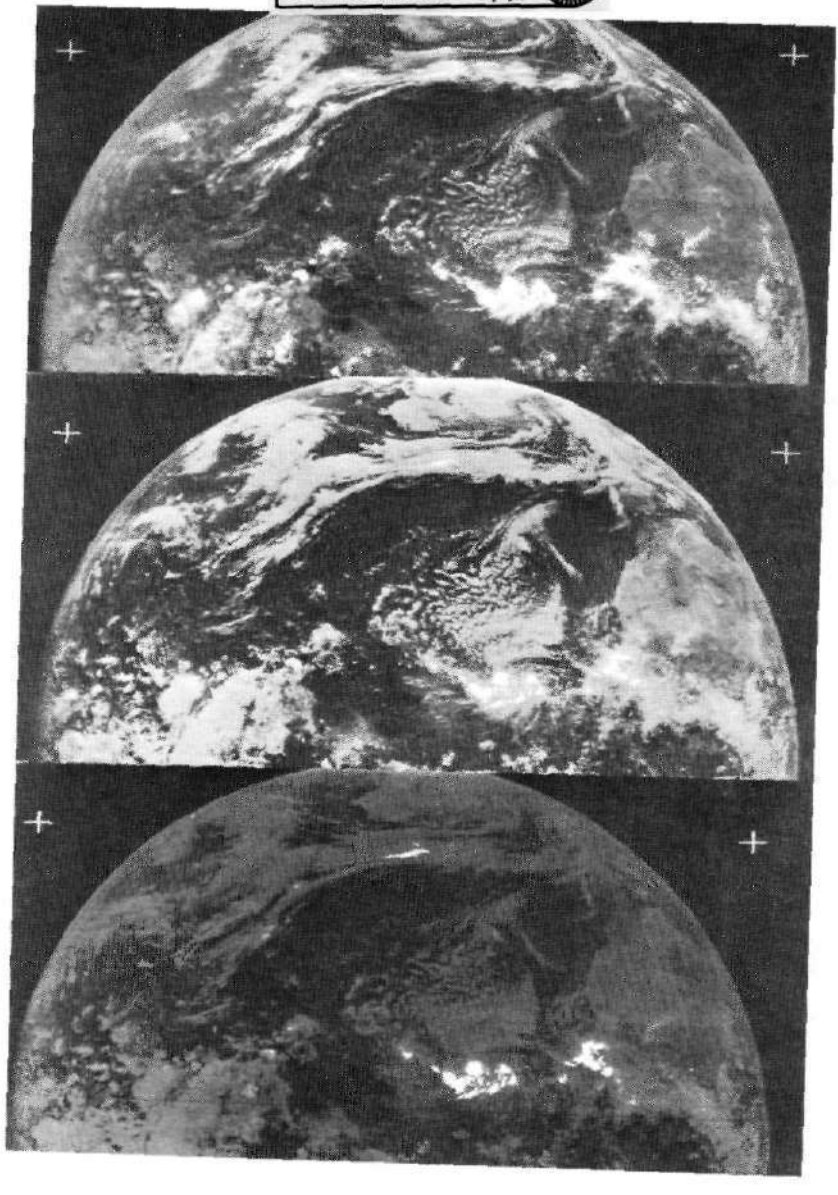

Fig. 16. Cloud cluster convective structure revealed by image enhancement (a), (b), (c).

These are a few of the developments which hold promise for greater utility of both low altitude orbiting satellites and geostationary satellite platforms.

References

COSPAR Working Group VI. 1969. "Systems possibilities for an early GARP Experiment," Report to JOC, GARP Pubn. No. 2, W. M. O., Geneva.

Cox, C. and Munk, W. 1956. "Slopes of the sea surface deduced from photographs of the sun glitter," Univ. of California Press, Berkeley and Los Angeles.

Fujita, T. 1968. "Present status of cloud velocity computations from ATS-I and ATS-III," COSPAR Space Research, No. 9, pp. 557-570.

Global Atmospheric Research Program (GARP). 1967. Report of Study Conf. Stockholm, 28 June to 11 July, W. M. O., Geneva.

Hanson, K. J. 1969. "Applications for bi-spectral radiance measurements from a satellite," Ph. D. thesis, Univ. Wisconsin.

Hasler, A. F. 1970. "A blink technique for quantitative measurements of cloud motions from ATS-I," Weather in motion, V. E. Suomi and K. J. Hanson (Eds.). Univ. Wisconsin Press. (To be published).

Hubert, L. F. and Whitney, L. F. 1970. "Accuracy of wind estimates from geostationary satellites," Presented at the Symposium of Tropical Met., Honolulu (June 1970).

Kuhn, P. M. 1970. "Applications of thermal radiation measurements in atmospheric science," Advances in Geophysics, Vol. 14 (in press) Academic Press, N. Y.

Johnson, M. H. 1968. "A photogrammic technique for finding winds," MS thesis. Dept. Met., Univ. Wisconsin.

Lally, V. 1969. "GHOST—a technical summary," NCAR, Boulder, Colorado.

Levanon, N., Suomi, V. E. and Stremler, F. G. 1970. "Applications of radio Altimetry to balloons," AFCRL Balloon Symposium. (To be published).

Levanon, N. 1970. "Determination of sea surface slopes, distribution and wind velocity using sun glitter from ATS-I," Weather in motion, V. E. Suomi and K. J. Hanson (Eds.), Univ. Wisconsin Press. (To be published.)

Mintz, Y. 1967. "Report of Panel 1" (p. 9), Report of Study Conf. Stockholm. W. M. O. Geneva.

Morel, P. 1966. "Definition scientific du projet de satellite FR-2" (Project EOLE), Centre Nat. de la Recherche Scientifique, Service d'Aeronomic No. 101.

Santa Barbara Research Center. 1968. "Three camera designs for meteorological observations from geostationary orbit," SM 4-68, June 1968. Technical proposal.

Sikdar, D. N. 1969. "Convective heat transport over the tropical mid-Pacific as estimated from ATS," Ph. D. thesis, Univ. Wisconsin.

Smagorinsky, J. 1969. "Problems and promises of deterministic extended-range forecasting," Wexler Memorial Lecture, Bull. Amer. Met. Soc., pp. 286-311.

Suomi, V. E., Krauss, R. and Vonder Haar, T. 1969. "On the possibility of sounding the atmosphere from geostationary altitude," Special Report No. 1, under Contract NAS5-11542 submitted to NASA.

Wark, D. Q. and Fleming, H. E. 1966. "Indirect measurements of atmospheric temperature profiles from satellites," Mon. Wea. Rev., 94, pp. 351-362.

Wark, D. Q. and Hilleary, D. T. 1969. "Atmospheric temperature: successful test of remote probing," Science, 165, pp. 1,256-1,258.

Yani, M. 1968. "Power spectra of large-scale disturbances over the tropical Pacific," J. Met. Soc. Japan, XXXXVI, No. 4, pp. 308-323.

POSSIBILITIES FOR SOUNDING THE ATMOSPHERE FROM A GEOSYNCHRONOUS SPACECRAFT[1]

V. Suomi, T. Vonder Haar, R. Krauss and A. Stamm
The University of Wisconsin
Madison, Wisconsin

Abstract:

This paper demonstrates that vertical temperature sounding of the atmosphere from geostationary altitude is feasible. It treats the meteorological and instrumental options which must be considered to obtain soundings from this great distance with the required accuracy in a reasonable period of time. Measurements from the geosynchronous ATS satellites are used to examine cloud conditions. Observations from experiments on NIMBUS-III are used to specify radiance levels to be measured. For a spin-scan system, like that planned for the SMS, an instantaneous field-of-view of 0.3 mrad - 0.4 mrad (11 km - 14 km) is recommended for the tropospheric sounding channels of 20 cm^{-1} bandwidth near the 15 μm region. Results indicate that it will be possible to sound the atmosphere to the earth's surface through openings in a 95% cloud cover in less than one hour.

1. Introduction

The measurement of infrared radiance from the earth's atmosphere well enough to infer the vertical temperature profile from geostationary attitude is difficult due to the low energy levels encountered. At 35 800 km, random noise from the radiation detector is a large fraction of the signal from the atmosphere. Given a suitable optical system and very sensitive detector, we can overcome this energy deficiency by using multiple sampling in space, time or both. One must not use too long integration times, however, since

[1] Contribution (A. 1. 14) to the Symposium on Remote Sounding of the Atmosphere, XIIIth Meeting of COSPAR, Leningrad, USSR, 20-29 May, 1970.

the parameter of interest, atmospheric temperature, varies with time. One must also insure proper space sampling since temperature varies with space as well. Despite these difficulties, the effort will be well worth the trouble one must take because the atmosphere is a four dimensional system (x, y, z and t) and a continuous view adds the dimension time.

Such nearly continuous views of atmospheric conditions were first returned from experiments on the Applications Technology Satellites (ATS) I and III [1], [2]. These satellites are in equatorial orbits at geostationary altitude. They have carried high-resolution telescopic photometers to measure reflected solar radiance. Many of these measurements, formed line by line into a single frame, give an image of the earth-atmosphere system during a twenty- to thirty-minute period. Successive frames allow the measurement and study of the time variation of atmospheric conditions over a large portion of the earth's surface.

Very recently, spectrometer and interferometer experiments on NIMBUS-III [3,], [4], and NIMBUS-IV have successfully demonstrated the capability to infer atmospheric temperature profiles from radiation measurements. In addition, the operational value of such measurements (from the polar-orbiting NIMBUS) has been shown [5]. It is the purpose of this paper to study the possibility of placing a vertical temperature profile experiment on a geostationary satellite. Our immediate requirement is the ability to infer temperature profiles with an RMS error of less than 1°C.

One way to reduce the error is to restrict the observations to clear areas only. Thus only clear column radiances are used to reconstruct the temperature profile, and errors due to the presence of cloud are removed. The Nimbus III and IV results are very impressive even including cloud in the field-of-fiew, but few would argue that the presence of cloud contributes to higher accuracy.

It is possible to reduce the field-of-view of the instrument in order to see through small openings in the clouds. A smaller field-of-view, however, decreases the signal-to-noise ratio of the measurement and more samples must be taken in order to improve the S/N ratio to acceptable levels. As one reduces the field-of-view, are enough additional samples available to compensate for the poorer signal? A general answer to this question is not possible since the performance parameters of different instruments will yield different answers.

The central question of our study may be stated another way. Each radiance observation will be contaminated by detector noise and may be contaminated by "cloud noise." With a large instantaneous field-of-view (IFOV) it is not possible to separate the detector noise from the cloud noise. With a small IFOV, one can separate the "cloud noise" which is not random from the detector noise that is random. However, one can do this only at the

price of a poorer signal-to-noise ratio. Are there enough additional clear column samples using a small IFOV to improve the S/N ratio to acceptable levels? The answer depends on the performance specifications of the instrument and on the natural occurrence of clouds.

2. Instrumental Options

The instrumental constraints used in this study are based on typical meteorological spacecraft configurations planned for the early 1970's. These include:

a) a spin-scan instrument system (see Fig. 1)

b) sixteen-inch optics

c) spin rate of 100 rpm

d) cooled HgCdTe infrared detectors (near 11 μm for imaging; sounding near 14 μm).

In addition to the high-resolution infrared imaging sensor (IFOV about 0.2 mrad) it is possible that an even higher resolution "visible" radiation sensor will share the same primary optical system with the infrared sounding channels.

Measurements from the NIMBUS experiments have shown that the magnitude of infrared radiance near the 15 μm CO_2 band varies from 50 to 110 erg · cm^{-2} · sec^{-1} · sr^{-1} · cm from band center to edge during clear sky conditions over most of the region viewed from a geostationary satellite. These same experiments obtained measurements with relative accuracies of about 0.25 erg · cm^{-2} · sec^{-1} · sr^{-1} · cm. Vertical temperature profiles with an RMS error of 1°C were obtained from them. We shall use the observed radiance values to test our proposed experiment and adopt the same relative error value as our limit.

Several important instrument options remain. These include (a) IFOV (α) of the sounding channels, (b) spectral location (ν) and width ($\Delta\nu$) of the channels, and (c) scan rate and time required to cover a finite area. Each of these are interrelated, each affects the relative accuracy of a radiance measurement and each of these instrumental options also represents an important decision that will affect meteorological application of the measurements. Combinations of these parameters (as well as the general instrument characteristics mentioned above) were systematically varied in a set of standard instrumental relationships [6]. These include expressions for the power output from the detector, the noise equivalent power (NEP) and noise equivalent radiance (NER). The latter for any individual measure is approximately:

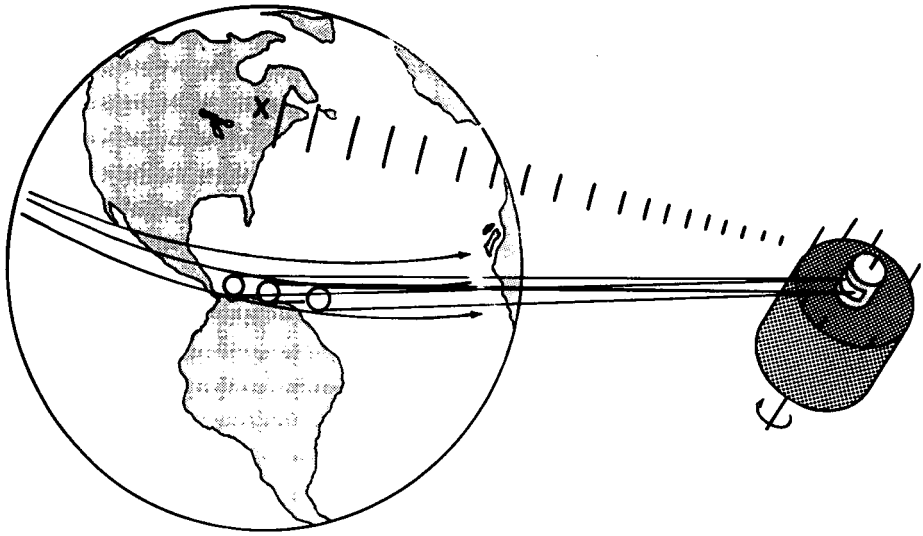

Fig. 1. Schematic depiction of a spin-scan sensor on a geostationary spacecraft.

$$NER \sim 1/\alpha^2 \tag{1}$$

where α is the IFOV. The ground resolution spot size at nadir, D, is directly related to the IFOV, α. Over a finite grid mesh of area A (i.e., 400 km × 400 km as proposed for the Global Atmospheric Research Program) the possible number of discrete measurements, N, varies inversely with D^2. Furthermore, the NER due to random instrument noise for each discrete measurement may be reduced by $1/N^{1/2}$ when a representative radiance value over the grid is desired. Thus:

$$(NER)_A = NER/N^{1/2} \sim 1/N^{1/2}\alpha^2 \sim 1/N^{1/2}D^2 \sim 1/A^{1/2}D \tag{2}$$

Figure 2 illustrates the relationship of the instrumental options for the geostationary sounder considered in this paper. Note that for a radiance error of 0.25 erg · cm^{-2} · sec^{-1} · sr^{-1} · cm the required observable clear area increases rapidly as ground resolution improves. Two additional ordinate scales are provided. One demonstrates the percent observable clear area required in a GARP grid mesh to acquire a sufficiently accurate radiance value with a sensor of given IFOV. It shows that the required accuracy is possible from <u>one scan pass</u> over a region 65% - 85% cloudy if the sensor's ground resolution, D, is 11 km - 14 km. At 100 rpm, one scan pass over a GARP grid near satellite subpoint would take about twenty seconds. For mesoscale

applications over clear regions, the remaining scale shows that the geostationary sounder can acquire an accurate sounding every 150 km if $\alpha = 0.4$ mrad.

It is clear from the above that one observation in each sounding channel cannot be used to infer the temperature profile over the spot size (D = 11 - 14 km) on the earth enclosed in the narrow field-of-view. It may take more than 1,000 discrete observations to improve the signal-to-noise ratio to the level needed to get a meaningful temperature profile determination. This will depend on the specified scan step and sampling frequency. Thus, for the sample instrument described here (with a scan step of 0.2 mrad) the minimum soundable area will be about ninety miles on a side, roughly one-tenth of a GARP grid.

3. Effect of Cloud Distribution

As mentioned earlier, cloud cover interferes with radiometric temperature sounding. To avoid clouds with a given instrument observing over a specified area, we must increase the time required to complete a sounding within our relative accuracy limits. In order to separate cloud fields-of-view from clear observations, a higher resolution (but with a wider bandpass, $\Delta\nu$) infrared imaging channel can be used.

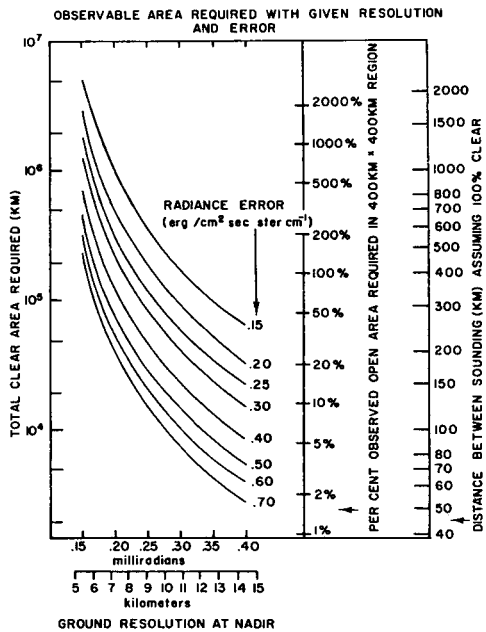

Fig. 2. Nomogram showing interrelation of instrumental options and their influence on meteorological temperature sounding requirements.

Most meteorologically active (baroclinic) regions tend to be quite cloudy. Temperature soundings near these features of the circulation are particularly valuable. In order to test how well one can sample these areas, a special study [7] of cloud distribution was performed. It used data from ATS-I and III, thus simulating the view of the proposed sounder. The spin-scan camera on ATS-I and III has an IFOV of only $\alpha = 0.1$ mrad. Thus it was possible to simulate the cloud statistics of a radiometer having a larger IFOV.

Some of the regions studied (e.g. Fig. 3) were completely cloud-covered. Others (in the intertropical convergence zone, over areas of dense broken cloud cover near extratropical fronts and within active convective cloud regions over South America) can be represented by the traces labeled Case 1, 2 and 3 in Fig. 4. These show the reduction in the total area of clear fields-of-view as a function of sensor ground resolution. The values are normalized to the percent clear area seen by a sensor with ground resolution of 4.6 km. Example 4 in the figure is a rather special case with all clear areas smaller than 7 km. Other, less cloudy, conditions are shown to have less rapid reduction of observable clear area with increasing α or D.

In order to optimize the engineering choices to typical cloud distributions we must specify the scan step size mentioned earlier. Since a high resolution infrared imager is likely to be included along with the sounder, a scan step about 0.2 mrad is probable. We shall use this value and thus a typical frame of the entire earth would require 15 to 20 minutes.

Table 1 shows the time required to obtain a vertical temperature sounding over a GARP grid for various cloud conditions using the above scan step with our sample instrument. Note that while 0.2 mrad stepping was used, the sounding channel had an IFOV of 0.4 mrad. The surface temperature is 300°K; a relative radiance error of 0.25 erg $\cdot$ cm^{-2} $\cdot$ sec^{-1} $\cdot$ sr^{-1} $\cdot$ cm will be obtained over the grid mesh. Note that even in a region of 95% cloud cover an accurate sounding is possible in under one hour.

It is evident from our trade-offs between relative accuracy, field-of-view and area/time that there is an optimum set of parameters for a specific spacecraft and basic instrument. The observing system considered here is similar to the proposed GeoSynchronous Meteorological Satellite (SMS). For such a system we are apparently instrument-noise limited for small IFOV's and cloud-noise limited at larger IFOV's. Figure 5 shows this very well in terms of relative sounding time required over a GARP grid. Each trace refers to a cloud situation shown in Fig. 4. For a given case the valley curves indicate a preferred resolution to minimize the sounding time. This effect is demonstrated by Stamm and Vonder Haar [7] who considered eighteen grids near frontal zones over the U.S. and over convective cloud regions of the Amazon basin (see Fig. 3). Four of these regions are more than 99% cloud-covered and cannot be sounded at $\alpha = 0.3 - 0.4$ in a reasonable time period. Of the remaining fourteen, nine may be sounded with desired accuracy in less than one hour with

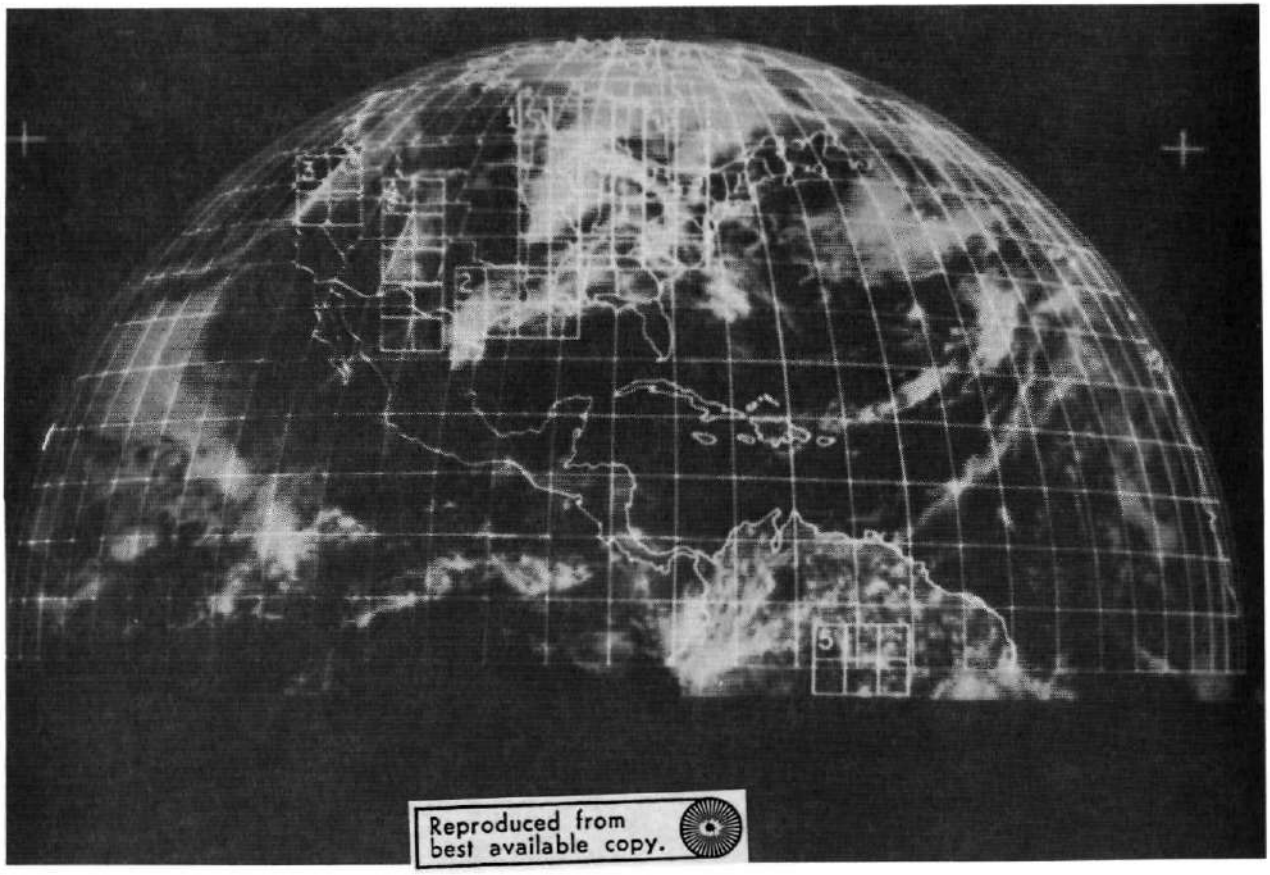

Fig. 3. ATS-III picture of 23 April 1968 (1714Z) noting grid areas used in cloud distribution study [7].

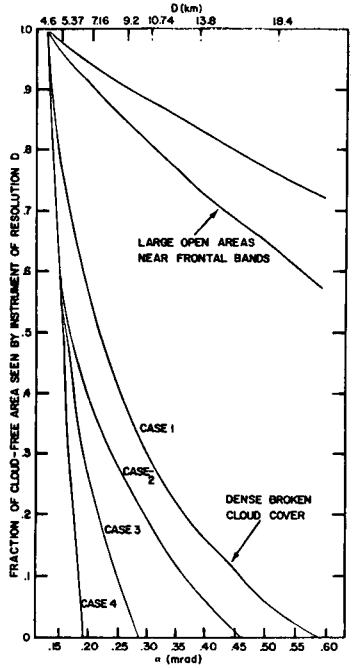

Fig. 4. Fraction of "open" or cloud-free area seen over a GARP-size grid by instrument of angular resolution α (normalized to 100% of 4.6 km ground resolution).

Table 1

Temperature Sounding Time Required for Various Cloud Conditions (A = 160 000 km^2, $(NER)_A = 0.25$ erg · cm^{-2} · sec^{-1} · sr^{-1} · cm, $\alpha = 0.4$ mrad, $\nu = 690$ cm^{-1}, $\Delta\nu = 20$ cm^{-1})

% open area	Number of complete frames	Time for sounding (hr.)
100%	1	0.26
50	1	0.26
10	2	.52
5	3	.79
1	11	2.88

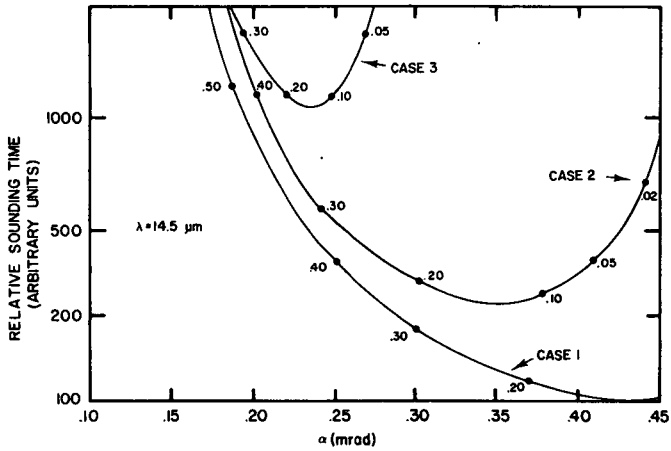

Fig. 5. Relative sounding time required as a function of the rate of change of measured "open" area (Fig. 3) with angular resolution. Values at the dots show fraction of the cloud-free area seen by sensor with specific α.

IFOV of 0.3 mrad - 0.4 mrad and five would require from two hours to six hours. At higher and lower ground resolution the results were less favorable.

In general, the region of α = 0.3 mrad - 0.4 mrad looks best even though we are viewing only 10% - 30% of the cloud-free area which would be viewed by a sensor with smaller α. Since the curves in Fig. 5 have rather flat minima, it may be best to make a final IFOV selection closer to 0.4 mrad to gain signal-to-noise ratio as noted by Eq. (1). This applies especially to the low- and mid-tropospheric channels, those where cloud effects are most severe.

4. Summary

Our studies show that the opportunity for sounding the atmosphere from geosynchronous orbit looks very attractive. These studies have shown that even with typical cloud distribution near meteorologically active regions a sounding is possible over a 400 km × 400 km grid mesh within a reasonable time interval.

A recent paper [8] shows that when soundings from geostationary altitude are added to those obtained from two polar-orbiting satellites, the numerical model's predicted wind error is reduced by 35%. In addition, they demonstrate that a geostationary sounder can serve as a powerful backup to a two-satellite polar-orbiting sounding system. Their results show that a combination of

geostationary satellites and one polar-orbiting satellite give wind values at least as good as two polar-orbiting satellites alone if the data are inserted at intervals of twelve hours. They also find that if the geostationary data is inserted more frequently than every twelve hours there is an improvement over results obtained from polar-orbiting satellites. In view of the fact that the incremental cost of including IR sounders on geostationary satellites is relatively modest and that even in the worst conditions one can obtain soundings every two hours, this feature should be added to the global observing system.

COSPAR Working Group VI Report [9] states that, "If the results of such studies show that IR soundings will be feasible from geostationary satellites, such observations in combination with those obtained from near-polar satellites would form an almost ideal complementary combination." The present study shows that the IR sounding from geostationary altitude is indeed feasible and the observing system simulation study [8] shows these observations to be very valuable.

5. References

1. Suomi, V. and Parent, R., 1968. Bull. Am. Met. Soc., 49, p. 74.

2. Suomi, V. and Vonder Haar, T., 1969. J. Spacecraft and Rockets, 6, p. 342.

3. Wark, D. O. and Hilleary, D. T., 1969. Science, 165, p. 1256.

4. Hanel, R. and Conrath, B., 1969. Science, 165, p. 1260.

5. Smith, W., Woolf, H., and Jacob, M., 1970. Mon. Wea. Rev., 98.

6. Krauss, R., 1970. Special Report under Contract NAS5-11542, SSEC, The University of Wisconsin.

7. Stamm, A. and Vonder Haar, T., 1970. J. Appl. Met., 9.

8. Jastrow, R. and Halem, M., 1970. Bull. Am. Met. Soc., 51.

9. COSPAR Working Group VI Report to JOC, Second Draft (1968).

NOTE: We thank Professor R. Parent for his contributions to this work and acknowledge support of NASA under contract NAS5-11542.

A RADIO ALTIMETER FOR BALLOONS AND SOME METEOROLOGICAL APPLICATIONS

Nadav Levanon and Verner E. Suomi

Abstract:

A newly developed radio altimeter permits geometric altitude measurement of meteorological balloons up to altitudes of 30 km. The one-second averaged random error is smaller than 0.1%. The 0.5 W peak power pulsed radar is simple and light enough to be carried aloft by a regular sounding balloon together with a radiosonde. Flight tests were conducted on standard radiosonde flights and on board GHOST balloons. This paper briefly describes the principle of operation and results of flight tests. It suggests possible applications in the areas of improving atmospheric sounding and new scientific experiments.

1. Introduction

In the paragraphs which follow we describe a relatively simple, lightweight, low-power radio altimeter suitable for use on balloons, kites or other air or space platforms. Depending on the integration time one can achieve very high accuracy. For example, at 30 km one can obtain the altitude to one meter in about one minute. The absolute accuracy of the instrument is not yet known because a suitable calibration technique of comparable accuracy is not readily available.

The description given here is oriented toward the user. It emphasizes applications and results of flight tests. A more technically oriented description will appear elsewhere (Levanon, 1970).

2. Applications

Ever since the beginning of ballooning, most height determinations have been made using a pressure measurement and the hydrostatic equation

$$dP = -\rho g dZ \qquad (1)$$

where P is the atmospheric pressure, ρ is the air density, g is the acceleration due to gravity and Z is the geometric altitude.

If we express the air density in terms of pressure and temperature as is obtained in a typical radiosonde observation, we get the height of the air column in question

$$Z - Z_0 = (\ln P_0 - \ln P)R\bar{T}/Mg \qquad (2)$$

where R is the universal gas constant, $\bar{T}$ is the mean temperature in the column and M is the molecular weight constant. When the observation is over the ocean, $Z_0 = 0$ and P_0 is the sea level pressure. Clearly, if one has independent height information it is possible to extract useful meteorological information from the relationship. Here are a few examples:

(1) A reference pressure for GARP. Any method of atmospheric sounding requires reference pressure. This is usually achieved by measuring the surface pressure. A key requirement of the global system is true global coverage. In areas where no surface pressure observations exist it is possible to use a reference pressure at the altitude of constant level balloons—another component of the proposed global system. While this application of the radio altimeter was the main purpose behind its development, a number of additional experiments are possible.

(2) Direct measurement of the ageostrophic component of the wind. In the free atmosphere, during balanced motion, a constant level balloon should, in the first approximation, fly along a contour line on a constant-pressure surface, or along an isobar on a constant-level surface. That is, the pressure altitude and geometric altitude should remain constant, or change equally. Any departure will be due to cross gradient flow and can yield the ageostrophic component of the wind.

(3) Improved radiosonde. Radiosonde readings at high altitude are relatively inaccurate. The barometer resolution approaches the total pressure, and the temperature sensor is affected by stronger solar radiation. Through the use of the hydrostatic equation, the geometric altitude could replace one of the less accurate parameters.

(4) Fast-falling dropsonde. An obstacle in the development of fast-falling dropsonde is the relatively long time constant of the temperature sensor. Here again it could be replaced by measuring the geometric altitude. Furthermore, if the projected area of the dropsonde is known, and the geometric altitude is measured continuously to yield the velocity, then the air density can be calculated, and a complete sounding is achieved without any additional sensors.

(5) Ranging. The altimeter is actually a ranging device. In normal operation it will measure the arriving time of the surface return. However, there is no reason why it cannot measure the arriving time of an artificial return, created by a transponder. With two such transponders, horizontal position of the balloon could be located, adding wind measurements to its list of applications.

3. The principle of operation

The radio altimeter is a pulsed radar system in which the period of the transmitted pulses is, when locked, a measure of altitude. Prior to locking, this period is varied by a VCO (Voltage Controlled Oscillator). A receiving window exists before each transmitted pulse (Fig. 1). As the pulse period approaches the delay length of the returned pulse, $2h/c$, the receiving window starts sampling a prior pulse reflected by the earth surface.

In cases of scattered reflection, the shape of the returned pulse (Fig. 2), is a convolution integral of the transmitted pulse (Moore, 1957, Edison, 1960). It is an attenuated duplicate of the transmitted pulse in cases of specular reflection (Brown, 1969). It can also be a combination of the two. In both cases, there is a relatively well-defined break point in the returned pulse at the point corresponding to the end of the transmitted pulse. This break point is enhanced and brought to a form in which it can serve as a zero error signal by taking the derivative of the returned pulse. This is done by injecting small perturbations into the transmitted pulse period (Fig. 1). When the period of the transmitted pulses is too large, i. e. the trailing slope of the return is

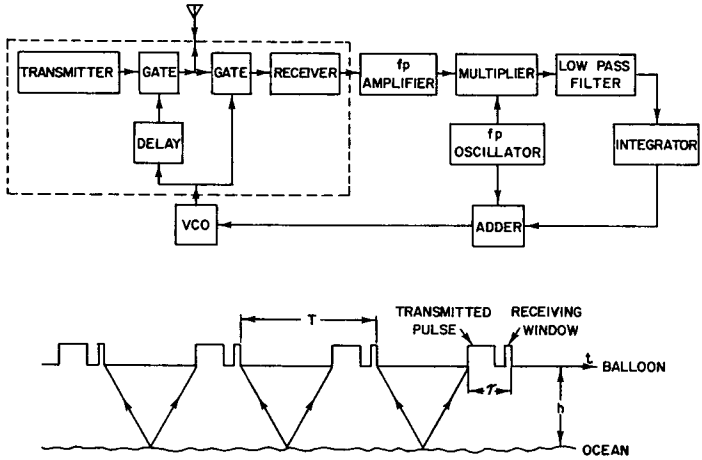

Fig. 1. The altimeter block diagram and principle of operation

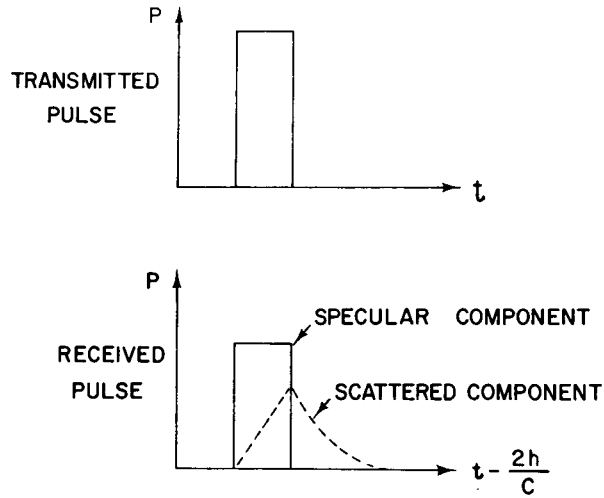

Fig. 2. Simplified representation of transmitted and received pulses

sampled, the receiveived signal at the perturbation frequency fp is out of phase compared to the injected perturbation (Fig. 3). When the period is too short, i.e. the leading slope is sampled, the injected and detected perturbation signals are in phase. These injected and detected perturbation signals are fed to a multiplier to yield the derivative of the returned pulse, which is also the error signal of the loop. A filter and an integrator are following which smooth this error signal and lock the VCO to that period which corresponds to the peak of the return pulse. Such a system is known in control theory as "single parameter sinusoidal perturbation adaptive system" (McGrath, 1961; Eveleigh, 1967).

In practice, the transmitter, receiver, gates and delay blocks of Fig. 1 are all combined in a single superregenerative stage (Hall, 1950). This is a highly oscillatory radio frequency circuit which, when allowed to oscillate, shows a receiving sensitivity at the beginning of the oscillations growth. Those oscillations, upon reaching saturation, become the transmitted pulse.

When the rest of the system is analyzed, it shows a resemblance to the well-studied phase-locked loop (Viterbi, 1966; Gardner, 1966). The system optimization is therefore based on data available for that loop. The main parameter of such a loop is its bandwidth which is approximately the inverse of its built-in averaging period. To reduce the effects of fluctuations in the returned pulses and of added noise, the lowest possible bandwidth is preferred. The lower theoretical limit on this bandwidth is determined by the rate of altitude changes which the altimeter has to follow. A practical limit is added by

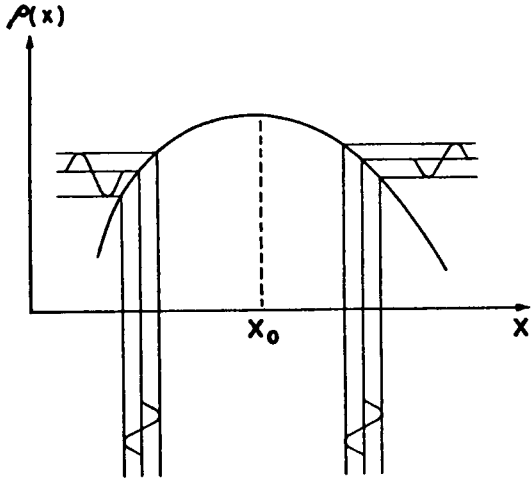

Fig. 3. The effect of sinusoidal parameter perturbations upon a single dimensional even-function curve.

the finite search and lock-in time, requested in case of loss of locking. For ascending radiosonde, 1 Hz bandwidth was found to be practical. This implies that the built-in averaging period of the altimeter is approximately one second. With the lowest pulse repetition rate being 3×10^4 pps, it further implies that at least 3×10^4 returns are averaged for each reading. This number can be increased by adding external averaging.

4. Range, ambiguity and data output

Return shape considerations and the fixed delay between the receiving window and the transmitted pulse impose a lower limit on the altitude, which is about 1 km. The upper limit is influenced by many parameters; the dominants among them are power, antenna gain, and the terrain. The upper limit for the unit outlined in Table 1, when flown over water, is about 35 km. The pulse delays corresponding to these two limits are 6.7μs and 243μs, respectively. However, this does not imply that the pulse period has to vary over such a wide range. As can be seen in Fig. 4, there is no reason why the altimeter cannot transmit a second pulse (or more) before the previous one is received. We shall call this subharmonic operation. This mode of operation can happen by itself at any altitude above twice the minimum altitude of operation. This immediately indicates that the minimum range of altitude required to get full

Table 1

Altimeter Parameters

Altitude Range	1 km to 35 km
Frequency	403 MHz or 1680 MHz
Peak RF Power	0.5 W
Average RF Power	25 mW
Pulse Width	0.5 μs
Pulse Repetition Rate	3×10^4 to 10^5 pps
Perturbation Frequency	200 Hz
Antenna	2 or 4 element Yagi
Antenna Gain (over dipole)	3.2 or 7.7 dB
Polarization	Linear
Total Power Consumption	1 W
Input Voltages	$\pm$ 13 V ($\pm$ 10%)
Electronics Temperature Range	-55°C to +55°C
Weight (approximately)	1 lb.

coverage is equal to the minimum altitude. If the minimum altitude of operation is 2000 m, then the range of the altimeter should be from 2000 m to 4000 m. Above 4000 m the altimeter will switch to a subharmonic mode. From Fig. 5 it is clear that the first ambiguity problem starts at 6000 m which is 3×2000 m, or, 2×3000 m, and the altimeter can lock on both. The pattern of switching modes as the balloon ascends, in the case of no loss of locking except at the end of range, is marked in Fig. 5. However, this pattern is not guaranteed since loss of locking might occur. In any case, the ambiguity is equal to at least the lowest altitude (in our example 2000 m), and it can be resolved by pressure reading or by the history of the ascent.

Subharmonic operation is recommended even if the range of operation is limited, as in the case of the superpressure balloons. In this case, however, it is possible to assure that only one mode will cover this limited range. Operation in a subharmonic mode means more pulses per unit time, therefore, more transmitted power and better signal-to-noise ratio.

The best means of extracting the altitude data is counting the pulse repetition rate. The exact relation between the geometric altitude h, and the pulse repetition rate f, is given by

$$h = (n/f - \tau)c/2 \tag{3}$$

where c is the velocity of light, n the subharmonic mode number, and τ the built-in delay between the receiving window and the end of the transmitted pulse. The only man-made parameter in (3) is τ, which can be measured and

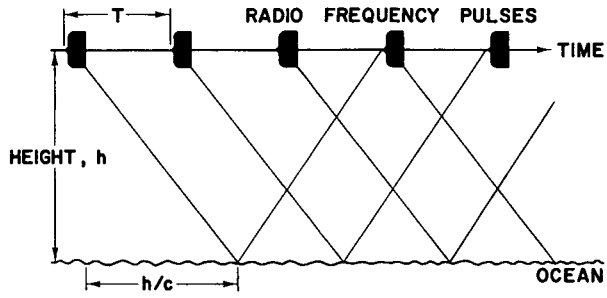

Fig. 4. Sub-harmonic operation

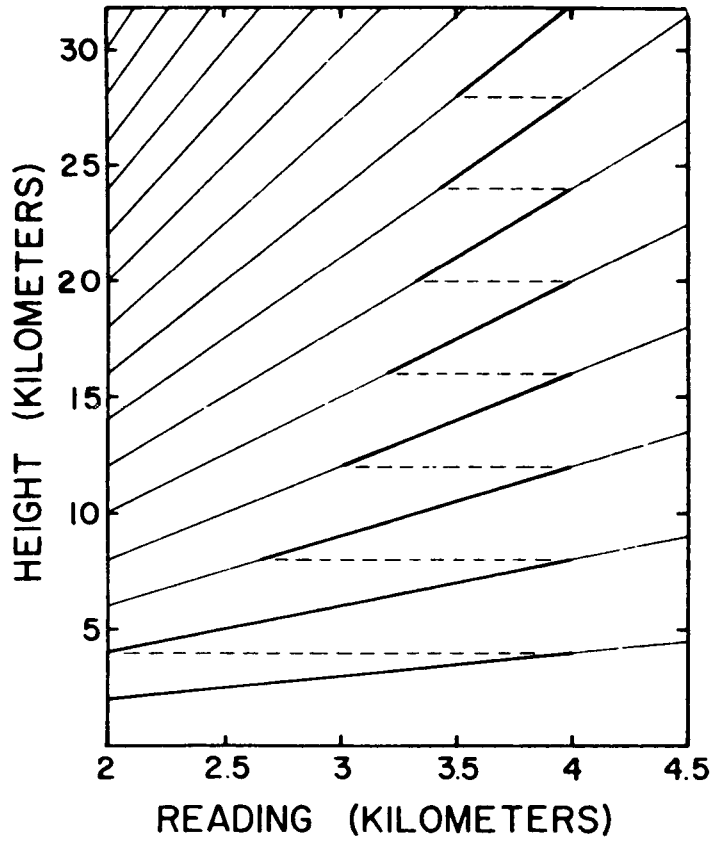

Fig. 5. Ambiguity pattern

controlled to within several orders of magnitude better than the altimeter-specified accuracy.

In short-range balloon flights, such as radiosonde flights, remote counting of the repetition rate is relatively easy, since the ground station is within receiving range from the altimeter radar pulses. The block diagram of such a ground station is shown in Fig. 6. The receiver detects the radar pulses themselves, and feeds them through a band-pass filter whose width should include the entire possible range of the pulse repetition rate. Despite this high bandwidth, the actual information bandwidth is less than 1 Hz, since this was the bandwidth of the altimeter loop itself. A phase-lock stage is therefore used in the ground station to achieve the lower bandwidth. It should be pointed out that in order to achieve locking, the phase-lock loop bandwidth has to be at least fp, which is the perturbation frequency.

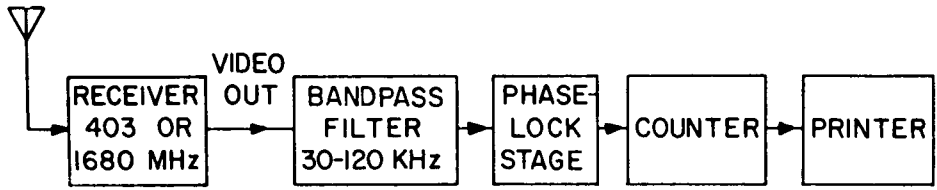

Fig. 6. Block diagram of the ground station

What has been described above is a scheme of telemetering a 1 Hz bandwidth of information, on a channel 10^5 times wider. This inefficient scheme was justified since the telemetry channel was already there in the form of the radar pulses themselves. In longer balloon flights, such as GHOST flights, the bandwidth reduction has to be done on board the balloon payload itself, before transmission. To prevent any degradation in data accuracy, the data should be kept in frequency form, and the reduction should be done by mixing and dividing. The altitude data for further manipulation in the frequency domain is branched off the altimeter loop (Fig. 1) after the VCO.

A third form of data, an analog one, is available if the data is branched off the altimeter loop after the integrator. The data here is in the form of voltage, which is the preferred input of many telemetry channels. However, a man-made link, the voltage-to-frequency curve of the VCO, is now introduced in the data chain, and some degradation in accuracy should be expected.

5. Circuitry and flight tests.

The altimeter circuitry is in continuous change, following progress in the project, and progress in the development of electronics devices. The super-

regenerative stage used in the described flight tests utilized a nuvistor triode at the 403 MHz meteorological band. Laboratory tests of solid state super-regenerative stages at both 403 MHz and 1680 MHz have already been made, and those units will be tested in balloon flights in the near future. The rest of the circuitry is all solid state, mainly in the form of Integrated Circuits. The narrow-band amplifier is an operational amplifier with a twin T network in the feedback loop. The multiplier is a Field Effect Transistor (FET) chopper. The integrator and oscillator utilize operational amplifiers. The filter is a passive lag-lead network. The VCO is an astable multivibrator in which the charging resistors are returned to a variable input. The VCO is followed by a pulse shaper which includes a monostable stage and an amplifier. In addition, there is a bias control stage, whose purpose is to maintain a proper super-regeneration action, and it is doing so by sensing the width of the transmitted pulse. Several types of antennas were used in the flight tests. They included slotted dipoles, dipoles, rhombics and two- or four-element Yagies. The Yagies were found to be the most suited for this application.

As of 1 December 1969, a total of nine flight tests were conducted: four on board aircrafts, three on board regular radiosonde balloons, and two on board GHOST balloons. The purpose of the aircraft flights was to test the principle of operation with a prototype model, to test units prior to shipment to the GHOST flight experimenters, and to gather information on the shape of the return pulse.

The balloon flights were more realistic tests for the altimeter. The first among them was a failure as far as altitude readings were concerned. However, it brought a wealth of information with regard to ground reception, problems resulting from the pendulum motion of the payload of ascending balloons (MacCready, 1965), and the electronics behavior under true environmental conditions. The second and third radiosonde flights were very successful and will be described in more detail. They were launched near Sturgeon Bay, Wisconsin, on 14 and 15 March 1969. In the 14 March flight, the altimeter utilized a two-element Yagi antenna. The electronics and the antenna are shown in Fig. 7. The electronics weigh 130 g, and the antenna 40 g. A radiosonde battery was used to supply the anode voltage and filament voltage for the tube. Two 12V water-activated batteries supplied the power for the rest of the circuitry. The altimeter pulse repetition rate was modulated on the radiosonde 1680 MHz signal, without disturbing normal radiosonde operation. This scheme was preferred on receiving the altimeter pulses directly on 403 MHz, since, for the 1680 MHz band a higher gain dish antenna was available at the ground station. A second reason for a better reception of the radiosonde signal was the fact that the radiosonde antenna was pointing sideways toward the ground station, while the altimeter antenna was pointing downward.

The altimeter and the radiosonde were carried aloft by a standard 1200 g neophrene balloon. The payload was tied at the bottom of a 100 m string to minimize the pendulum motion. After the balloon broke, the payload landed at

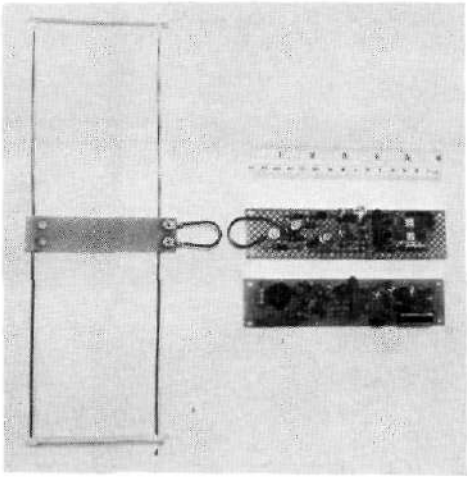

Fig. 7. The radio altimeter layout

Norwalk, Michigan, and was returned by the finder. This implies that most of the flight, and certainly all of the ascent, took place over Lake Michigan.

Height readings started seven minutes after launch, as the balloon crossed the minimum operational altitude of the altimeter, which was 1.8 km. From then on the height was recorded continuously for the next fifty-seven minutes, when the balloon reached an altitude of 16 km. In the next ten minutes the altitude readings became intermittent. Yet, good data were still available up to an altitude of 18.5 km where the signal-to-noise ratio decreased to the point that no locking could be achieved. The altimeter data were recorded by counting the pulses over a period of one second, and printing the result. This was repeated every two seconds during the entire flight.

In Fig. 8 several height measurements of the altimeter in intervals of about five minutes, during the ascent, are compared to heights calculated from the temperature and pressure data received from the radiosonde. These calculations utilized the hydrostatic equation with steps equal to five contacts on the radiosonde baroswitch. Calibration of the baroswitch was performed two weeks before the flight.

Height readings were received also on the descent, starting at an altitude of 14.2 km and continuing down to 2.2 km, although the readings were intermittent during portions of the descent. Some of these readings are compared to the radiosonde data in Fig. 9.

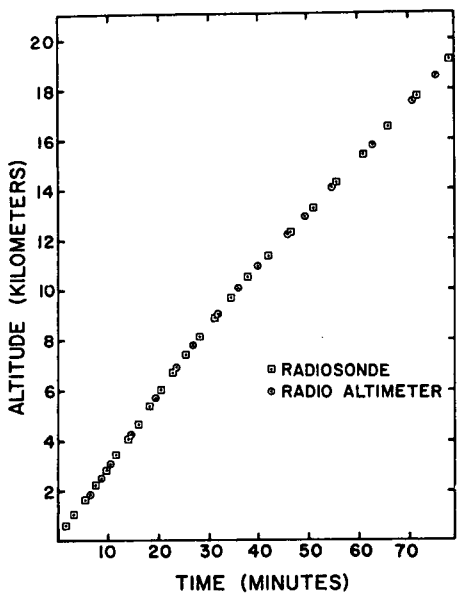

Fig. 8. Altimeter height readings, compared to radiosonde height calculations, during the ascent of 14 March 1969, Sturgeon Bay, Wisconsin.

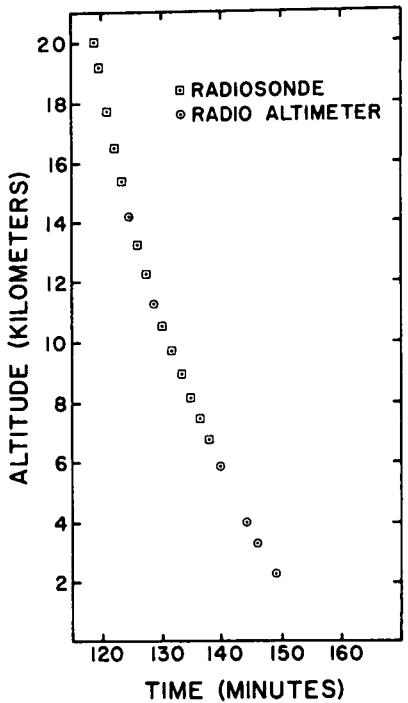

Fig. 9. Altimeter height readings, compared to radiosonde height calculations, during the descent of 14 March 1969, Sturgeon Bay, Wisconsin.

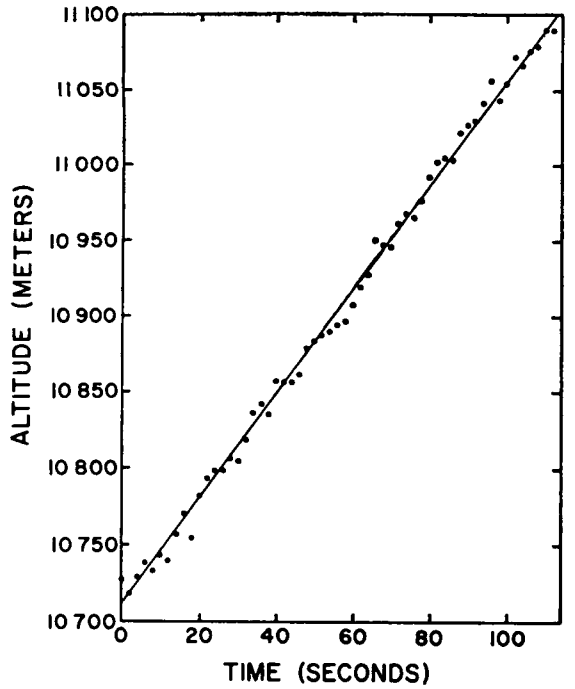

Fig. 10. Sample of the radio altimeter height readings over a two-minute period during the ascent of 14 March 1969, Sturgeon Bay, Wisconsin.

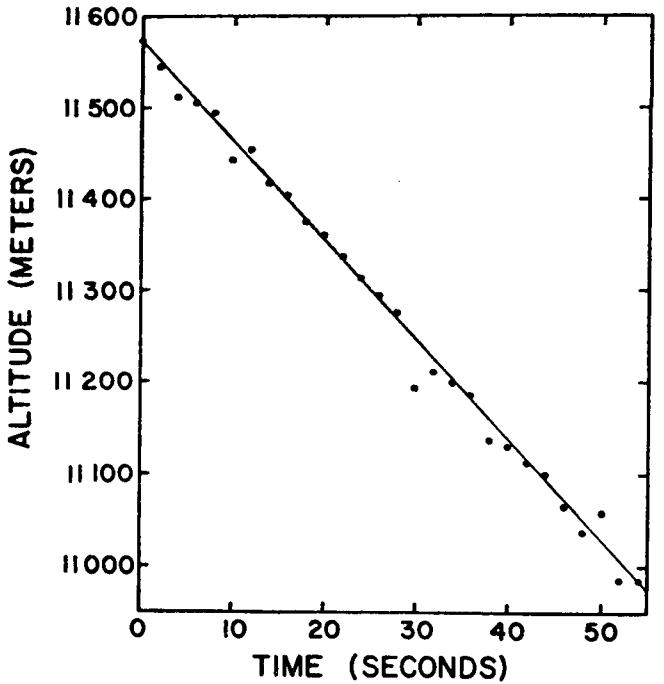

Fig. 11. Sample of the radio altimeter height readings over one-minute period during the descent of 14 March 1969, Sturgeon Bay, Wisconsin.

Altogether, more than 2500 meaningful height measurements were recorded during the flight. It is impossible to present all the data in this report. We chose the 200 mb level, which happens to be the midrange of this flight, and presented the readings received from the altimeter over a period of two minutes during the ascent (Fig. 10) and one minute during the descent (Fig. 11). From Fig. 10 we note that the 1 s rms value of the random error, at an altitude of nearly 10 km, is smaller than 7 m. This is an error of 0.07%.

What is called error here is actually the sum of the true error due to noise, plus existing erratic balloon motions, plus the effect of the pendulum motion of the payload, plus end type error caused by the fact that the counting period does not include full number of perturbation periods.

The major difference in the 15 March test was the use of a rhombic antenna. This flight terminated near Williamsburg, Michigan, implying that nearly two-thirds of the flight took place over the lake. The rhombic antenna was much bulkier than the Yagi, and matching it to the altimeter indoors was more complicated. As a result, it was not matched properly, and its higher gain was more or less compensated by this mismatching. The highest altitude recorded by the altimeter was 16.8 km. In Fig. 12 we present the readings received from this flight during a period of about one minute near the 200 mb level. Contrary to the previous flight, the altimeter did not function at all during the descent. A possible explanation to this could be that the rhombic antenna became tangled during the descent.

The two GHOST flights were launched from Christchurch, New Zealand on 16 September 1969 and 3 October 1969. The main modification in the circuitry was the addition of an interfacing circuitry, in order to reduce the high pulse repetition rate to the slow Morse type code of the GHOST system (Lally, 1969). The end result of the data reduction was a one-to-one relation between the altitude, h, and the period, T, of ten consecutive transmissions of the Morse letter L. The ground station operator can tolerate a variation in the period, T, from 10 s to 40 s. It was hence designed that this range of T will correspond to the altitude range of approximately $\pm$ 1 km around the 200 mb altitude, when the altimeter operates in the third subharmonic mode, and around the 100 mb altitude, when the altimeter operates at the fourth subharmonic mode. Assuming the resolution of the period measurement was 0.1 s, then the corresponding altitude resolutions were 10 m at 12 km (200 mb), and 14 m at 16 km (100 mb).

The first GHOST balloon was launched to a floating altitude of 15800 m (100 mb). The electronics payload included the regular GHOST package, an additional solar-cells panel to supply power for the altimeter, and the altimeter itself. The ground station was able to trace the altimeter for several days, and locking was observed. However, radio interference from the GHOST transmitter prevented proper operation of the interfacing circuitry, and the data were uninterpretable. This problem was corrected toward the second launch.

The second GHOST balloon was launched to a floating altitude of 12200 m (200 mb). The GHOST package and the altimeter were carried aloft by an experimental Cannibal-loon (Lally, 1969). The geometric altitude of the balloon during the first day is shown in Fig. 13. During the first three hours, a check on the geometric altitude was provided by a ground radar. This check becomes less accurate with time since the horizontal drift of the balloon forces the radar to operate at longer range and decreasing elevation, where errors in alignment become significant. The 65 m to 110 m difference between the altimeter data and the ground radar data encouraged the New Zealand Weather Service to check the alignment of the ground radar system. Preliminary analysis indicated errors between 0.1 and 0.2 degrees. These errors could account for the difference. Returning to the altimeter data, they show a rise of about 100 m during the first two hours after reaching floating altitude. This corresponds exactly to the theoretical rise expected from the Cannibal-loon, as it released its excess gas. From then on, and for the next five hours, a remarkably smooth altitude trace was observed. Data transmission ended as the sun angle dropped below 20 degrees, reducing the power available from the solar cells below the opera-

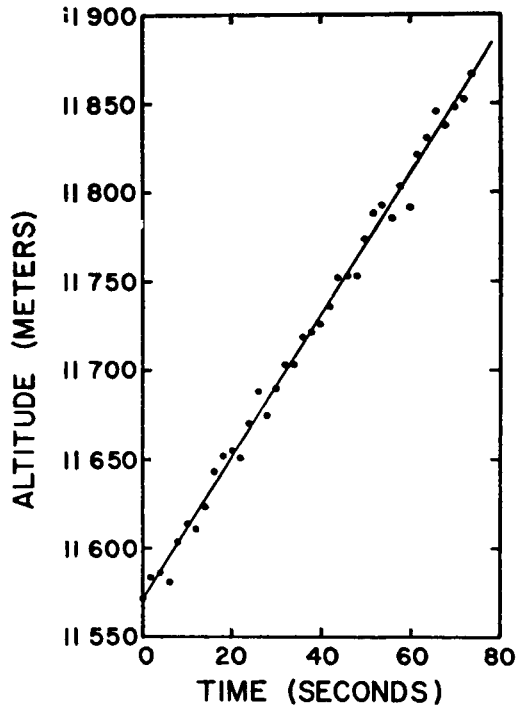

Fig. 12. Sample of the radio altimeter height readings over about one-minute period during the ascent of 15 March 1969, Sturgeon Bay, Wisconsin.

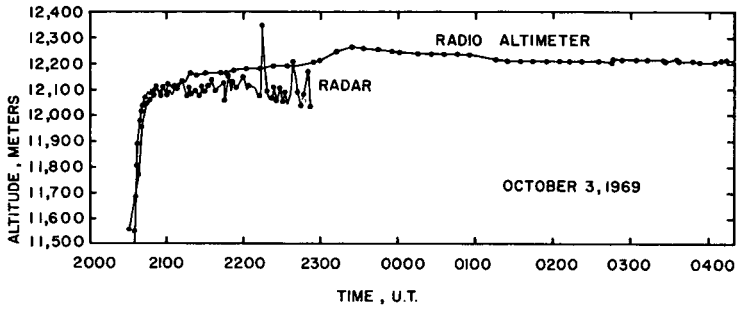

Fig. 13. Altimeter height readings, compared to ground radar readings, during GHOST balloon flight of 3 October 1969, Christchurch, New Zealand.

tional level. Unfortunately, the balloon was nowhere in the skies the next morning. Apparently a major defect caused it to come down during the first night.

6. Summary

In this paper we have presented a new meteorological tool which measures the geometric altitude of balloons. Flight tests conducted by us at Wisconsin and by the NCAR team in New Zealand indicate that this is a working tool. We have outlined several applications, one which initiated the development of the altimeter, and some which evolved during the development. We believe that more applications will be unfolded in the future.

Acknowledgments

This research has been sponsored by the Laboratory for Atmospheric and Biological Sciences, Goddard Space Flight Center, NASA, under Contract NAS5-11542. The authors wish to thank Charles E. Blair for constructing the various models, and for his many suggestions concerning circuit design. Thanks are also due to James A. Maynard for performing the flight tests in Wisconsin, and to Vincent E. Lally and the NCAR GHOST project team for performing the flight tests in New Zealand.

References

Brown, W. E. Jr., 1969. "Radar studies of the earth." Proc. IRE, 57, 612-620.

Edison, A. R., Moore, R. K., and Warner, B. D., 1960. "Radar terrain return measured at near-vertical incidence." IRE Trans. Antennas and Propagation, AP-8, 246-254.

Eveleigh, V. W., 1967. Adaptive Control and Optimization Techniques. New York, McGraw-Hill, 197-222.

Gardner, F. M., 1966. Phaselock Techniques. New York, Wiley, 179 pp.

Hall, G. O., 1948. "Superregenerative receivers." In Microwave Receivers, Van Voorhis, S. N., Ed., New York, McGraw-Hill, 545-578.

Lally, V. E., and Lichfield, E. W., 1969. "Summary of status and plans for the GHOST balloon project." Bull. Amer. Meteor. Soc., 50, 867-874.

Levanon, N., 1970. "Balloon-borne radio altimeter." IEEE Trans. Geoscience Electronics, GE-8 (to be published January 1970).

MacCready, P. B. Jr., 1965. "Comparison of some balloon techniques." J. Appl. Meteor., 4, 504-508.

McGrath, R. J., and Rideout, V. C., 1961. "A simulator study of a two-parameter adaptive system." IRE Trans. Automatic Control, AC-6, 35-42.

Moore, R. K., and Williams, C. S. Jr., 1957. "Radar terrain return at near-vertical incidence." Proc. IRE, 45, 228-238.

Viterbi, A. J., 1966. Principles of Coherent Communication. New York, McGraw-Hill, 3-120.

2

ACCURATE PULSE-RADAR ALTIMETER FOR METEOROLOGICAL BALLOONS

Nadav Levanon
Ferrel Stremler

Abstract:

A simple, light-weight pulse-radar altimeter package has been designed and tested to accurately measure altitudes of meteorological balloons. This altimeter uses a superregenerative RF stage which is controlled by an adaptive feedback system. Altitudes to 20 km have been measured accurately over Lake Michigan using a peak power of one watt.

There is a growing need for an accurate radio altimeter which is simple and light enough to be carried aloft by standard sounding balloons. Some basic ideas for implementing such an altimeter are discussed briefly in this letter.

The altimeter described here makes use of a superregenerative stage serving as both the transmitter and the receiver. This stage is part of a feedback system such that the period between transmitted pulses is a measure of the altitude. The relatively slow rate of change of altitude permits the averaging of many successive returns with a corresponding improvement in the signal-to-noise ratio.

The superregenerative stage when gated on by the quench pulse produces an RF pulse whose envelope area depends on the RF input signal present when the leading edge of the quench pulse is applied. This operation is centered on the growth of oscillations in a highly oscillatory circuit. This action continues until the trailing edge of the quench pulse stops the oscillations and is described in more detail in the literature.[1] The superregenerative circuit

---

[1] Hall, G. O., "Superregenerative receivers." In Microwave Receivers, M. I. T. Rad. Lab. Ser. New York: McGraw-Hill, 1950, ch. 20.

has the advantages that 1) a high receiver gain can be achieved using a single stage, and 2) a single stage can double as transmitter and receiver. It is for both reasons that the superregenerative circuit was chosen for the balloon altimeter package.

The principles of operation of the feedback-controlled superregenerative stage can be described best by referring to Fig. 1. When the period of the quench pulses is equal to the delay of the return pulse, the superregenerative stage detects its own pulses. As the period (or repetition rate) of the quench pulses is varied, the output of the superregenerative detector reaches a maximum near the repetition rate f_q as given by

$$f_q = \frac{c}{2h}$$

where h is the altitude and c is the velocity of light. Varying the repetition rate about this value is equivalent to scanning the pulse for its time of arrival. The remainder of the feedback loop is designed to adjust the repetition rate to the peak of the returned pulse. Before discussing the feedback, however, we shall look at the returned pulse characteristics.

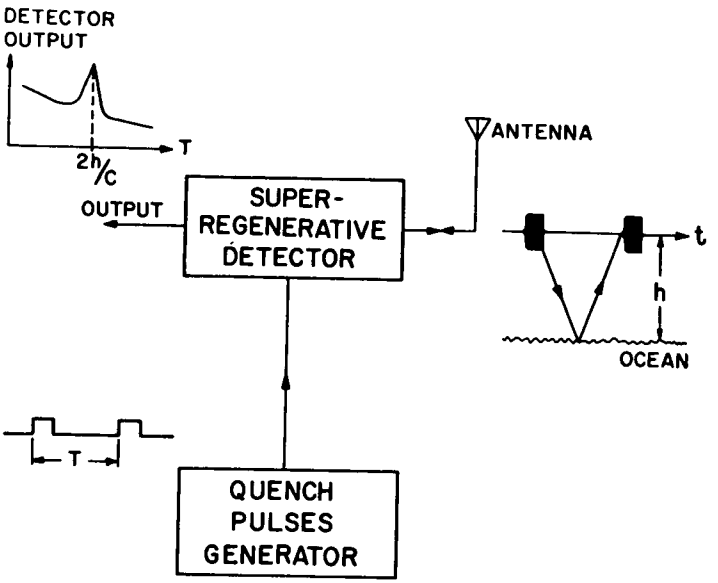

Fig. 1. The output of the superregenerative detector peaks when the quench pulse period equals the delay of the return.

The expected returns at near-vertical incidence are largely due to area scatter[2] and the terrain serves as an imperfect integrator on the pulse envelope.[3] Thus returns from the vertical (i.e., minimum path length) are, on the average, reinforced by returns arriving from small angular displacements from the vertical. The net effect is that if the illuminated area is limited by the pulse length rather than by the antenna beamwidth, the peak or maximum of the returned pulse envelope occurs at the end of the transmitted pulse shape (delayed by the round trip to the altimeter subpoint). Such a condition guarantees that the fixed additional delay between the beginning of the superregenerative quench pulse and the peak of the return is exactly the length of the quench pulse. This can be controlled accurately in the design of the altimeter.

The principle of the feedback system is to always maintain the condition that the leading edge of the quench pulse occurs at the peak of the returned pulse. To detect the error, a small sinusoidal perturbation is introduced in the estimate of the pulse delay, which is the pulse repetition rate. The net overall effect of the perturbation is to take the derivative of the averaged returned pulse envelope. Thus a null condition, corresponding to the peak of the returned pulse, results. This can be used as an error signal in a feedback loop to drive the repetition rate to the correct value. Measuring the arrival time of the peak of the returned pulse is in contrast to conventional pulse-radar altimeters which use the leading edge of the returned pulse for an indication of height.

A block diagram of the pulse-radar altimeter system is shown in Fig. 2. The voltage-controlled oscillator (VCO) determines the repetition rate of the quench pulses. This rate is linearly related to the voltage at the output of the integrator and is sinusoidally perturbed at a preset rate f_pHz. The dependence of the output of the superregenerative detector with quench frequency serves to frequency demodulate the perturbation signal. If the quench frequency is too high, the demodulated perturbation signal (at the frequency f_p) is out of phase compared to the modulating signal. On the other hand, if the quench frequency is too low, the detected signal is in phase, and when it is at the correct frequency (or rate) only higher harmonics of f_p are present.

A synchronous detector is then used to compare the phase of the demodulated perturbation signal with the injected perturbation signal to yield both the magnitude and sign of the error signal. The integrator smooths this voltage and locks the VCO to that frequency which gives the peak output of the

---

[2]Edison, A. R., Moore, R. K., and Warner, B. D., "Radar terrain return measured at near-vertical incidence." IRE Trans. Antennas and Propagation, vol. AP-8, pp. 246-254, May, 1960.

[3]Moore, R. K., and Williams, C. S., Jr., "Radar terrain return at near-vertical incidence," Proc. IRE, vol. 45, pp. 228-238, February 1957.

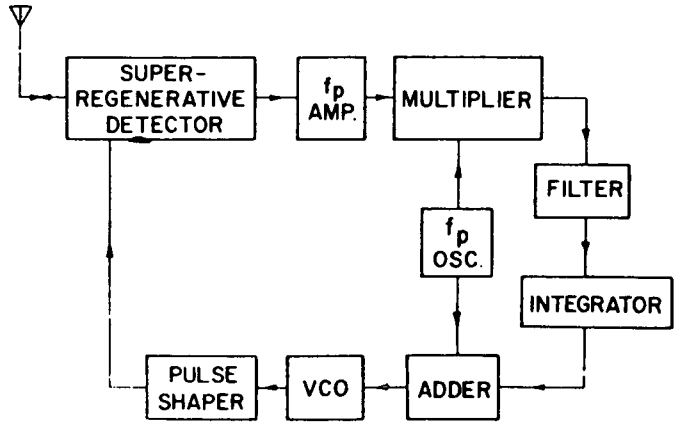

Fig. 2. Block diagram of the radio altimeter

superregenerative stage. The optimization of this feedback loop was based on data available for the optimization of phase-locked loops which are very similar.

Two prototypes of the altimeter described have been constructed and flown in two balloon fights over Lake Michigan.[4] Both versions made accurate measurements of balloon altitude from 2 km up to 20 km using a peak power of one watt. Antenna gain was 3.2 dB over that of a dipole and the wavelength used was 70 cm. The RF pulse width (not including the rise time) was 0.5 μs.

The integration time used in the altimeter was one second. The pulse repetition rate varied between 5×10^4 to 10^5 pps, which implies that at least 5×10^4 pulses were averaged for each reading. Data was made available at the ground station every two seconds by counting the repetition rate of the arriving pulses over a period of one second. At an altitude of 10 km, the rms random error in the altitude measurements was less than 0.07 percent. The range ambiguity of the readings was equal to at least 2 km and was easily resolved by the pressure and temperature data or the history of the flight. These flight tests have demonstrated the capability of the design described here. Further work in this area is continuing.

---

[4]Levanon, N., Balloon-Borne Radio Altimeter, Ph.D. dissertation, University of Wisconsin, Madison, Wis., April 1969.

IMAGE CORRELATOR FOR CLOUD DISPLACEMENT MEASUREMENT

J. G. Miller

INTRODUCTION

When ATS pictures within a series are compared, changes in the position of clouds that move with the wind can be detected. The following problems must be solved before accurate wind velocity can be determined from these displacements:

1. Navigation and Distortion Correction. Where analog means are used to measure displacement, the measurements must be with respect to a land mark. But if the time between pictures is large, the change in location of the subsatellite point causes changes in the relative position of the landmarks. Also the method used to reproduce the pictures causes distortions.

2. Location of the Cloud. The location of a cloud is the location of its mass center. However clouds change shape, even appear and disappear quite rapidly. Therefore, the displacement of a cloud should be measured between pictures with short time differentials to have the best chance of correctly following a cloud and finding its mass center.

3. Accurate Measurement. The displacement of clouds on the picture is so small that accurate measurement is difficult even with considerable enlargement. However, displacement is proportional to time between pictures, so accuracy is greatly improved with long time between pictures.

Thus there is a conflict between the need for a long time between pictures for more accurate measurement and reduction of those distortions that are of a random nature, and the need for a short time between pictures for reduction of navigation and those distortions that tend to accumulate, as well as for location of the mass center of the cloud.

The SSEC image correlator can find the displacements between mass centers so accurately that the use of short intervals between pictures is practical. A means to correct for distortion is inherent in the system.

DISCUSSION

Method of Operation

The method of operation of the image correlation has been documented in [1]. Briefly, a beam of light is passed through the two transparencies of the clouds that are to be aligned, i. e., correlated. The average value of the resulting light intensity is determined by a photo-multiplier. When one transparency is vibrated, an oscillation in light intensity occurs. The light oscillation is either in-phase or out-of-phase with the mechanical vibration, depending on the direction that the transparencies must be moved to correlate the images. The image correlator uses the phase of the oscillation in light intensity as a signal to a motor which moves the transparencies to their correlated position.

Reference [1] describes the very simple electronic and mechanical system that was used to prove the concept to be workable. Appendix A presents the electronics presently being used.

Description of Mechanism

Negatives from the SSEC precision display, approximately 6. 6 inch diameter earth, are held by vacuum along their edges to open center frames that can be vibrated and translated. When thus held, there is approximately 0. 025 inch clearance between the negatives. The upper negative, usually earlier time, is oscillated in the east-west direction and translated in the north-south direction. The lower negative, usually later time, is oscillated in the north-south direction and translated in the east-west direction.

A slightly convergent light beam is passed through the two negatives and focused with a 14" F. F. L. projection lens on a screen with a manificant of 5. 75. The projection lens can be moved parallel to the negatives so that any part of the image can be placed at the center of the screen.

The center of the screen was cut out and an adjustable aperture and photo detector inserted. The signal from the photo detector operates the automatic control system which aligns the images with very high precision. The correlator is operated sequentially, first oscillating and translating in one direction and a few seconds later in the other. The cycle is repeated several times to allow the correlator to find the best fit.

Coordinate Systems

Two coordinate systems are required to record the motion of the two independent mechanical systems. The coordinates which describe the position of

the moving lens are called the XY system. The coordinates which measure the distance that one picture is moved with respect to the other are called the ΔX, ΔY system.

The origin of the XY system is established near the subsatellite point. The approximate location of a cloud or land mass can be found from the X and Y distance that the lens must be moved till its image appears on the aperture at the center of the screen. A small error in the original setting of the origin of the XY system has negligible effect on accuracy of wind determination.

The ΔX, ΔY coordinate system is set to zero when landmarks are aligned. This origin should be established at the landmark closest to the cloud field being studied. A significant ΔX and ΔY will usually be measured at more distant landmarks. The sources of these apparent motions of landmarks are identified in the Error Analysis Section, and a means to correct them is presented in Appendix B.

Conversion of Distance to Correlation ΔX and ΔY to Displacement of a Cloud

The mechanical constraint of the ΔX, ΔY system is that ΔY measures displacement of the upper frame, usually the earlier negative, and ΔX measures displacement of the lower frame, usually the later negative. Figure 1 illustrates the change in position of a cloud as measured by this system.

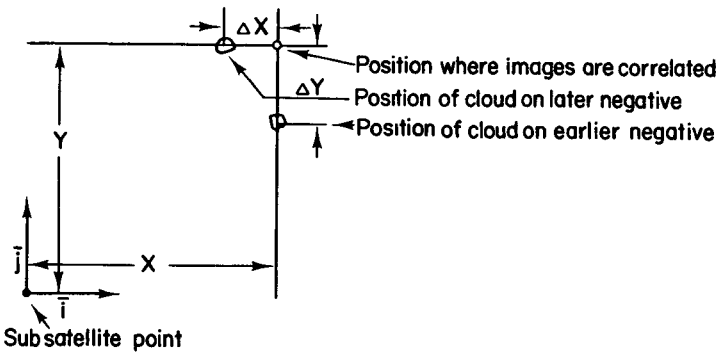

Fig. 1

It can be seen in Fig. 1 that the position of the cloud in earlier negatives is $X\vec{i}$, $(Y - \Delta Y)\vec{j}$, and in the latter negative it is $(X - \Delta X)\vec{i}$, $Y\vec{j}$. The displacement of this cloud is $-\Delta X\vec{i}$, $+ \Delta Y\vec{j}$.

Error Analysis

An error in X and Y, the position coordinate system, will not greatly change the displacement on the earth's surface that is calculated for a given ΔX and ΔY, unless the cloud appears close to the edge of the negative. However, the displacement of a cloud on the earth is very sensitive to the accuracy with which ΔX and ΔY are measured.

The measured ΔX and ΔY are subject to at least three types of errors in the aligned position. The first type is related to the accuracy with which the image correlator can line up the two objects and determine how far the negatives were moved to achieve this alignment. A second type consists of misalignments caused by rotation of the negative, and change in relative position of landmarks due to change in subpoint. The third type of misalignments is caused by errors in processing satellite data into pictures.

The first type of error, ability to correlate, has been shown by a repeatability test to be small if high quality negatives and proper cloud choices are used.

The second type of misalignment can be measured and therefore corrected. Appendix B describes these measurements and corrections.

Errors of the third type have not been investigated thoroughly, but the author believes they can be made very small or possibly measured and corrected. Because of the continuous variations in tape speed that occur during recording and playback, the light intensity sensed by the camera may be displaced as much as 0.0005 inch along the scan line when the negative is produced. This is a small random error which is probably not important. However, the position on the negative at which the scan line starts can be a major source of error. Figure 2 is a 3× enlargement of corresponding "line start" for two pictures that were used during image correlator testing. It can be seen that for the 12:59 picture the displacement of each "line start" was small and usually random. However, on the 12:33 picture, several errors in line start occur that are comparatively large. The largest could result in a ΔX which corresponds to a 40-mph. wind, but even the small errors that can be seen on both line starts will produce significant apparent winds.

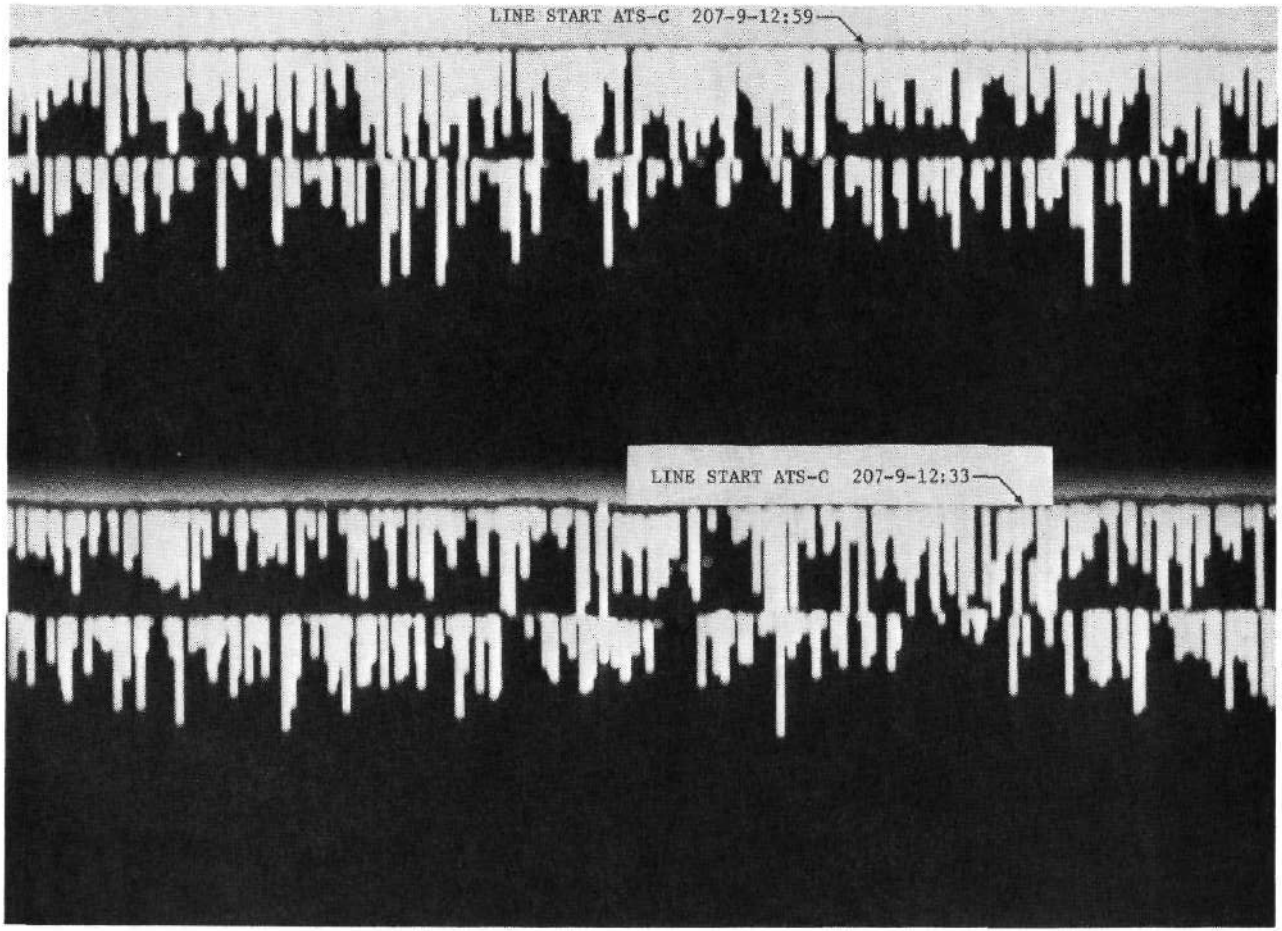
LINE START ATS-C 207-9-12:59
LINE START ATS-C 207-9-12:33

Repeatability Test

Test Description and Data

The images were aligned by the operator and the micrometers which read ΔX and ΔY were set to zero. The image correlator was operated and the micrometers read when correlation was indicated. The test was repeated four more times but with the X and Y displaced a few thousandths of an inch in the four possible combinations of direction as initial conditions. Selected data from these tests are presented in Table 1.

Conclusion from Repeatability Test

1) When the cloud was of similar shape and density on both pictures, either large, small, or textured, the system was able to repeat the correlated position within $\pm$ 0.0005 inch. The measurement was repeatable as long as the shape of the cloud and the change in density between cloud and background were similar on both negatives, even though some clouds were thin and others dense.

2) Clouds which had major differences in shape or density between negatives did not produce an error signal or else there was no position where the error signal became zero. In a case where a cloud appeared on a single line on one negative but was spread over several scan lines on the other, several distinct correlation positions perpendicular to the scan lines could be found.

The test was repeated using the operator's judgement of when clouds were aligned. The difference in position the operator judged to be alignment on repetitive runs was approximately ten times that determined by the correlator.

REFERENCES

Maciejewski, Martin: "Measurements of Cloud Velocity by Correlation of ATS Photorecording Images," Master's thesis, Electrical Engineering, 1969.

Table 1

Selected Run from Repeatability Test

Cloud	Correlation Number 1: Initial correlation—Zero set at operator estimate of correlation ΔX	1 ΔY	2: Displaced + X − Y ΔX	2 ΔY	3: Displaced + X + Y ΔX	3 ΔY	4: Displaced −X − Y ΔX	4 ΔY	5: Displaced −X + Y ΔX	5 ΔY	Maximum Difference Between Correlation Positions ΔX	ΔY
Small Cloud Good Contrast Both pictures	−. 003 3/4	+. 003 1/4	−. 004	+. 003 1/4	−. 003	+. 003 1/4	−. 003	+. 003	−. 004	+. 003 1/4	. 000 3/4	. 000
Medium cloud Good contrast Both pictures	+. 006 3/4	−. 002	+. 007	−. 001 3/4	+. 006 1/2	−. 002	+. 007	−. 002	+. 007	−. 001 3/4	. 000 1/2	. 000 1/4
Medium cloud Poor contrast but similar Both pictures	−. 010	−. 005	−. 011	−. 006	−. 009	−. 005 1/2	−. 008 1/2	−. 005	−. 009 1/2	−. 004 3/4	. 002 1/2	. 001 1/4
Medium cloud Good contrast on one, Poor on other*	−. 001	+. 001	−. 001	+. 001	−. 001	+. 001	−. 001	+. 001	−. 001	+. 001	0	0*
Medium cloud Good on one, poor on other	will not correlate											
Long cloud poorly defined	−0. 000 1/2	−. 003 1/2	+. 001	−. 008 1/2	−. 003	−. 004	−. 007	−. 009 1/2	−. 009 1/2	+. 001	. 008	. 010 1/2

*In this case the poor-contrast cloud seemed to fit inside the high-contrast one.

APPENDIX A

Description of Electronic System

Figure A-2 is a schematic of the electronic system. The axes are operated sequentially for approximately three seconds. The motors step slowly when the integration is partially charged and rapidly when saturated. This results in a system which is insensitive to noise but positions very accurately.

The general schematic is presented in Figure A-1.

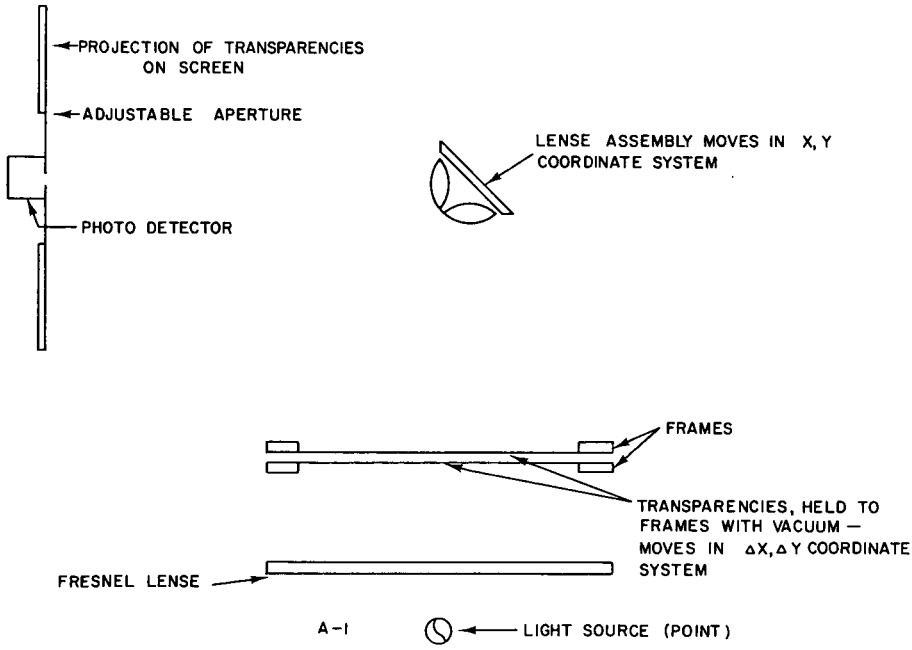

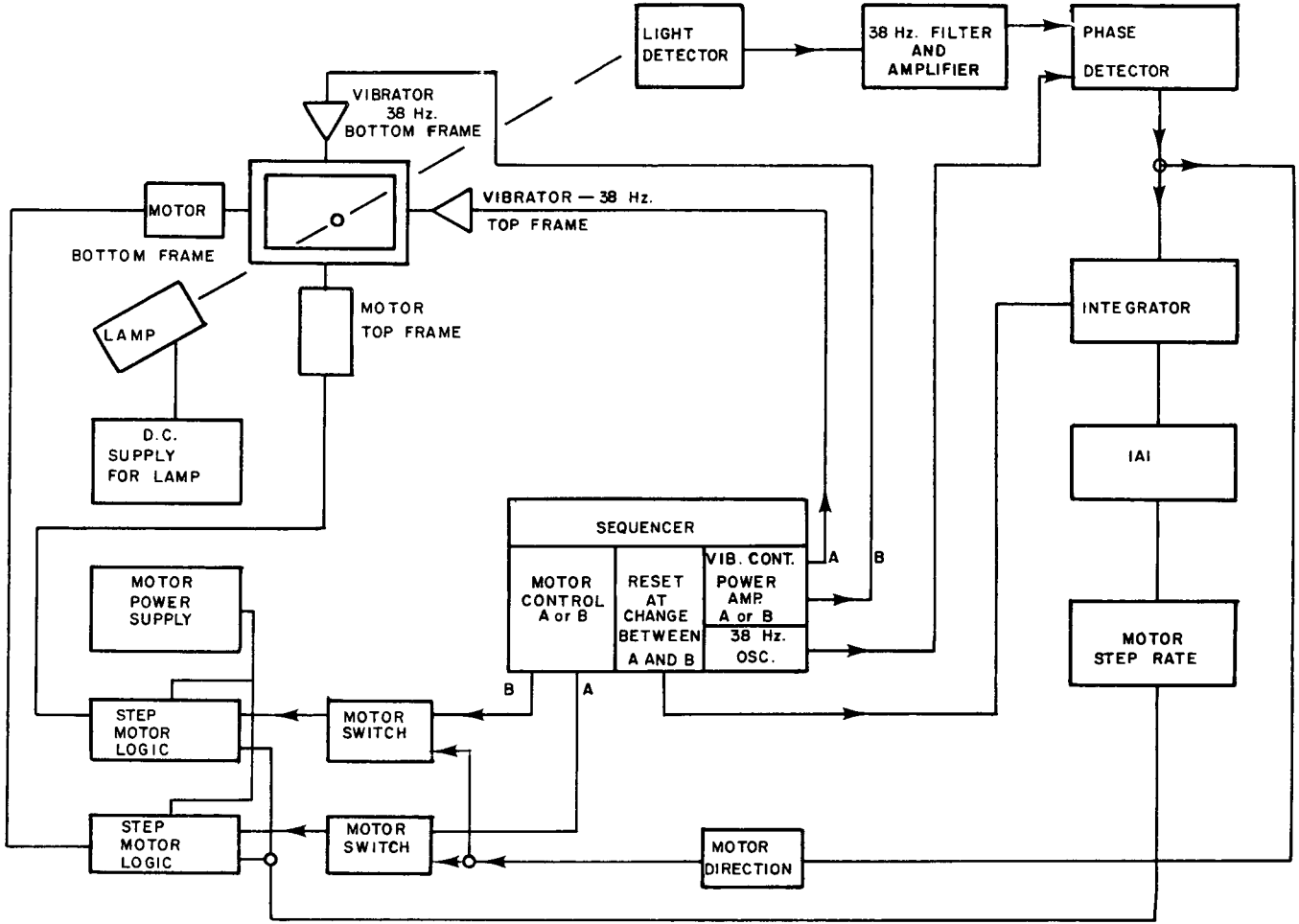

A—2 ELECTRICAL SCHEMATIC

APPENDIX B

Misalignment Correction

A primary landmark, one near the area that is to be studied, is aligned and this position is defined to be $\Delta X = \Delta Y =$ zero. The ΔX and ΔY that will be measured when another landmark is aligned will not be zero because: (1) the negatives may have been rotated when they were installed; (2) the negatives may have changed their shape since they were exposed; and (3) the relative position of landmarks may have changed because of a change in the subpoint.

A linear correction to these misalignments can be made from the ΔX and ΔY that are measured at the secondary landmarks. Figure B-7 illustrates how this misalignment appears when the primary landmark is aligned and the secondary landmark must be moved at a distance ΔX_1 and ΔY_1 before it is aligned. Figure B-2 illustrates the way in which the measured displacement of the secondary landmark was resolved to separate the rotation and distortion components.

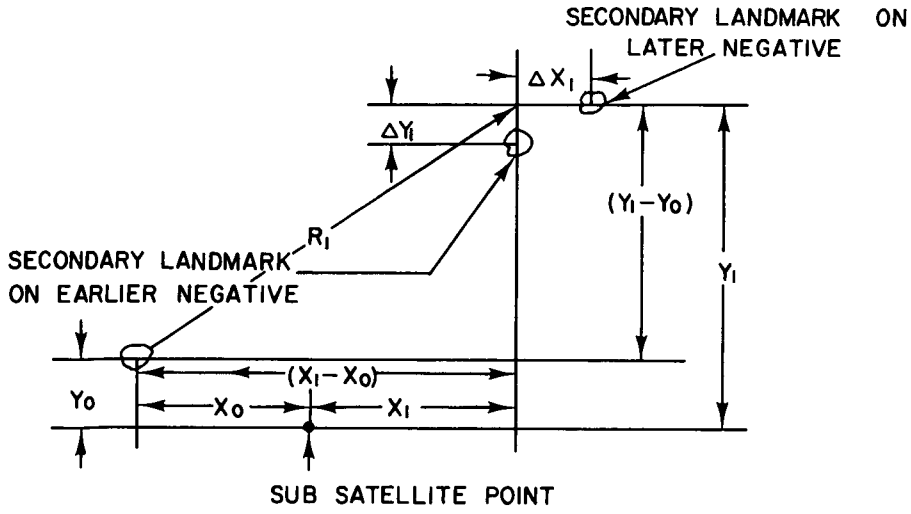

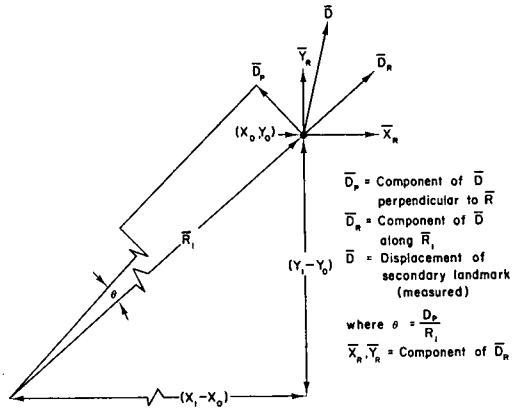

Fig. B-2

A correction based on this measurement can be made as follows.

Rotation Correction. For a cloud located at X_nY_n

$$C_P = \theta((X_1-X_n)^2 + (Y_1-Y_n)^2)^{1/2} = \theta\, Rn$$

The correction C_P is perpendicular to the vector between the primary landmark and the cloud. It can be resolved into its X and Y components C_{PX} and C_{PY} with their origin at X_nY_n.

Distortion Correction for cloud located at X_nY_n.

$$C_{RX} = \frac{X_1 - X_n}{X_1 - X_0} XR$$

$$C_{RY} = \frac{Y_1 - Y_n}{Y_1 - Y_0} YR$$

The corrected displacement of the cloud at X_nY_n is:

$$\Delta X_n \text{ (corrected)} = X_n \text{ (measured)} - (C_{PX} + C_{RX})$$

$$\Delta Y_n \text{ (corrected)} = Y_n \text{ (measured)} - (C_{PX} + C_{RX})$$

If other secondary landmarks are aligned, other correction factors probably will be indicated because the distortion is not linear. Higher order corrections can be calculated.

Vorticity and Divergence Computations from Cloud Displacements

By T. H. Vonder Haar and Eric Smith

Introduction

The selective measurement of cloud displacements can be used to infer winds remotely from a satellite. A sufficient set of these winds will describe the vertical variation of quasi-horizontal atmospheric circulation. Many research and operation applications further describe the flow by means of horizontal velocity divergence and the vertical component of relative vorticity (spin). In fact, one technique for initializing (pre-processing) wind and temperature data for input to numerical models requires vorticity as a prime input (to a form of the "balance equation").

Conventionally, in a cartesian coordinate system, the vorticity, ζ, and divergence, DIV_2V, are derived from (2) and (1) by use of measured values of $\vec{u}$, the eastward, and $\vec{v}$, the northward components of the wind $\vec{V}$.

$$(1) \qquad \zeta = \frac{dv}{dx} - \frac{du}{dy} \qquad \text{[positive = counterclockwise]}$$

$$(2) \qquad DIV_2V = \frac{du}{dx} + \frac{dv}{dy} \qquad \text{[negative = convergence].}$$

Alternatively, both parameters may be computed from simultaneous analyses of wind measurements in terms of streamlines (lines describing the wind direction in an Eulerian reference frame) and isotachs (lines of constant windspeed).

Satellite-derived cloud displacements provide a new kind of wind measurement. Thus, it is possible to consider new techniques for determining vorticity and divergence. The next section describes such a technique based on first principle definitions of the parameters. It is a technique only; it uses the same basic input, $\vec{V}$. In theory all techniques yield the same values. In practice, however, the first principle method may have computational advantages when used with satellite data.

Method

Given:

(a) field of cloud displacement vectors, $\vec{V}_i$

(b) in a cartesian (i.e., line/element) coordinate system

(c) with values, X_i, Y_i locating the midpoints of each $\vec{V}_i$ and values a_i, b_i defining the start points and c_i, d_i the endpoints of each $\vec{V}_i$

$$\vec{V}_i$$

$$c_i, d_i$$

$$x_i, y_i$$

$$a_i, b_i$$

The area, A_N, of the irregular, n-sided polygon (Fig. 1) formed by the midpoints x_i, y_i is given by:

$$A_N = \frac{\left| \sum_{i=1}^{i=N} y_i(x_{i+1} - x_{i-1}) \right|}{2} \tag{3}$$

where $|\ |$ denotes an absolute value and $i = 0 \equiv i = N$; $i = 1 \equiv i = N + 1$.

Horizontal divergence, DIV_2V, is defined as the relative rate of change in an area (i.e., A_N) bounded by given air parcels or tracers (i.e. clouds). Thus:

$$DIV_2V = \frac{1}{A_N} \frac{dA_N}{dt} [t^{-1}] . \tag{4}$$

From a field of cloud displacement vectors $\vec{V}_i$ derived from two satellite pictures Δt seconds apart, we use (3) and (4) to obtain:

$$(5) \qquad DIV_2V = \frac{\left|\sum_{i=1}^{i=N} d_i(c_{i+1} - c_{i-1})\right| - \left|\sum_{i=1}^{i=N} b_i(a_{i+1} - a_{i-1})\right|}{\left(\left|\sum_{i=1}^{i=N} b_i(a_{i+1} - a_{i-1})\right|\right) \cdot \Delta t}$$

Δt in seconds

Typical values of DIV_2V on a synoptic scale (10^2 - 10^3 km) in the atmosphere are 10^{-5} sec^{-1} (smaller at some levels). This is equivalent to a one percent area change in sixteen minutes.

Relative vorticity, ζ, is circulation per unit area. For a small area, A_N:

$$(6) \qquad \zeta = \frac{C}{A_N} \frac{\oint \vec{V}_i \cdot \vec{d}_S}{A_N} \quad [t^{-1}].$$

where $\oint$ signifies a line integral around the (ideally circular) area A_N (Fig. 2) and $\vec{dS}$ represents both the magnitude (distance) and position of a segment on the perimeter of A_N.

From a field of cloud displacement vectors as in Fig. 2, with A_N defined at the midpoints (x_i, y_i) of $\vec{V}_i$, we may evaluate (6) to obtain ζ at time $t = 1/2\ (\Delta t)$:

$$(7) \qquad \zeta = \frac{\sum_{i=1}^{i=N} |(V_i) \cdot (dS_i)| \cdot \cos\theta_i}{A_N}$$

$$V_i = e/\Delta t$$

$$dS_i = 1/2\ (a+d)$$

$$\cos\theta_i = (b^2 + a^2 - c^2)/2ab$$

$$a = \sqrt{(x_{i+1} - x_i)^2 + (y_{i+1} - y_i)^2}$$

$$b = \sqrt{(x_i - a_i)^2 + (y_i - b_i)^2}$$

$$c = \sqrt{(x_{i+1} - c_i)^2 + (y_{i+1} - d_i)^2}$$

$$d = \sqrt{(x_{i-1} - x_i)^2 + (y_{i-1} - y_i)^2}$$

$$e = \sqrt{(a_i - c_i)^2 + (b_i - d_i)^2}$$

From (3) we set $A_N = \frac{1}{2}\left[\left|\sum_{i=1}^{i=N} f\right|\right]$ with $f = y_i(x_{i+1} - x_{i-1})]$

$$(8) \qquad \zeta = \sum_{i=1}^{i=N}\left[\left|\left(\frac{e \cdot (a+d)}{\cdot \Delta t}\right)\right| \cdot \left(\frac{b^2 + a^2 - c^2}{2ab}\right)\right]_i \Big/ \left|\sum_{i=1}^{i=N} f\right|$$

Δt in seconds

Summary

We plan to compute ζ and DIV_2 from the techniques based on first principles (Eqs. (5) and (8)) and to compare the resulting values and ease of computation with the more conventional methods.

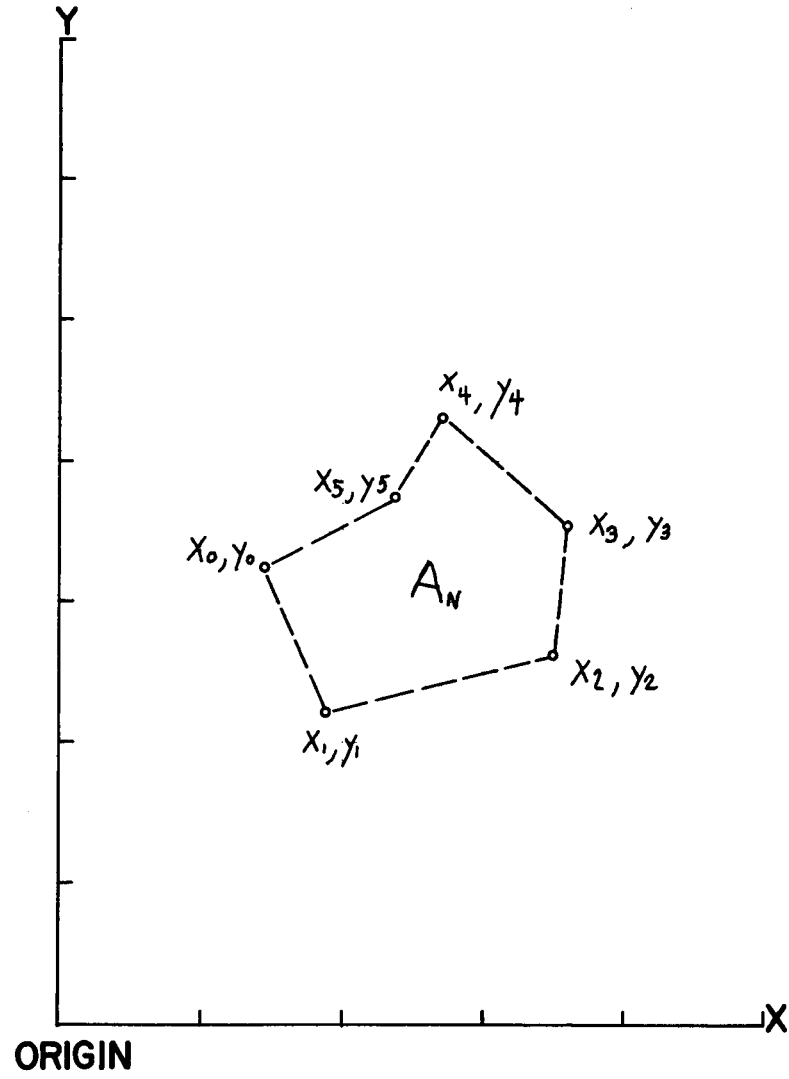

FIG 1

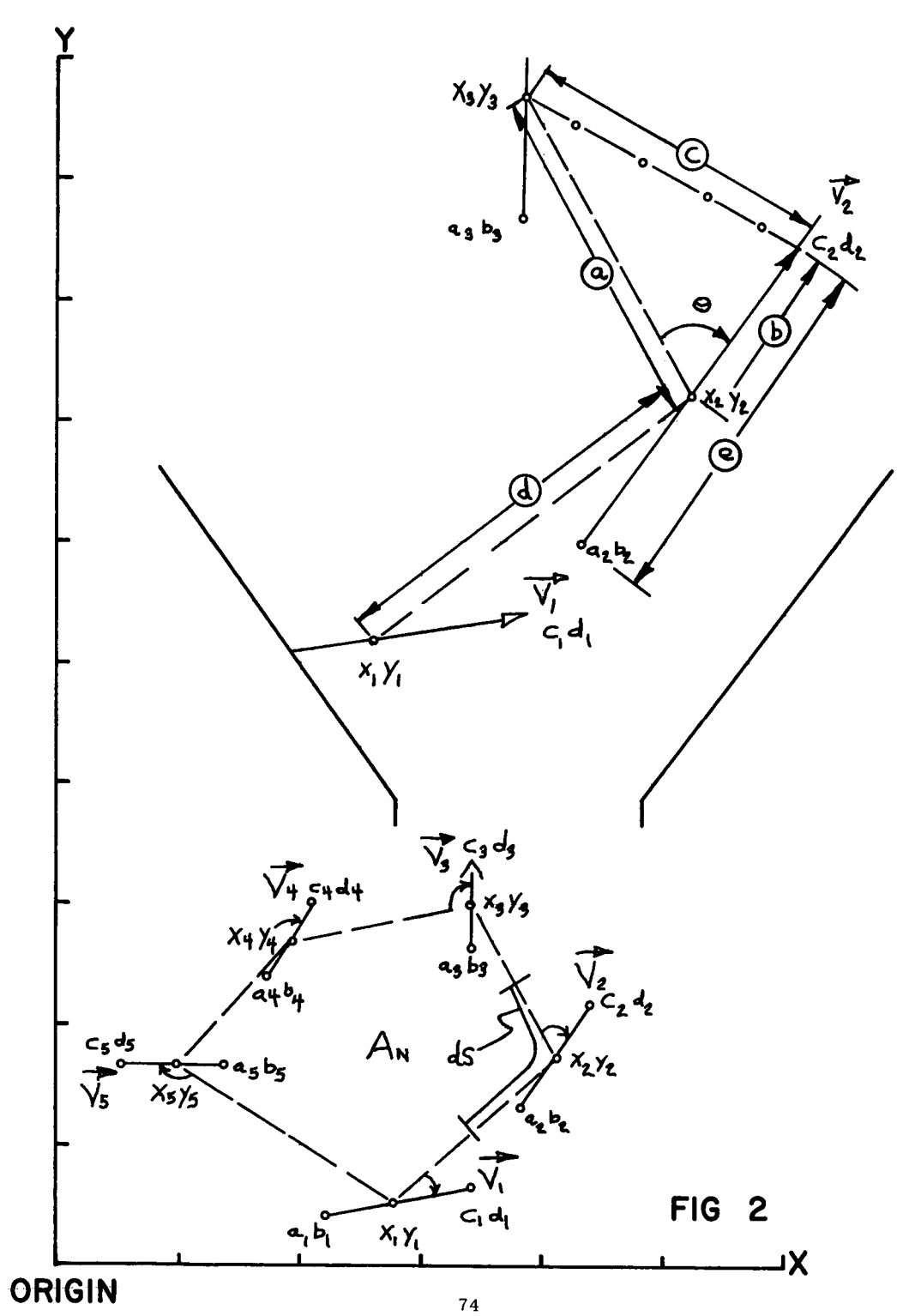
Y
X
ORIGIN
$X_3 Y_3$
$a_3 b_3$
$\vec{V}_2$
$C_2 d_2$
a
b
c
d
e
θ
$X_2 Y_2$
$a_2 b_2$
$\vec{V}_1$
$C_1 d_1$
$X_1 Y_1$
$\vec{V}_3$ $C_3 d_3$
$\vec{V}_4$ $C_4 d_4$
$X_4 Y_4$
$a_4 b_4$
$X_3 Y_3$
$a_3 b_3$
$\vec{V}_2$
$C_2 d_2$
$C_5 d_5$
$a_5 b_5$
$\vec{V}_5$
$X_5 Y_5$
A_N
dS
$X_2 Y_2$
$a_2 b_2$
$\vec{V}_1$
$C_1 d_1$
$a_1 b_1$
$X_1 Y_1$

FIG 2

TIME VARIATION OF TROPICAL ENERGETICS AS VIEWED FROM A GEOSTATIONARY ALTITUDE

D. N. Sikdar and V. E. Suomi

Abstract:

In this paper we have used time-lapse ATS-I satellite cloud photographs as our data source for the evaluation of the convective transport of latent heat from the lower troposphere to the tropical upper troposphere.

The analysis reveals that the meso- to sub-synoptic-scale convection systems over the tropical mid-Pacific are well organized on a time scale of a few days and are controlled by the large-scale motion field. The time variation of this heat transport, in the sector 120W-180W, 15N-15S, indicates an approximate periodicity of five days. Furthermore, this pulsating feature seems to be tied to a wave-like disturbance field of wavelength nearly 75° of longitude and moving westward with an approximate speed of 15° of longitude per day.

Introduction

The dynamics of large-scale tropical disturbances and their interactions with mid-latitude circulations has been limited by lack of observations on an appropriate space scale. Riehl (1945, 1948) first pointed out the existence of "easterly waves" in the lower tropical troposphere based on synoptic data in the Caribbean Sea region. Over the tropical Pacific, Palmer (1952) found similar types of disturbances and classified them as "equatorial waves." The wavelength of these disturbances is stated to be of the order of 2000 km - 3000 km. Yanai and Nitta (1967) pointed out that these wave systems exhibit systematic upward motions to the east of the wave axis.

Tropical upper tropospheric circulations were first reported by Riehl (1948). He found large eddies in the upper troposphere at ~ 200 mb over the western Pacific. These eddies are seen to move westward with a phase velocity close to the speed of lower easterlies. Recently, Yanai and Maruyama (1966), had studied these tropical upper tropospheric disturbances in detail and detected westward-moving waves over the equatorial Pacific despite the general flow field being eastward at those levels. The wavelength of these disturbances is estimated to be around 10, 000 km. Based on the power spectral analysis of upper tropospheric wind data over the tropical Pacific (150W to 150E) for the period April to July 1962, Yanai et al. (1968) reported a significant peak of power spectral density of the meridional wind component at four-to-five-day periods. These high-level spectral density peaks are related to the traveling large-scale disturbances.

Based on these findings one might ask if there is a relationship between these westward-moving tropospheric perturbation fields and the intensity of tropical convection. In the tropics, a major part of the heat is transported from the boundary layer to the tropical upper troposphere by deep "wet" convection and then in the form of sensible heat and potential energy to the higher latitudes. The purpose of this paper is to show that tropical convective activity as revealed by the geosynchronous satellite cloud photographs also has a strong periodic fluctuation.

This analysis covers the period 1–30 April 1969 during the Line Island Experiment. Frequent satellite pictures and additional surface and upper air observations were available.

On the Scales of Convection in the Tropics

In tropical circulations, three broad scales of motion are mainly involved: 1) planetary scale (the equatorial trough and trade-wind regime, subtropical highs and jets, the tropical monsoon, etc.); 2) synoptic- or large-wave scale (easterly waves, tropical cyclones, waves in the upper troposphere, etc.); 3) meso-convective scale (cumulus clouds which can form cloud clusters).

Figure 1, taken from the February 1970 GARP technical report, clearly explains these scales. On the meso-convective scale (10 km - 100 km) one identifies individual cumulonimbus towers (1 km - 10 km) surrounded by clear space on the satellite photographs. On the cloud-cluster scale (100 km - 1000 km) there may exist a number of meso-convective-scale convective areas in proximity so that the high-level cirrus outflows in their mature and decaying stages merge to form a common cirrus shield. These scales are found embedded in a large-wave scale.

The half-globe cloud picture (Fig. 2) taken from ATS-III shows the cloud population on a day in July 1969 over the Atlantic. Various scales of convec-

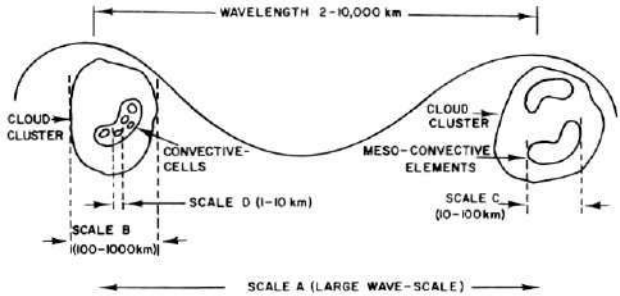

Fig. 1. The scales of tropospheric motions in the tropics.

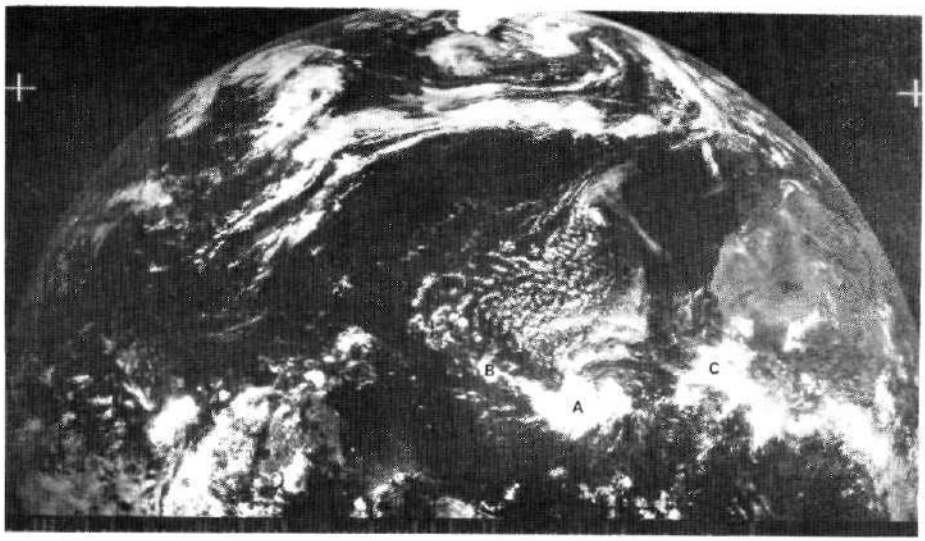

Fig. 2. ATS-III (half-globe) cloud picture over the Atlantic on a day in July, 1969.

tion can be easily identified on this photograph. Bright clouds marked A, B and C can be categorized as the cloud-cluster scale.

Figure 3 is an enlargement of cloud cluster A in which one would anticipate the presence of a number of active deep meso-convective-scale convections. ATS satellites easily observe the composite cirrus canopies resulting from these deep convection cells. If one enhances the brightest portion of the photos, zones of deep convection can also be identified. Figure 4 is an example photograph emphasizing the bright parts of cloud cluster A (Fig. 2), i.e., the deep portion of the cloud cluster. This picture suggests that the deep-convection cells occupy a small area and they exist more or less around the geometric center of a cloud cluster.

Cirrus canopies observed at the top of these deep convection cells have a lifetime much greater than the lifetime of a cloud cluster, so that the time variations in their areas can be excellent markers for the convective energy

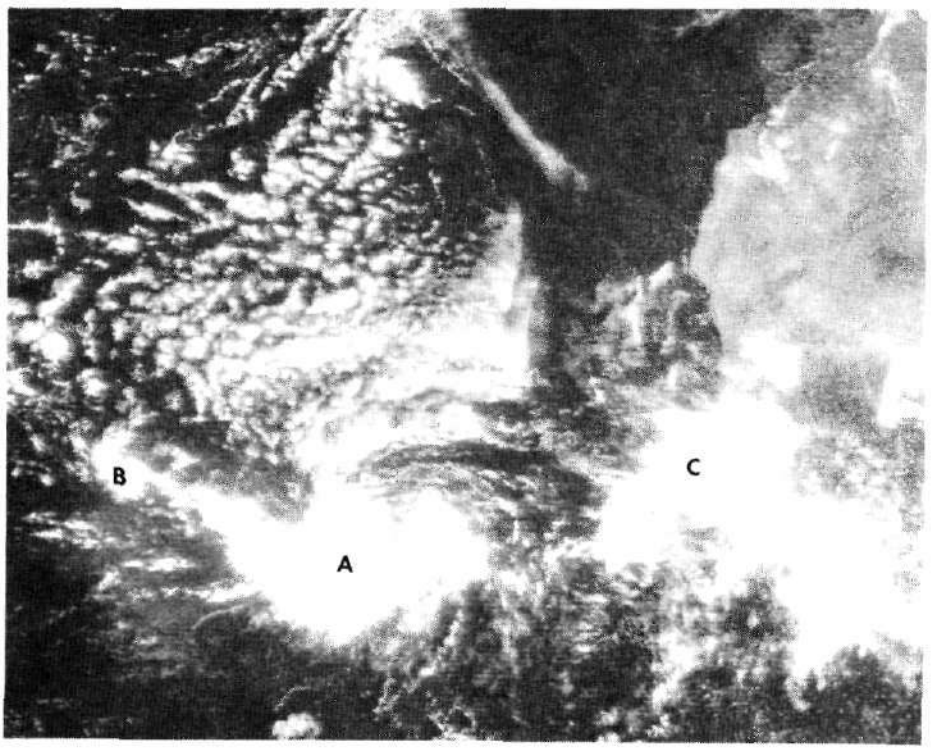

Fig. 3. Enlargement of cloud-cluster A in Fig. 2 (not to scale)

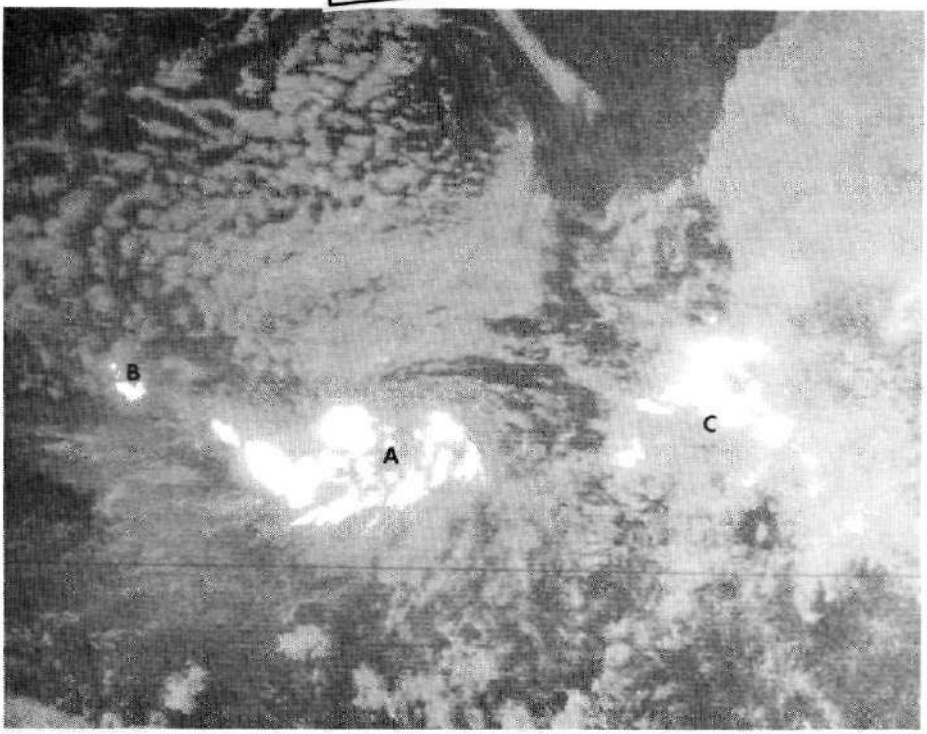

Fig. 4. High-level enhancement of cloud-cluster A in Fig. 2 (not to scale)

transport to the tropical upper troposphere (Sikdar and Suomi, 1969). In order to evaluate these transports we have used the three-layer convection model (I) shown in Fig. 5. This model is similar to what Green et al. (1966) had presented for large-scale convective circulation.

A Brief Physical Description of the Model Used

As already pointed out, a cloud cluster may be regarded as an envelope of deep convection occurring in regions of organized rising motion associated with the large-wave scale. A deep tropical convection is essentially made up of three layers (Model I, Fig. 5). First, the layer of inflow (LIF) which includes the planetary boundary layer that extends from the sea surface to the lifting condensation level (LCL). In this layer, warm moisture-laden air is drawn into the cloud region because of the local convergence which might be produced by large-scale motion. The second layer, the layer of vertical

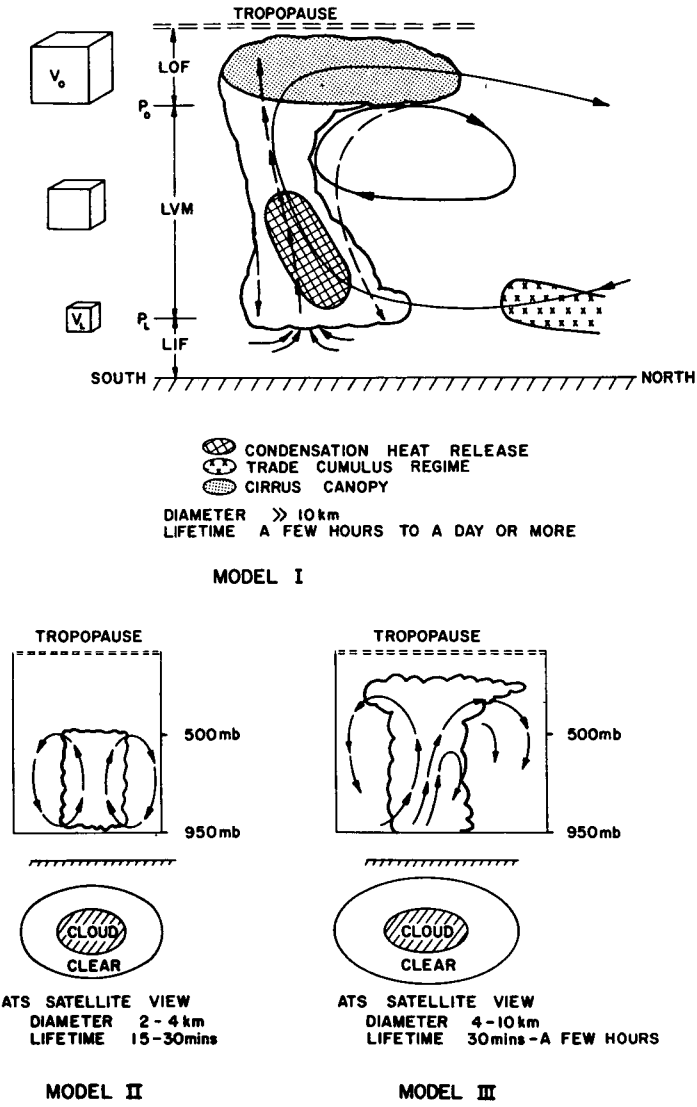

Fig. 5. Schematic diagrams for convection models of various scales

motion (LVM), has a depth from the LCL to the throat of a convective tower in which the vertical motion is maximum at the core decreasing to a negligible value at the cloud periphery. It is assumed that the buoyant air starts condensing at the LCL and the heat of condensation thus released is conserved in the rising volume. The third layer is the layer of outflow (LOF), that between the throat and the tropopause in which clouds diverge in the form of cirrus plumes. The cloud divergence in this layer is analogous to the horizontal spread of smoke particles in the atmosphere when a rising plume strikes a stable layer. The mean thickness of a cirrus shield atop a cloud cluster has been assumed as 1.0 km following Ludlum (1966), Borovikov et al. (1963) and Anderson.[1] In this model the amount of rain ought to be related to the amount of cirrus present. We know this is true qualitatively and are now trying to quantify this relationship.

While it is possible to derive information on the convective mass and heat transport to the tropical upper troposphere, the proposed convection model does not treat the compensation current in the cloud environment explicitly. Nevertheless, an observed aperiodic or periodic fluctuation in the cirrus canopy and a lifetime much longer than a few hours suggests an unsteady convective circulation associated with cloud-cluster-scale convection, and the air evicted aloft of a deep convection zone does not descend in the immediate vicinity but is removed at considerable distances. Mass continuity is provided by convergence essentially in the planetary boundary layer and "all the air originating in the updraft remains in the upper troposphere, spreading out mainly in the anvil plume downshear but appreciatly also in the upshear side" (Newton, 1966).

In a small-scale convective circulation (cumulus congestus) as shown in Model II of Fig. 5, there is hardly any outflow seen on the satellite photographs because rapid mixing with the dry environment inhibits their growth and a clear space is usually evident around them. In the case of an isolated deep convective circulation (Model III) the solenoid field is maintained as long as the colder air with lower moisture content, originating at some levels in the mid-troposphere (Newton, 1966), does not enter the center of the storm. As soon as this cold air current develops in the descending branch both inside and outside of these cells, clear spaces appear around these cells on satellite time-lapse photographs. Such a cloud circulation is often seen in isolated severe thunderstorms in mid-latitude (Sikdar et al., 1970) and also in tropical regions. Model I may be a better representation for the deep-convection cells apparently embedded in a cloud-cluster-scale convection that will be discussed in this paper.

---

[1]Anderson, C. E., 1969: Personal communication.

Ludlum (1963) has also shown that the model for large-scale motion systems is similar to that for well-organized cumulonimbus clouds as observed in a cloud cluster, except that the horizontal scale is very much greater. In large-scale convection, the strongest acceleration appears along the trajectory that passes through the condensation region. From the isentropic relative-flow charts the circulations of large-scale mid-latitude convection can be traced back near the surface into much lower latitudes (Green et al., 1966). The magnitude of this far-region descending branch is mainly determined by the radiative heat loss at higher latitudes. The descent period may be up to twenty days before the current returns to the surface layer in the same latitude. The arms of the descending circulation have been left open to show, in the large-scale flow field in the meridional plane, that the descent continues in other systems and that there is no boundary on that side.

If we use Model I the volume V_0 of a buoyant parcel at the layer of outflow near the cloud top can be related to its volume V_L at the LCL, using the equation of state, in the form

$$V_0 = \left(\frac{P_L T_0}{P_0 T_L}\right) V_L , \tag{1}$$

where suffix 0 and L stand for the base of the outflow layer and the top of the inflow layer, respectively, and P, T are corresponding pressure and temperatures.

With mean values of P_0, P_L, T_0, T_L obtained from upper-air soundings in the environment, one gets an estimate of volume flux at the outflow layer as

$$\frac{dV_0}{dt} = \frac{K}{\rho L} \frac{dM_L}{dt} , \tag{2}$$

where M_L is the mass, ρ_L the density of air at the subcloud layer (1.1×10^{-3} gm cm^{-3}) and is assumed constant for a steady inflow and $K = P_L T_0/(P_0 T_L)$ is a dimensionless constant.

Relating the cloud divergence to cloud area change (Sikdar, 1969) and making use of (2), the mass flux (gm sec^{-1}) at the layer of outflow is given by

$$\frac{dM_L}{dt} = \frac{\rho_L}{K}[A_c \Delta Z(\nabla_H \cdot \mathbf{V}_c)], \tag{3}$$

where A_c is the area of cirrus atop a cloud cluster, and ΔZ the average thickness of the cirrus shield. The term $[A_c(\nabla_H \cdot \mathbf{V}_c)]$ is evaluated from successive ATS-I cloud photographs.

In a deep convective circulation in the tropics, the major source of energy is the water vapor content (the average mixing ratio W is $\sim$ 20 gm kg^{-1} in the planetary boundary layer) flowing into the storm which is almost completely converted to liquid or frozen water through expansional cooling of the air in the updraft. Of this liquid or frozen water, only a fraction falls out as rain (Braham, 1952), with as much as 90% remaining behind as cloud. Cirrus shield air carrying these hydrometeors penetrates deeply into the upper troposphere ($\sim$ 200 mb) where the mixing ratio hardly exceeds 0.1 - 0.2 gm kg^{-1} .

In this model we have assumed that the equivalent temperature at the LCL is constant, and that all the water vapor passes to the condensed phase as it ascends through the cloud core. The latent heat flux (cal sec^{-1}) can be estimated from

$$E_c = L\Delta W \frac{dM_L}{dt} , \qquad (4)$$

where L is 597 cal gm^{-1} at 0C and $\Delta W = (W_{LCL} - W_0)$.

It should be pointed out here that our exclusion of an in-cloud cold downdraft from the proposed flow model will simply reduce our estimates of mass and heat fluxes. The cold air detrained out of the storm bottom was probably entrained from mid-tropospheric levels. Cold air brought down has the same effect on the storm's heat transfer process as does warm air carried aloft.

Analysis of ATS Pictures

A pronounced cirrus outflow resulting from a number of active penetrative convection cells embedded in a cloud cluster can be easily identified on the brightness-standardized ATS time-lapse pictures against isolated low- and middle-cloud backgrounds. A cloud cluster is not a Lambertian reflector, especially at large solar zenith angles (Bartman, 1967); at small angles (+ 30° to - 30°), however, a thick cirrus canopy may closely behave as such a reflector. A systematic analysis of high- and low-level brightness-enhanced pictures shows that while the brightness gradient change of a cloud core is sensitive to solar zenith angle change by 30° or more around local noon, the mean brightness of a cirrus shield hardly exhibits any such difference. In order to avoid any correction for brightness change due to change in solar zenith angle, we have selected satellite pictures over a period of two hours on either side of local noon at the sub-satellite point (0° , 150W), in which period at least ten pictures are obtained provided the satellite maintains a continuous watch. Moreover, since the proposed technique is employed on two successive satellite photographs twenty-three minutes apart, the brightness change due to the change in solar zenith angle $\sim$ 5° in each period may be regarded as insignificant (Sikdar, 1969).

Data Source and Coverage

For reasons mentioned in Section 4, we have selected the region 120W - 180W, 15N - 15S as our study area, and throughout this paper the sections 120W - 180W, 0° - 15N and 120W - 180W, 0° - 15S will be referred to as the Northern Hemispheric Sector (NHS) and the Southern Hemispheric Sector (SHS), respectively. Locations of the conventional surface and upper air stations used in this study are shown in Fig. 6.

The number of daily available ATS-I pictures analyzed are presented in Table 1. Although one can compute convective heat fluxes from two successive satellite photographs twenty-three minutes apart, a longer sequence of pictures and greater observation frequency render higher accuracy in the evaluated magnitudes. Table 1 clearly shows that the number of photographs analyzed in this scheme less than satisfactory except for the period 13 April - 26 April, 1967. Nevertheless, we will present whatever information we could derive from this small data sample.

Results

Time variation of large-scale convective heat fluxes in the tropics

Figure 7 shows the daily average percent cloud cover in the NHS as well as in the SHS for the investigation period. Each data point in this diagram represents the average of many growing and decaying cloud clusters in each

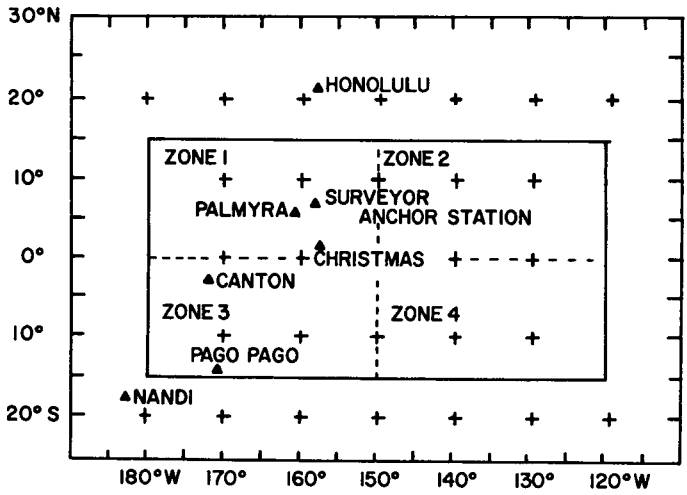

Fig. 6. Location of the radiosonde stations in the grid box under investigation

Table 1

Number of Cloud Photographs Used in the Analyses

Date (April 1967)	Photographs used
1	3
2	8
3	0
4	10
5	3
6	4
7	3
8	4
9	3
10	5
11	2
12	2
13	12
14	11
15	7
16	12
17	12
18	12
19	11
20	11
21	12
22	12
23	13
24	7
25	10
26	11
27	6
28	8
29	4
30	4

grid sector. In addition to a significant day-to-day variation in percent cloud cover, a periodicity of seven to eight days is clearly evident in this diagram.

Figure 8 presents the daily mean of the average convective heat transport to the upper troposphere over the mid-Pacific for April 1967 as computed from the model. These magnitudes are directly proportional to the rate of expansion of cirrus shields at the top of cloud clusters as determined from

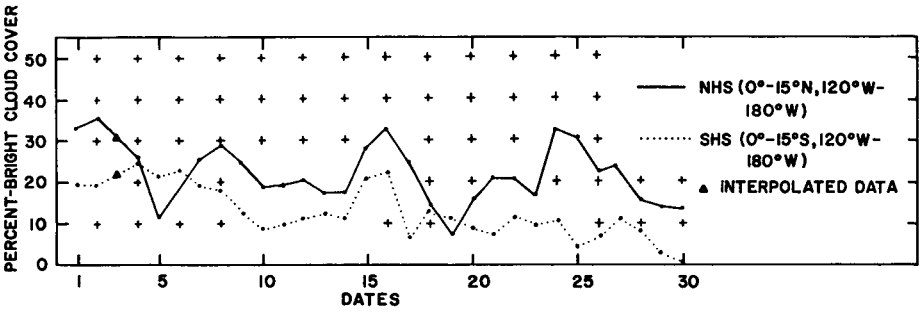

Fig. 7. Daily percent bright cloud cover in April 1967.

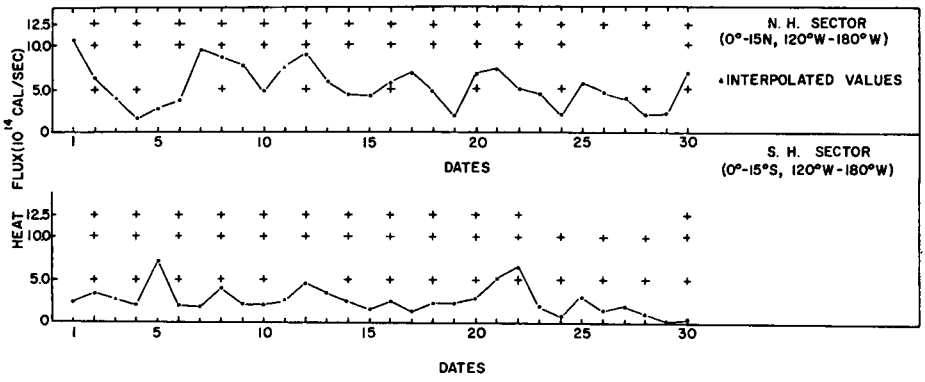

Fig. 8. Daily mean of the convective heat fluxes to the tropical upper troposphere in April 1967 over the central Pacific.

successive ATS pictures. Contrary to the seven- to eight-day periodicity in the cloudiness cycle which involves cloud motion (Fig. 7), Fig. 8 shows an approximate periodicity of four- to five-days in the convective heat release in the NHS, while in the SHS it ranges from four to six days. The absence of sharp sharp peaks in the SHS might be attributed to the weak convective activity there during the study period. Nevertheless, these observations clearly suggest an association between the large-scale convective heat release and large-scale wave disturbances propagating in the tropical troposphere. From the five-day periodic fluctuations one would be inclined to relate the convective activities over the tropical mid-Pacific to the equatorial wave-type disturbances (Palmer, 1950, 1951). Equatorial waves are known to have wavelengths of the order of 2000 km - 3000 km (about 30° of longitude) and have a period of $\sim$ 5 days.

Phase and speed of the upper tropospheric disturbance

Whether the large-scale heat release referred to in the previous section is initiated by upper- or lower-tropospheric disturbance fields, by a boundary-layer phenomenon, or by some combination of all cannot be determined using present conventional data. However, one may be able to determine from satellite photographs whether the wave pattern indicated in Fig. 8 moves eastward or westward.

In order to determine the pattern motion the convective fluxes were computed in longitudinally separated grid zones, 120W - 150W, 150W - 180W in the two hemispheric sectors. The new grids are shown in Fig. 6 by broken lines. The computed energy release (weighted over the respective grid sector) was plotted for each zone as a function of time in Figs. 9 and 10, respectively. The most spectacular change from Fig. 8 is the appearance of sharper peaks at a four- to five-day interval in all zones. A smaller longitudinal grid box is a sharper phase filter for longitudinal wave motions.

Starting with t = 0 on 4 April, 1967 in Figs. 9 and 10, one finds that the first maximum of energy flux density appears in zone two in the NHS. After two days the maximum appears in zone one. The same feature is observed in the SHS as well. Apparently a wave disturbance travels westward in both hemispheric sectors. There is a phase difference of two days in the appearance of a maximum between the eastern and western portions of the Northern Hemisphere zone and a similar but less distinct phase difference between the eastern and western portions of the Southern Hemisphere zone. When we assign the phase difference to the center-to-center distances between the zones we obtain a wave disturbance speed of 15° of longitude per day. The five-day period yields a wavelength of 75° of longitude.

Figures 11 and 12 present the time cross-sections for cloud cover in each 5° latitude belt in the grid zone under investigation for April 1967, prepared from the ESSA III computer mosaics. Westward propagation of clouds is clearly evident on these photographs. Also, from the slope of the cloud lines one computes the speed of the cloud field as 6° - 7° of longitude per day. Thus, the phase speed of the release of convection is more than twice the speed of the cloud field motion observed in Figs. 11 and 12. Yanai et al. (1968) also found a similar phenomenon involving the upper tropospheric meridional component in the same region and season but for a different year.

Furthermore, by superimposing the upper wave pattern in Fig. 9 on the upper wave pattern in Fig. 10 (western region), one finds a phase difference of two days in the maxima, with the one in the SHS leading, during the period 4 - 18 April 1967. This phase difference decreased to one day in the case of the fourth maximum and disappeared thereafter. In the eastern sector, on the other hand, a two-day phase difference is discernible for the period 4 - 16 April after which no significant difference can be found. The cloud

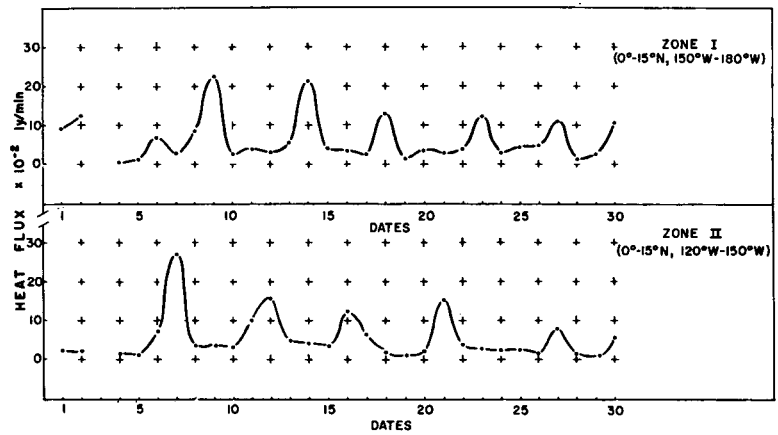

Fig. 9. Latent heat fluxes in zones I and II in the Northern Hemispheric sector for April 1967.

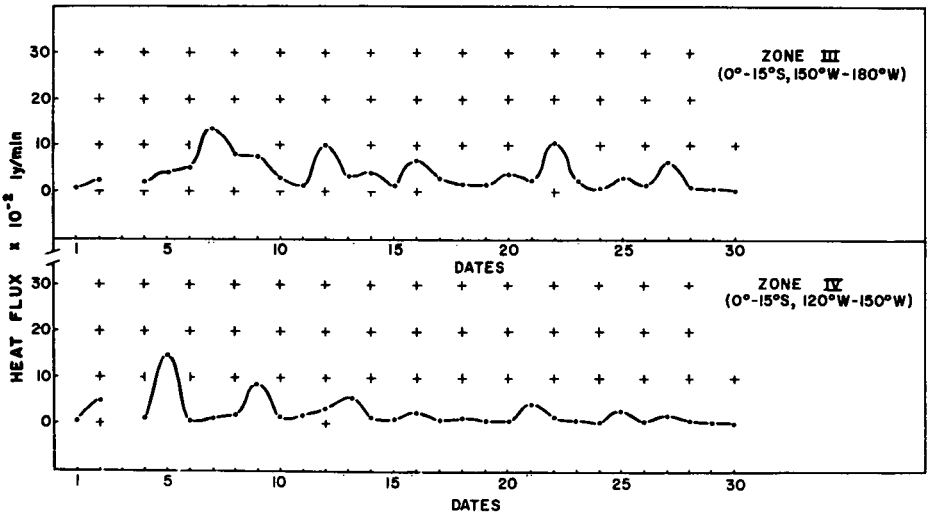

Fig. 10. Latent heat fluxes in Zones III and IV in Southern Hemispheric sector for April 1967.

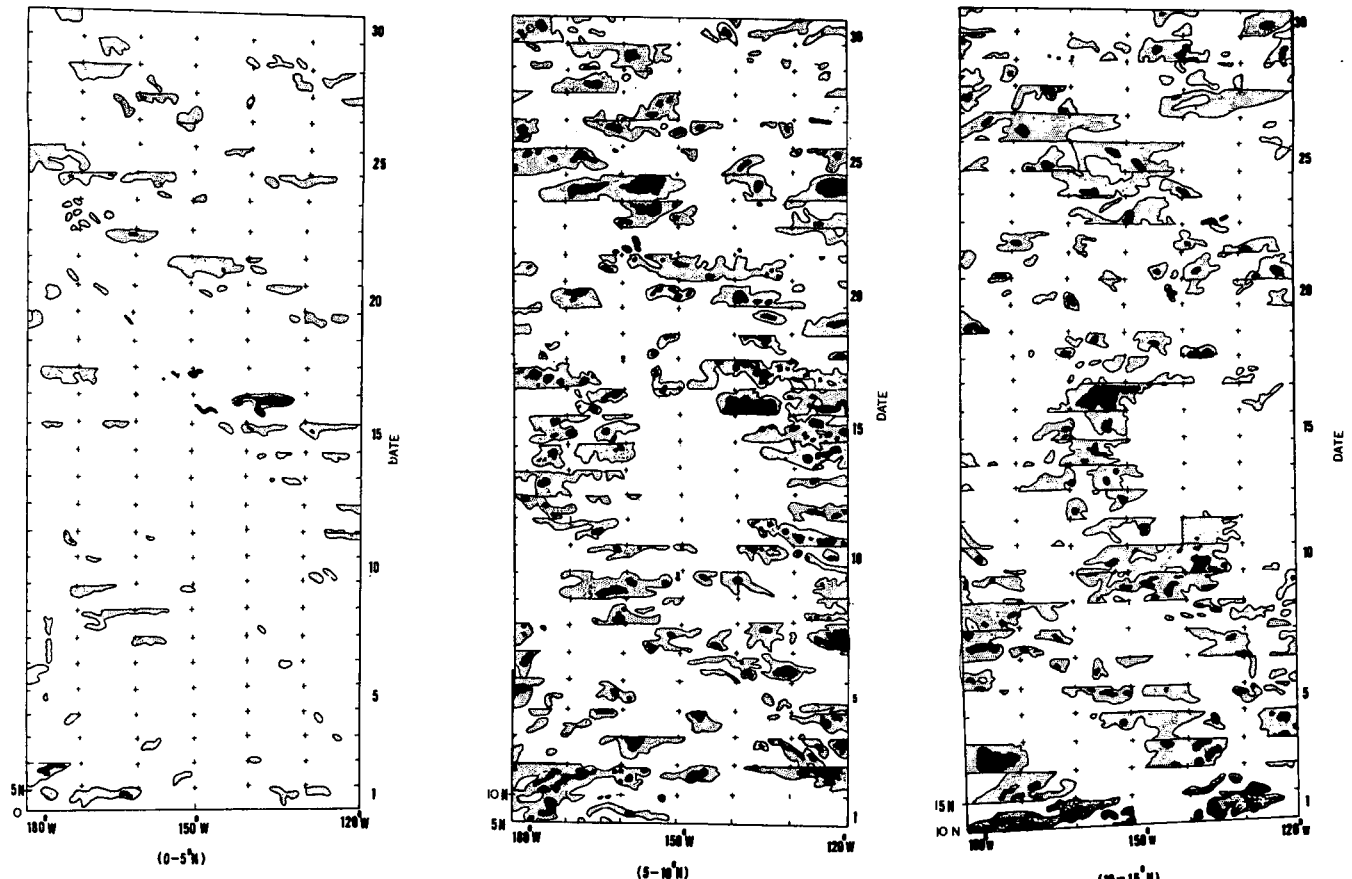

Fig. 11. Time cross-sections of cloud field in 5° latitude belts in the Northern Hemisphere sector (0° - 15N) for April 1967, prepared from ESSA III mosaic. Brighter cloud regions are darkened.

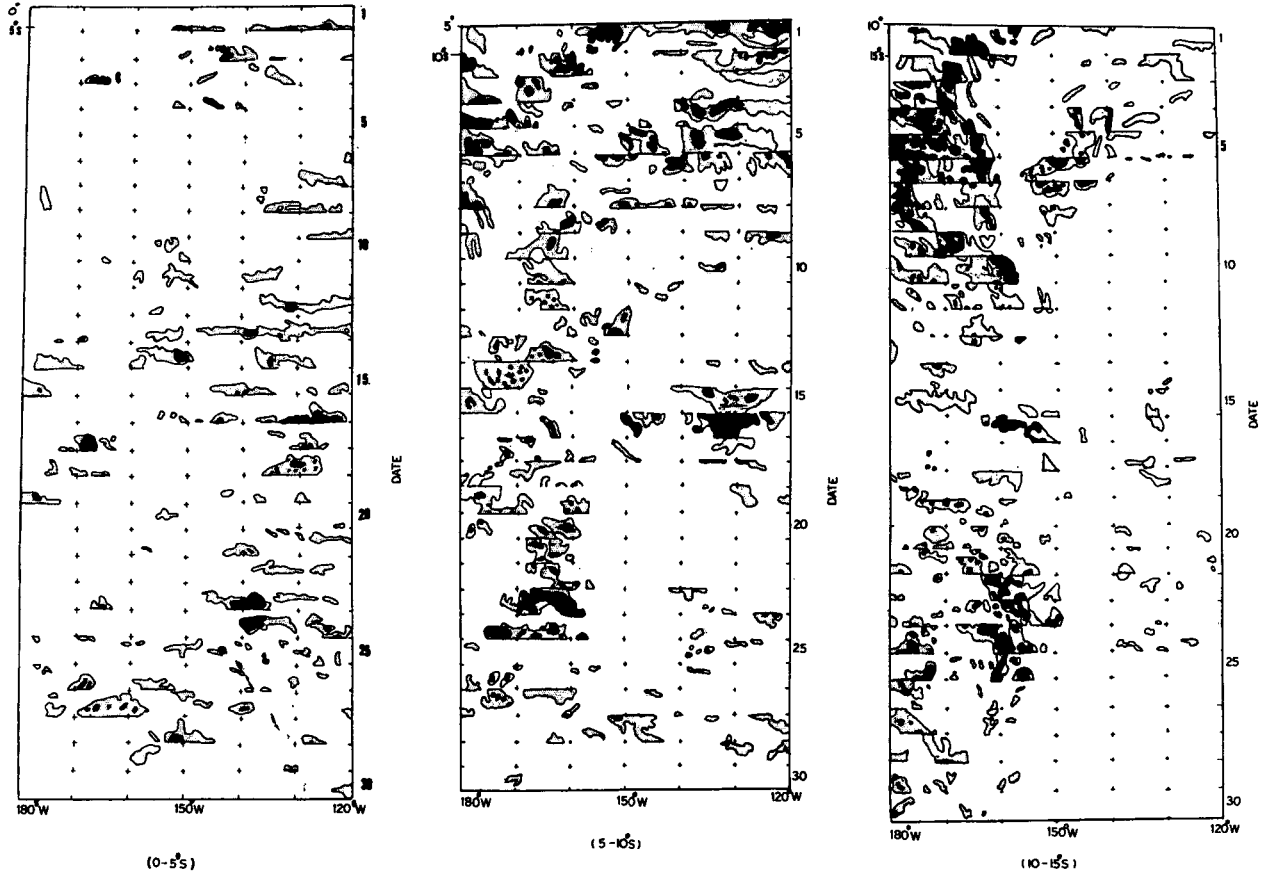

Fig. 12. Same as Fig. 11 except for the Southern Hemispheric sector (0° - 15S).

population in the eastern region of the SHS was probably inadequate to reflect the persistence of this feature. The phase relationship between the cited tropospheric disturbance fields across the equator in this short-period study is also suggestive of a mixed Rossby-gravity wave (Matsuno, 1966). These findings therefore suggest that the convective heat release to the tropical upper troposphere over the central Pacific is associated with the mixed Rossby-gravity wave mode[2] rather than the equatorial wave type disturbance of Palmer (1951). The existence of westward-moving waves of planetary scale over the Pacific has been further substantiated by a spectrum analysis of a long series of cloud data (Sikdar et al., 1970).

7. Summary and Conclusions

In this paper we have shown, subject to some reasonable assumptions, that one can extract quantitative information on the cloud dynamics of the tropical atmosphere from geosynchronous satellite time-lapse cloud photographs. This short-period analysis suggests the following tentative conclusions:

1) In the tropics large-scale convective activity pulsates with an approximate periodicity of five days.

2) The cloud-cluster scale convection systems are well-organized on a time scale of a few days and are probably coupled to the large-scale meridional circulations.

3) The periodic excitation of the large-scale convergence field in both hemispheric sectors seems to be associated with a wave-like disturbance having a wavelength of 75° of longitude, moving westward with an approximate speed of 15° of longitude per day in the troposphere.

4) The westward cloud motion, as evident on the time cross-section, seems to have no relation to the westward propagating large-scale tropospheric disturbance field presented in this paper.

5) A phase difference of nearly two days is indicated (for a part of the study period) between moving disturbances north and south of the equator; for the remainder of the period no significant difference can be found.

---

[2]Recently Hayashi (1970) reported in a theoretical paper that when the release of latent heat due to moist convection in the upper troposphere exceeds a critical value, unstable waves of free internal mode come into existence whose growth rate increases with the increasing heat. He found that mixed Rossby-gravity waves were the most unstable mode, and that a wavelength of 10,000 km coincided with a period of about four days. Our observations appear to be in line with this finding.

One of the key problems in models of the tropical atmosphere is to account for the heat release by convection, a phenomenon whose space scale is much smaller than the grid mesh used in the model. The statistics from this study have clearly shown that the release of convection in the tropics, at least in the region under investigation, is not random and is controlled by the large-scale motion. In view of the findings for this limited time sample, one is tempted to believe that the determination heat release in the sub-mesh convective scale may be possible from a knowledge of the large-scale motion field in the tropics. Further investigation in this area is underway.

Acknowledgments

The authors wish to thank the National Aeronautics and Space Administration for supporting this research under Contract NAS5-11542, and David Cadle and John Riggs of the Space Science and Engineering Center Photographic Laboratory for their efforts in producing the brightness-standardized gridded enlargements of the photographs used in this research.

References

Bartman, F. L., 1967. "The reflectance and scattering of solar radiation by the earth," NASA Rept. NAS-54(03).

Borovikov, A. M. et al., 1963. Cloud Physics. Translated by Israel Program for Scientific Translation. Available from the office of Tech. Service, U. S. Dept. of Commerce, Washington, D. C.

Braham, R. R., Jr., 1952. "The water and energy budgets of the thunderstorm and their relation to thunderstorm development." J. Meteor, 9, 227-242.

Green, J. S. A., Ludlum, F. H. and McIlveen, J. F. R., 1966. "Isentropic relative flow analysis and the parcel theory," O. J. Met. Soc., 210-219.

Hayashi, U., 1970. "A theory of large-scale equatorial waves generated by condensation heating and accelerating the zonal wind," J. Meteor., Soc. Japan, 48, 140-160.

Ludlum, F. H., 1963. "Severe local storms: A review," Meteor. Mongr., 5, No. 27, 1-28.

_____, 1966. "Cumulus and cumulonimbus convection," Tellus, 18, 687-698.

Matsuno, T., 1966. "Quasi-geostrophic motions in the equatorial area," J. Meteor. Soc. Japan, 46, 215-222.

Newton, C. W., 1966. "Circulations in large sheared cumulonimbus," Tellus, 18, 699-713.

Palmer, C. E., 1951. "Tropical meteorology," Compendium of Meteorology, Boston Amer. Meteor. Soc., 859-880.

_____, 1952. "Tropical meteorology," Quart. J. Roy. Meteor. Soc., 78, 126-163.

Riehl, H., 1945. "Waves in the easterlies and the polar front in the tropics," Dept. of Meteorology, The University of Chicago, Misc. Rept. 17, 79 pp.

_____, 1948. "On the formation of west-Atlantic Hurricanes," Dept. of Meteorology, The University of Chicago, Misc. Rept. 24, 1-64.

Sikdar, D. N., 1969. "Convective heat transport over the tropical mid-Pacific as estimated from a geosynchronous satellite altitude," Ph. D. thesis, Dept. of Meteorology, The University of Wisconsin, Madison.

_____, and Suomi, V. E., 1969. "An objective technique of evaluating mesoscale convective heat transport in the tropics from geosynchronous satellite cloud photographs," Studies in Atmospheric Energetics based on Aerospace Probings, Ann. Rept. 1968, Dept. of Meteorology, The University of Wisconsin, Madison.

_____, Young, J., and Suomi, V. E., 1970. "Time-spectral characteristics of large-scale cloud systems in the tropical Pacific," (submitted for publication to Journal Atmos. Sci.).

_____, Suomi, V. E., and Anderson, C. E., 1970. "Convective transport of mass and energy in severe storms over the United States—An estimate from a geostationary altitude," Tellus, 22, 521.

Yanai, M., and Maruyama, T., 1966. "Stratospheric wave disturbances propagating over the equatorial Pacific," J. Meteor. Soc. Japan, 44, 291-294.

_____, and Nitta, T., 1967. "Computation of vertical motion and vorticity budget in a Caribbean easterly wave, J. Meteor. Soc. Japan, 45, 444-466.

_____, et al., 1968. "Power spectra of large-scale disturbances over the tropical Pacific," J. Meteor. Soc. Japan, 46, 801-816.

ON THE POSSIBILITY OF PREDICTING THE DEVELOPMENT OF CLOUD CLUSTERS FROM THE LARGE-SCALE WIND FIELD USING GEOSTATIONARY SATELLITE PICTURES

A. Frederick Hasler

1. INTRODUCTION

Before the advent of geosynchronous satellite photographs and computer composite satellite pictures covering large areas of the earth, only a crude description of the tropical oceanic cloud field and its change with time was possible. Since these advances in our observational system have been made, the picture of this region has been much improved. One of the most important observations made from these pictures is the existence and behavior of cloud clusters.[1] The cloud cluster consists of a group of cumulus and cumulonimbus clouds with vertical dimensions of up to 10 km. or greater and horizontal dimensions of approximately 250 km. to over 1000 km. Cloud clusters occur primarily over the tropical oceans. They have a preferred location along the intertropical convergence zone and they appear in the mean as the intertropical cloud bands shown by Kornfield et al. (1967) and Kornfield and Hasler (1969), but may also occur outside this region. Perturbations in the wind field due to cloud clusters are not as well defined as those in tropical storms. Simpson et al. (1967) say that "no marked perturbation of the wind field occurred in the lower troposphere" as a result of a study of 500 km. × 500 km. cloud clusters which were observed in early satellite pictures of the Caribbean. Cloud clusters may deepen into tropical depressions,[2] but more often they do not develop a closed circulation at any level. Cloud clusters probably provide the major portion of vertical heat and moisture transport from the sub-cloud layer to the upper troposphere in the tropics. If this is true they must be the "Hot Towers"

---

[1] The term cloud cluster was adopted by the Joint GARP Organizing Committee (1969).

[2] Observations from satellite pictures indicate no substantial difference between an ordinary cloud cluster and one which later develops into a hurricane or typhoon.

which Richl and Malkus (1958) have described. For this reason it is very important that cloud clusters be treated accurately in any tropical model. However present numerical models do not handle them well; in fact: "The principal shortcoming in present numerical models in the tropics is their failure to deal adequately with the tropical systems containing the cloud cluster."[1] The global numerical models can handle only the large-scale motion in the tropics. Cloud clusters on the other hand range down to the small-scale and their active portions are even smaller. If the relationship between the large-scale motion field and the development of active portions of the cloud cluster can be determined, then a large first step will have been made toward parameterization of the small-scale processes in the tropics.

The geosynchronous satellite pictures provide a nearly ideal tool for the measurement of short period change in the cloud field in the tropics. The pictures contain both information on the area change and activity of clouds and cloud clusters and information on their motion. One obvious use of the pictures is to attempt to relate these two quantities. If in addition the cloud motions are highly correlated to the wind field, a quantity used by the numerical models, the pictures can be used to test the treatment of cloud clusters by the models. Preliminary studies by Fujita et al. (1969), Hasler et al. (1968), and Hubert[2] indicate that the cloud motions are highly correlated to the wind field. The exact level of the clouds cannot be determined from the satellite pictures at present, but these studies indicate that the derived winds may be assigned to 1,000m. - 2,000m. (850 mb.) for low-level clouds and to about 10,000m. (300 mb) for high-level clouds. Future satellites will be able to measure cloud height as well.

2. RESEARCH PROPOSAL

First the techniques and basic assumptions necessary to test the thesis hypotheses are listed. Then the primary objectives of further work are outlined in brief. Finally the thesis hypotheses are stated and a plan of approach is presented.

2.1 Techniques and Basic Assumptions

a. I have developed techniques to obtain cloud trajectories quantitatively from ATS-I and ATS-III pictures.

---

[1] Plan for U. S. participation in GARP (1969).

[2] "Wind estimates from geostationary satellites" (Presented at American Meteor. Society Meeting, New York, January 1969).

b. It will be assumed that relatively small cumulus clouds (< 20 km.) make good tracers of the wind field at 1000m. - 2000m.

c. It will be assumed that pieces of cirrus material make good tracers and that their trajectories are highly correlated to the wind field at 10, 000m. Note: Henceforth the cloud trajectory field will be referred to as the low-level wind field (1000m. - 2000m.) or the upper-level wind field (10, 000m.).

d. It will be assumed that there is a sufficient number of cumulus tracers to determine the low-level wind field at a resolution of 500 km. × 500 km. or better in the tropics. However, cirrus tracers are much more rare and can be used only in limited areas to determine the upper-level wind field.

e. I have developed techniques for measuring the convergence and vorticity of the low-level and upper-level wind field from the cloud trajectory field. The convergence measuring technique uses the area change of a polygon with a cloud at each of the vertices. The technique to measure vorticity approximates $\oint \frac{\vec{V} \cdot \vec{ds}}{A}$ around the polygon.

f. It will be further assumed that I can carry out the measurements of the wind field and its convergence and vorticity with sufficient accuracy to be able to relate these quantities meaningfully to the cloud clusters.

2. 2 Primary Objectives

a. To confirm the assumptions made in 2. 1.

b. To determine whether a relationship can be found between the convergence and vorticity of the large-scale, low-level wind field and the cloud clusters.

c. To determine relationship of convergence and vorticity at three different horizontal size scales.

1. Maximum resolution (The maximum resolution depends on the number of good tracers per unit area. Over limited areas the maximum resolution may be as good as 100 km. × 100 km.)

2. 500 km. × 500 km.

3. 1500 km. × 1500 km.

d. To determine whether a simple model of the low-level wind field around a cloud cluster can be constructed.

2.3 Thesis Hypotheses

a. That convergence and vorticity maximums in the large-scale, low-level wind field are associated with active cloud clusters.

b. That the convergence and vorticity of the large-scale, low-level wind field is correlated to the development of active cloud clusters.

2.4 Plan of Approach

a. The convergence and vorticity measuring techniques will be applied on three different space scales (maximum resolution, 500 km. × 500 km., 1500 km. × 1500 km.) to a number of different cloud clusters throughout their lifetimes.

b. Conventional data will be used whenever possible to test the assumption of correlation between cloud trajectories and the wind field.

c. All other assumptions will be tested as completely as possible.

d. A complete error analysis will be conducted on the resulting data.

e. The resulting data will be used to achieve the thesis objectives and test the thesis hypotheses.

3. TECHNIQUES

A detailed description of the techniques developed to date is contained in this section. The original "Blink" paper by Hasler et al. (1968), included in the appendix, is referred to for some of the basic techniques. Changes in the "Blink" technique and additional techniques necessary to obtain a complete quantitative description of the vector field from the satellite pictures are then described. Finally, a technique to measure divergence and a technique to measure vorticity from the vector field are outlined.

3.1 The author in collaboration with J. Kornfield and L. Jenson developed techniques described by Hasler et al. (1968) which are included in this proposal as an appendix. The techniques were as follows:

a. A technique for making a two- or three-frame time-lapse movie using a "Blink" projection system.

b. A technique for making precision measurements from the "Blink" images using an electronic digitizing table.

c. A technique for correcting the pictures for distortion.

1. An ellipse was fitted to points on the earth's limb with the aid of the UWCC's GAUSHAUS subroutine.

2. The earth was then restored to a circle, correcting for any linear distortion in the picture. The pictures were also scaled to correct for any size variability by measuring the apparent earth diameter in each picture.

d. A technique for computer superimposition of two or more pictures.

1. The center of each circle was transposed to the origin of measuring table.

2. The pictures were then rotated until the landmarks coincided.

e. A technique for rectification of the pictures.

1. The pictures were regarded as those made by a conventional camera so that a tangent plane approximation could be used.

2. Distances between any two points on one or more pictures were calculated by spherical geometry.

f. Techniques for the direction of a vector and its latitude and longitude.

1. The direction of a cloud displacement vector was estimated roughly from a gridded diagram of the vector field.

2. A rough estimate was made from a grid to determine latitude and longitude.

3.2 The following improvements and changes were made in the techniques:

a. An improved ellipse-fitting technique was devised.

1. The advantages of the new technique are:

a. improved accuracy
b. elimination of preliminary estimation of parameters
c. a great saving of computer time.

2. The mathematical basis for this nonlinear least-squares regression is presented in section 4.2.

b. Equations for accurate navigation of the pictures were derived and programmed.

1. These equations effect the transformation of a point on the picture with coordinates X_i, Y_i into latitude and longitude on the earth's surface.

2. The equations are presented in section 4.3.

c. A simple approximation was developed to determine the direction of the cloud displacement vectors (see section 4.4).

d. A "close-up" time-lapse movie projection technique was substituted for the "Blink" projection system described in the appendix.

1. Reasons for the substitution:

(a) The "Blink system was unavailable for more than a few test cases.

(b) The development of a precision alignment system made the use of movies more attractive.

(c) The use of "close-ups" enables one to preserve the full resolution of the original picture over a small area.

(d) The use of "close-ups" eliminates the camera and projector registration as a major source of error.

(e) The availability of Hughes and University of Wisconsin precision display pictures makes individual distortion correction of each picture unnecessary.

2. Advantages of the movie technique:

(a) The maximum time resolution of the data can be maintained over a longer period.

(b) Better time resolution allows one to use every possible cloud which is a suitable tracer.

(c) An ordinary 16 mm. projector can be used.

e. Description of the "close-up" time lapse movie measuring technique.

1. A "close-up" time-lapse movie is produced.

(a) The original negatives are aligned by a technique described by Hasler and Kornfield (1968) or using the precision alignment system.

(b) Bellows extensions of "close-up" lenses are used to reduce the area covered in the film.

(c) A film loop is made with the following sequence "endlessly" repeated: nine frames of the first and last negatives and three frames of the intermediate negatives.

(d) A film covering the nine negatives taken during the three middle hours of the day is considered ideal.

2. The "close-up" film loop is projected onto a piece of cardboard. Measurements are made by plotting the information accurately on the cardboard.

3. Four clouds or landmarks are measured on the "close-up" of the local noon picture.

4. The cloud trajectories are measured from the "close-up" film loop. Section 3.3 of the appendix describes the cloud selection and measurement procedure.

5. The following points are measured on the full earth picture taken at local noon.

   (a) The same four clouds or landmarks measured in the "close-up" picture.

   (b) One or more reference landmarks whose latitude and longitude are known.

   (c) About 100 points on the earth's limb.

6. The plotted reference points and cloud trajectory plots are then taken to an electronic digitizing table and the X and Y coordinates are accurately measured.

7. Preliminary estimates of the accuracy.

   (a) The repeatability of measuring the same cloud is 3 nm. (See Section 3.2 of the Appendix.)

   (b) Navigation error is about 10 nm.

   (c) Alignment error is about 10 nm. as determined by measuring the apparent velocity of landmarks.

   (d) The individual errors are not generally additive. In fact, both the alignment and navigation errors can be subtracted out in the area near a landmark. Also the divergence and vorticity measuring techniques are nearly independent of the navigation error, and the divergence technique is completely independent of alignment error. The total error in determination of a

velocity vector is about ± 10 nm. and may possibly be improved. Since this is a 10-nm. error taken over a three-hour period the total error in speed is about three knots. The Direction error is about ± 1.5 degrees.

f. A simple "close-up" transformation was devised to relate measurements made on the "close-up" pictures to the geometry of the full earth pictures (see Section 4.5).

3.3 A computer program was written by the author which takes the raw data output of the electronic digitizing table and performs all the necessary operations described above. It prints out the following information about the velocity field:

a. Latitude and longitude of a cloud at time T_1 and T_2.

b. Distance traveled on the surface of the earth.

c. Speed of travel.

d. Direction of travel.

e. U and V components of the velocity vector.

3.4 Divergence Measuring Technique

a. Description of the technique

1. A ring of clouds (or velocity vectors) is selected which form a polygon which has an approximately circular shape and which is of the scale size desired.

2. The area of the polygon is computed at times T_1 and T_2 and the change in area gives the divergence according to the system of equations derived in Section 4.6.

b. Reasons for using the technique

1. The technique was developed because it is independent of alignment errors.

(a) Conventional techniques would use the velocity vectors directly which contain the alignment errors.

(b) This technique is dependent only on the accuracy with which the distance between clouds on the same picture can be measured and how well the clouds serve as tracers.

2. The technique is purely objective and does not depend on subjective streamline or isotach analysis.

3. The technique can be used to calculate divergence directly from a vector field with nonuniform spacing.

c. Error analysis

1. Assumptions:

(a) The area over which the technique is applied must not diverge too far from a plane. (However since the area is computed twice in almost exactly the same spot on the earth, the error will tend to cancel out.)

(b) In the limit where the polygon is a triangle, the technique is identical with the technique described by Bellamy (1949) which assumes linear variation of velocity.

(c) If five or more clouds are used and the polygon is nearly circular, the technique may give unbiased results for second-order variations in velocity. In fact, it may approach the accuracy of the more sophisticated models derived by P. Schmidt and D. Johnson. [1]

2. Preliminary error estimates
(If one assumes that the wind vector is known within $\pm$ 3 knots then the error in divergence is about $\pm .2 \times 10^{-5}$ sec^{-1} over a 500 km. $\times$ 500 km. for a polygon with only 3 vertices.)

3.5 Vorticity Measuring Technique

a. The logical extension of the divergence measuring technique was to approximate the line integral $\oint \frac{\vec{V} \cdot \vec{ds}}{A}$ around the same polygon, thereby measuring the vorticity. The equations for this technique are presented in Section 4.7.

b. The technique therefore uses the identical data input as the convergence technique and makes the results directly comparable.

---

[1] Schmidt, P., and D. Johnson: Vertical Profiles of Polynomial Filtered Winds, Divergence and Vertical Motion. (Unpublished paper)

c. The assumptions for the technique are nearly identical to those of the divergence technique. However in this case the picture alignment error cannot be eliminated, but since any rotation error will be systematic over the entire picture the measurement of vorticity in one part of the picture relative to another part should be independent of the alignment error.

4. MATHEMATICAL BASIS OF THE TECHNIQUES

Most of the equations and mathematical operations used in the techniques explained in Section 3 are outlined in this section. Some derivations are also included.

4.1 Refer to Hasler et al. (1968) which is included as an appendix for the following equations and derivations.

a. Tangent plane approximation used in rectifying the pictures (pages A1-A3).

b. Mathematical basis of the original distortion correction and superimposition procedure (pages A3 - A5).

c. Equations for the rectification procedure (pages A6 - A10).

4.2 Nonlinear least-squares regression for a completely arbitrary(five-parameter) ellipse. This regression is used to determine the subsatellite point for the navigation of the pictures and to correct any linear distortion in the picture. Let

$$A'X_i^2 + B'Y_i^2 + C'X_iY_i + D'X_i + E'Y_i + F' = 0$$

be the most general equation for a planor ellipse where $A', B', \ldots, F'$ are the coefficients and X_i, Y_i are the coordinates of the i^{th} point on the ellipse, then we can get:

$$AX_i^2 + BY_i^2 + CX_iY_i + DX_i + EY_i = 1$$

If we assume that the relationship between X and Y is not perfect, we can represent the error as ε_i for the i^{th} point so that

$$AX_i^2 + BY_i^2 + CX_iY_i + DX_i + EY_i - 1 + \varepsilon_i = 0$$

Let

$$AX_i^2 + BY_i^2 + CX_iY_i + DX_i + EY_i - 1 = W_i .$$

The least square estimators of $A, B, \ldots, E$ may be obtained by minimizing the quantity

$$Z = \Sigma(\varepsilon_i)^2 = \Sigma(W_i)^2$$

with respect to $A, B, \ldots, E$ (all sums are from $i = 1$ to $i = N$ where N is the number of data points). This can be done in the following manner.

Let

$$\frac{\partial Z}{\partial A} = 2\Sigma X_i^2 W_i = 0$$

$$\frac{\partial Z}{\partial B} = 2\Sigma Y_i^2 W_i = 0$$

$$\frac{\partial Z}{\partial C} = 2\Sigma X_i Y_i W_i = 0$$

$$\frac{\partial Z}{\partial D} = 2\Sigma X_i W_i = 0$$

$$\frac{\partial Z}{\partial E} = 2\Sigma Y_i W_i = 0$$

where the values of $A, B, \ldots, E$ at the minimum are their estimators $\hat{A}, \hat{B}, \ldots, \hat{E}$.

We now have 5 equations and 5 unknowns:

$$\hat{A}\Sigma X_i^4 + \hat{B}\Sigma X_i^2 Y_i^2 + \hat{C}\Sigma X_i^3 Y_i + \hat{D}\Sigma X_i^3 + \hat{E}\Sigma X_i^2 Y_i = \Sigma X_i^2$$

$$\hat{A}\Sigma X_i^2 Y_i^2 + \hat{B}\Sigma Y_i^4 + \hat{C}\Sigma X_i Y_i^3 + \hat{D}\Sigma X_i Y_i^2 + \hat{E}\Sigma Y_i^3 = \Sigma Y_i^2$$

$$\hat{A}\Sigma X_i^3 Y_i + \hat{B}\Sigma X_i Y_i^3 + \hat{C}\Sigma X_i^2 Y_i^2 + \hat{D}\Sigma X_i^2 Y_i + \hat{E}\Sigma X_i Y_i^2 = \Sigma X_i Y_i$$

$$\hat{A}\Sigma X_i^3 + \hat{B}\Sigma X_i Y_i^2 + \hat{C}\Sigma X_i^2 Y_i + \hat{D}\Sigma X_i^2 + \hat{E}\Sigma X_i Y_i = \Sigma X_i$$

$$\hat{A}\Sigma X_i^2 Y_i + \hat{B}\Sigma Y_i^3 + \hat{C}\Sigma X_i Y_i^2 + \hat{D}\Sigma X_i Y_i + \hat{E}Y_i^2 = \Sigma Y_i$$

which is $\bar{T} \cdot \bar{X} = \bar{V}$ in matrix notation, where

$$\bar{T} = \begin{vmatrix} \Sigma X_i^4 & \Sigma X_i^2 Y_i^2 & \Sigma X_i^3 Y_i & \Sigma X_i^3 & \Sigma X_i^2 Y_i \\ \Sigma X_i^2 Y_i^2 & \Sigma Y_i^4 & \Sigma X_i Y_i^3 & \Sigma X_i Y_i^2 & \Sigma Y_i^3 \\ \Sigma X_i^3 Y_i & \Sigma X_i Y_i^3 & \Sigma X_i^2 Y_i^2 & \Sigma X_i^2 Y_i & \Sigma X_i Y_i^2 \\ \Sigma X_i^3 & \Sigma X_i Y_i^2 & \Sigma X_i^2 Y_{i.} & \Sigma X_i^2 & \Sigma X_i Y_i \\ \Sigma X_i^2 Y_i & \Sigma Y_i^3 & \Sigma X_i Y_i^2 & \Sigma X_i Y_i & \Sigma Y_i^2 \end{vmatrix} \quad \bar{X} = \begin{vmatrix} \hat{A} \\ \hat{B} \\ \hat{C} \\ \hat{D} \\ \hat{E} \end{vmatrix}$$

$$\bar{V} = \begin{vmatrix} \Sigma X_i^2 \\ \Sigma Y_i^2 \\ \Sigma X_i Y_i \\ \Sigma X_i \\ \Sigma Y_i \end{vmatrix}$$

which may be solved for $\bar{X}$ by inverting the $\bar{T}$ matrix

$$\bar{X} = \bar{T}^{-1}\bar{V}$$

This can be done easily by a computer library subroutine and gives the estimators

$$\hat{A},\ \hat{B},\ \hat{C},\ \hat{D},\ \hat{E}$$

These are related to the coefficients used on page A-3 of the Appendix by

$$T_1 = \frac{\hat{B}}{\hat{A}} \quad T_2 = \frac{\hat{C}}{\hat{A}} \quad T_3 = \frac{\hat{D}}{\hat{A}} \quad T_4 = \frac{\hat{E}}{\hat{A}} \quad T_5 = \frac{1}{\hat{A}}$$

An estimate of the rotation, major and minor axis, and x and y coordinates of the center of the ellipse may be obtained from these coefficients as explained in pages A3 - A5 of the Appendix.

4.3 Latitude-Longitude Equations

Given the following:

1. The X and Y coordinates (X_{ssp}, Y_{ssp}) of the subsatellite point on the picture as derived above in 4.2 and in the Appendix (pages A3 - A5).

2. The latitude and longitude $(\alpha_{ssp}, \gamma_{ssp})$ of the subsatellite point (part of orbital data supplied by NASA).

3. The X and Y coordinates (X_{lm}, Y_{lm}) of a landmark as measured directly from the picture.

4. The latitude and longitude $(\alpha_{lm}, \gamma_{lm})$ of the landmark as determined from an atlas.

5. The great circle distance between two points on the surface of the earth as a function of their X and Y coordinates on the picture as derived in the Appendix (pages A6 - A10).

6. The X and Y coordinates (X_C, Y_C) of a point C on the picture as measured directly.

Find the latitude and longitude $(\Delta\alpha_C, \Delta\gamma_C)$ of point C.

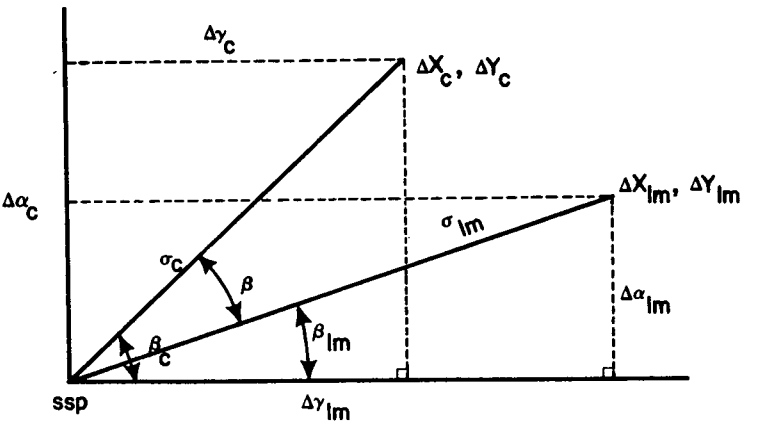

$$\Delta\alpha_{lm} = \alpha_{ssp} - \alpha_{lm}$$

$$\Delta\gamma_{lm} = \gamma_{ssp} - \gamma_{lm}$$

$$\Delta X_{lm} = X_{ssp} - X_{lm}$$

$$\Delta Y_{lm} = Y_{ssp} - Y_{lm}$$

$$\Delta X_c = X_{ssp} - X_c$$

$$\Delta Y_c = Y_{ssp} - Y_c$$

$$\left.\begin{aligned} \sigma_{lm} &= f(\Delta X_{lm}, \Delta Y_{lm}) \\ \sigma &= f(\Delta X_c, \Delta Y_c) \\ \beta &= f(\Delta X_{lm}, \Delta Y_{lm}, \Delta X_c, \Delta Y_c) \end{aligned}\right\} \text{ as derived in the Appendix (pages A6 - A10)}$$

From the law of sines for a spherical triangle

$$\beta_{lm} = \arcsin\left(\frac{\sin\Delta\alpha_{lm}}{\sin\sigma_{lm}}\right)$$

$$\beta_c = \beta + \beta_{lm}$$

If $(X_{lm}Y_c - Y_{lm}X_c) < 0$ multiply β by -1.

Then again from the law of sines

$$\Delta\alpha_c = \arcsin[\sin\beta_c \sin\sigma_c]$$

and from Napier's law for right spherical triangles

$$\Delta\gamma_c = \arcsin[\tan\Delta\gamma_c \tan(90° - \beta_c)].$$

4.4 Direction Equations

Given the latitude and longitude of two points $(\alpha_1, \gamma_2, \alpha_2, \gamma_2)$ on the earth's surface less than 200 km. apart find the approximate direction (θ) of the great circle arc connecting them.

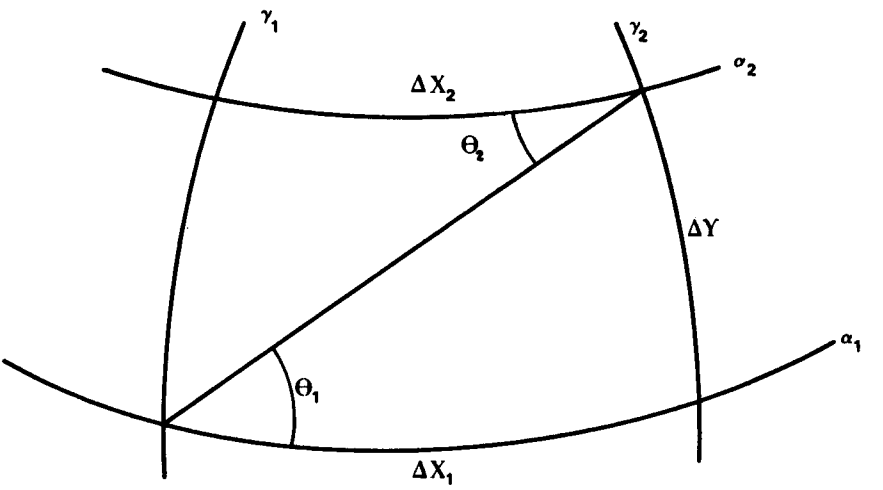

The average X displacement is

$$\overline{\Delta X} = (\gamma_1 - \gamma_2) \cos \frac{(\alpha_1 + \alpha_2)}{2}$$

The Y displacement is

$$\Delta Y = \alpha_2 - \alpha_1 .$$

Then the approximate direction is

$$\bar{\theta} = \arctan \frac{\Delta Y}{\overline{\Delta X}} .$$

If $\overline{\Delta X}$ and ΔY are divided by the time interval between pictures, we have the u and v components of the motion.

4.5 "Close-Up" Transformation Equations

Given: 1) Four reference points on a "close-up" picture (XR_i^{cu}, YR_i^{cu}).

2) The same four reference points measured on a full-earth picture (XR_i^{FE}, YR_i^{FE}).

3) An arbitrary point measured on the "close-up" picture (X_i^{cu}, Y_i^{cu}).

Find: The necessary transformation equations to find the corresponding point on the full-earth picture (X_i^{FE}, Y_i^{FE}).

The line connecting two reference points, on the full-earth picture, makes the angle θ_{FE} with the measuring table coordinate system where

$$\theta_{FE} = \arctan\left[\frac{XR_2^{FE} - XR_1^{FE}}{YR_2^{FE} - YR_1^{FE}}\right]$$

The corresponding angle on the "close-up" picture is

$$\theta_{cu} = \arctan\left[\frac{XR_2^{cu} - XR_1^{cu}}{YR_2^{cu} - YR_1^{cu}}\right]$$

therefore one picture must be rotated through an angle θ in order to bring it into alignment, where

$$\theta = \theta_{cu} - \theta_{FE}$$

this can be accomplished by rotating each point on the "close-up" picture including the four reference points by using the following expressions:

$$X\theta_i^{cu} = X_i^{cu} \cos\theta + Y_i^{cu} \sin\theta$$

$$Y\theta_i^{cu} = -X_i^{cu} \sin\theta + Y_i^{cu} \cos\theta$$

$$XR\theta_i^{cu} = XR_i^{cu} \cos\theta + YR_i^{cu} \sin\theta$$

$$YR\theta_i^{cu} = -XR_i^{cu} \sin\theta + YR_i^{cu} \cos\theta .$$

The final step in the transformation is the sizing operation which is accomplished by the following interpolation equations:

$$X_i^{FE} = (X\theta_i^{cu} - XR\theta_3^{cu}) \frac{(XR_4^{FE} - XR_3^{FE})}{(XR\theta_4^{cu} - XR\theta_3^{cu})} + XR_3^{FE}$$

$$Y_i^{FE} = (Y\theta_i^{cu} - YR\theta_1^{cu}) \frac{(YR_2^{FE} - YR_1^{FE})}{(YR\theta_2^{cu} - YR\theta_1^{cu})} + YR_1^{FE} .$$

4.6 Divergence Equations

Given: The latitude and longitude of n clouds forming an irregular n-sided polygon at times T_1 and T_2 $(\alpha_i^1, \gamma_i^1, \alpha_i^2, \gamma_i^2)$ as shown in Figure 1.

Find: Divergence (horizontal)

Let divergence be defined as $D_2V = \dfrac{\Delta A_n}{A_n \Delta T}$ where A_n is the area of the polygon and ΔA_n is the change in area over the time interval $\Delta T = T_2 - T_1$.

We can write an expression for the area of a polygon which is based on summing triangular-shaped subareas.

$$A_n = \sum_{i=1}^{n} \frac{Y_i(X_{i+1} - X_{i-1})}{2}$$

which is good for a rectangular coordinate system where X_i, Y_i are the coordinates of the vertices.

Now we can apply this expression to a spherical earth coordinate system. A good approximation for moderate-sized areas can be made by multiplying the longitude differences between two points by the cosine of the average latitude of the two points.

Let the average latitude of clouds $i + 1$ and $i - 1$ at time T_1 be

$$\bar{\alpha}_i^1 = \frac{\alpha^1_{i+1} + \alpha^1_{i-1}}{2}$$

and at time T_2

$$\bar{\alpha}_i^2 = \frac{\alpha^2_{i+1} + \alpha^2_{i-1}}{2} .$$

Then the area of the polygon at time T_1 is

$$A_1 = \frac{\sum_{i=1}^{n} \alpha_i^1(\gamma^1_{i+1} - \gamma^1_{i-1}) \cos \bar{\alpha}_i^1}{2}$$

and at time T_2

$$A_2 = \frac{\sum_{i=1}^{n} \alpha_i^2(\gamma^2_{i+1} - \gamma^2_{i-1}) \cos \bar{\alpha}_i^2}{2}$$

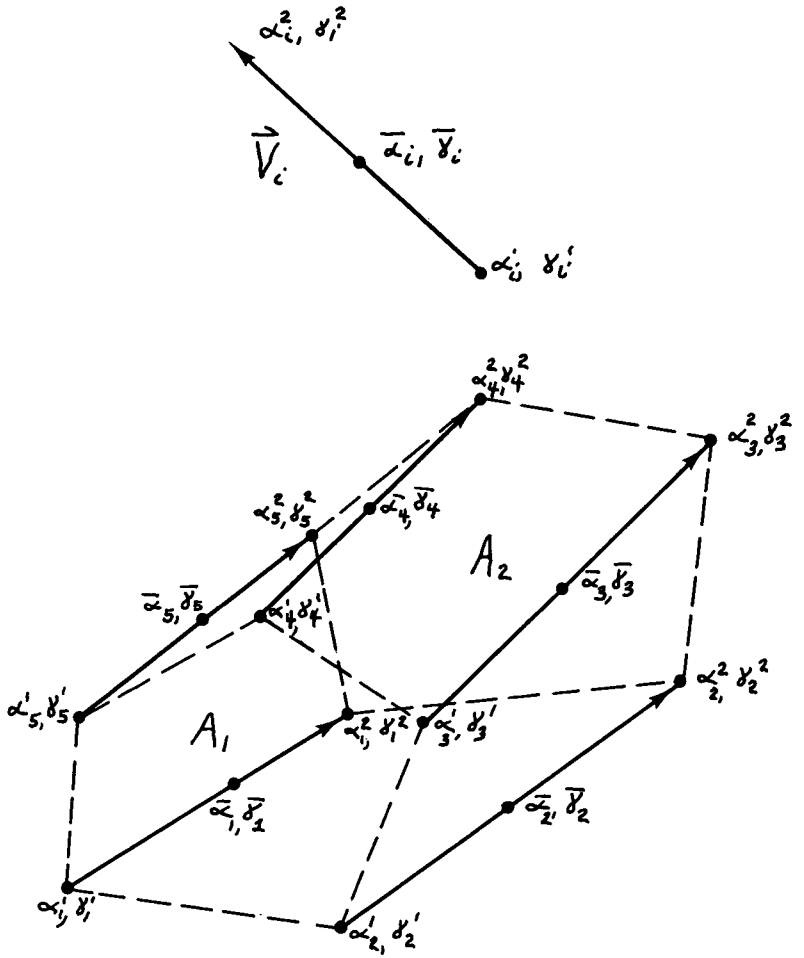

Fig. 1. Above: Cloud displacement vector $\vec{V}_i$, where the start point of the vector is at latitude and longitude (α_i^1, γ_i^1) of the cloud at time T_1. The end point is at latitude and longitude (α_i^2, γ_i^2) at time T_2. The midpoint of the vector is at average latitude and longitude $\bar{\alpha}_i$, $\bar{\gamma}_i$.

Below: A 5-sided polygon with area A_1 at time T_1 and area A_2 at time T_2.

The divergence is then

$$D_2V = \frac{A_2 - A_1}{|A_1|(T_2 - T_1)} \quad .$$

4.7 Vorticity Equations

Given: The latitude and longitude of n clouds forming an irregular n-sided polygon at times T_1 and T_2 as shown in Figure 2.

Find: Vorticity (vertical component of relative vorticity).

Let vorticity be defined as $\zeta \cdot \oint \frac{\vec{V} \cdot \vec{ds}}{A_n}$ where $\vec{V}$ is the horizontal wind vector at the location of elemental segment $\vec{ds}$ which is on the line surrounding the area A_n. The symbol $\oint$ indicates the line integral taken around the area. Now if we write this in finite difference form

$$\zeta = \sum_{i=1}^{n} \frac{|\vec{V}_i||\Delta\vec{S}_i| \cos\theta_i}{A_n}$$

$|\vec{V}_i|$ then represents the average speed of the wind blowing across the line segment $\Delta\vec{S}_i$ at the average angle θ_i.

Let $\vec{V1}_i$ and $\vec{V2}_i$ be the wind vectors at each end of $\Delta\vec{S}_i$ and let $\theta 1_i$ and $\theta 2_i$ be the respective angles between the wind vectors and $\Delta\vec{S}_i$. Then $|\vec{V}_i| = \frac{|\vec{V1}_i| + |\vec{V2}_i|}{2}$ and $\theta_i = \frac{\theta 1_i + \theta_2}{2}$ and we can write the vorticity in this form

$$\zeta = \frac{\sum_{i=1}^{n} \frac{|\vec{V1}_i| + |\vec{V2}_i|}{2} |\Delta\vec{S}_i| \cos\frac{\theta 1_i + \theta 2_i}{2}}{A_n}$$

If we use the average dot product instead we get

$$\zeta = \frac{\sum_{i=1}^{n} |\vec{V1}_i| \cos\theta 1_i + |\vec{V2}_i| \cos\theta 2_i \, |\Delta\vec{S}_i|}{A_n}$$

these two expressions are not equivalent but give equally valid approximations to the line integral. The second expression has been used in this thesis.

3

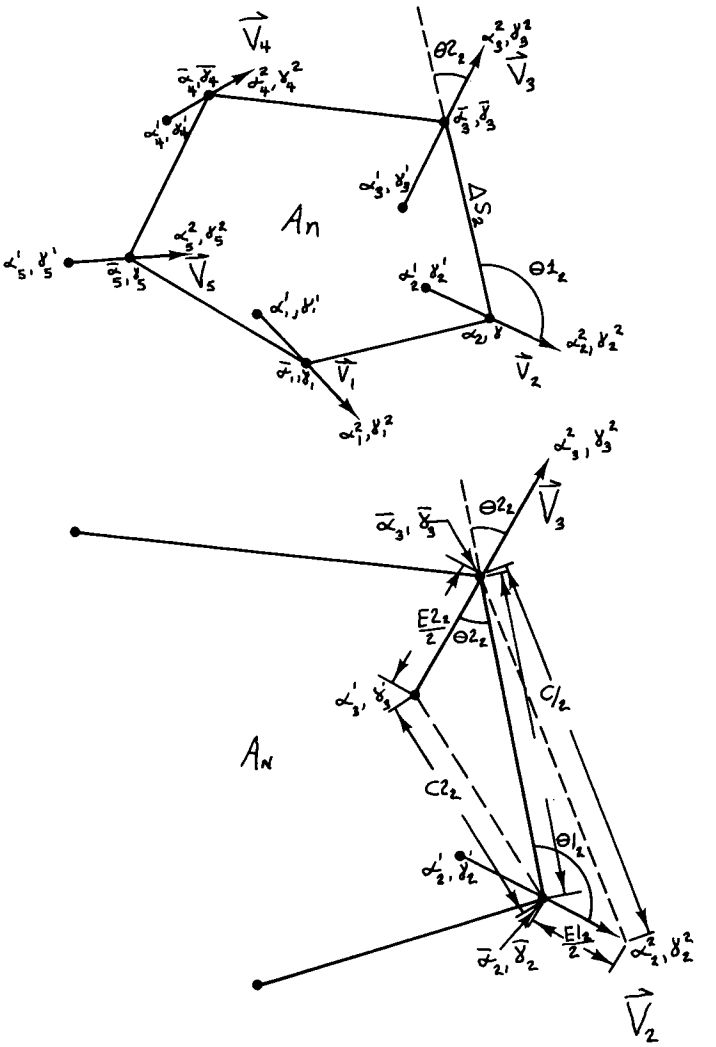

Fig. 2. Above: A 5-sided polygon described by the midpoints of the vectors with area A_n.

Below: Diagram of the geometry used in the vorticity measuring technique. The quantities A_i, $E1_i/2$, $E2_i/2$, $C1_i$, $C2_i$, $\theta 1_i$, $\theta 2_i$ are diagrammed for a specific case.

Let the latitude and longitude of the midpoint of the line connecting the cloud at time T_1 and time T_2 be

$$\bar{\alpha}_i = \frac{\alpha_i^1 + \alpha_i^2}{2}$$

$$\bar{\gamma}_i = \frac{\gamma_i^1 + \gamma_i^2}{2}$$

Again if we multiply the longitude differences between two points by the cosine of the average latitude of the two points we have an approximate expression for a spherical coordinate system. We therefore define six average latitude functions

$$\bar{\alpha}1_i = \frac{\bar{\alpha}_{i+1} + \bar{\alpha}_i}{2}$$

$$\bar{\alpha}2_i = \frac{\bar{\alpha}_{i+1} + \alpha_i^2}{2}$$

$$\bar{\alpha}3_i = \frac{\bar{\alpha}_i + \alpha^1_{i+1}}{2}$$

$$\bar{\alpha}4_i = \frac{\alpha_i^1 + \alpha_i^2}{2}$$

$$\bar{\alpha}5_i = \frac{\alpha^1_{i+1} + \alpha^2_{i+1}}{2}$$

$$\bar{\alpha}6_i = \frac{\bar{\alpha}_{i+1} + \bar{\alpha}_{i-1}}{2}$$

and the following coefficients

$$A_i = \sqrt{[(\bar{\gamma}_{i+1} - \bar{\gamma}_i)\cos\bar{\alpha}1_i]^2 + [\bar{\alpha}_{i+1} - \bar{\alpha}_i]^2}$$

$$C1_i = \sqrt{[(\bar{\gamma}_{i+1} - \gamma_i^2)\cos\bar{\alpha}2_i]^2 + [\bar{\alpha}_{i+1} - \alpha_i^2]^2}$$

$$C2_i = \sqrt{[(\bar{\gamma}_i - \gamma^2_{i+1})\cos\bar{\alpha}3_i]^2 + [\bar{\alpha}_i^1 - \alpha_{i+1}]^2}$$

$$E1_i = \sqrt{[(\gamma_i^1 - \gamma_i^2)\cos\bar{\alpha}4_i]^2 + [\alpha_i^1 - \alpha_i^2]^2}$$

$$E2_i = \sqrt{[(\gamma^1_{i+1} - \gamma^2_{i+1}) \cos \bar{\alpha}5_i]^2 + [\alpha^1_{i+1} - \alpha^2_{i+1}]^2}$$

$$F_i = \bar{\alpha}_i(\bar{\gamma}_{i+1} - \bar{\gamma}_{i-1}) \cos \bar{\alpha}6_i$$

then

$$V1_i = E1_i/\Delta T$$

$$V2_i = E_{2i}/\Delta T$$

$$\cos \theta 1_i = \frac{(E1_i/2)^2 + (A_i)^2 - (C1_i)^2}{A_i \cdot E1_i}$$

$$\cos \theta 2_i = \frac{(E2_i/2)^2 + (A_i)^2 - (C2_i)^2}{A_i \cdot E2_i}$$

$$\Delta s_i = A_i .$$

Then by summing we get the vorticity

$$\zeta = \sum_{i=1}^{n} \frac{(|V1_i| \cos \theta 1_i + |V2_i| \cos \theta 2_i)|\Delta S_i|/2}{\left| \sum_{i=1}^{n} F_i/2 \right|}$$

where

$$A_n = \left| \sum_{i=1}^{n} F_i/2 \right| .$$

5. PRELIMINARY RESULTS

The divergence and vorticity measuring techniques were compared with more conventional techniques and the correspondence was found to be good. The complete set of techniques described in Sections 3 and 4 were tested on a set of real ATS-I cloud cluster pictures. The quantitative description of the wind field and its divergence and vorticity was reasonable and of the right order of magnitude. The location of regions of convergence and positions relative vorticity coincided very well with the location of a large active cloud cluster.

5.1 The divergence and vorticity measuring techniques were first compared with measurements made by conventional techniques.

a. A uniformly spaced vector field was derived from satellite-determined cloud trajectories. The divergence and vorticity was then calculated using the equations $D_2V = \frac{\Delta U}{\Delta X} + \frac{\Delta V}{\Delta Y}$ and $\zeta = \frac{\Delta V}{\Delta X} - \frac{\Delta U}{\Delta Y}$. The divergence and vorticity was then calculated for polygons consisting of the squares made up by the uniform vector field.

b. The correspondence between the two techniques was very good. The average difference between the two divergence techniques was 9.5% with a standard deviation of 7.7%. The average difference between the two vorticity techniques was 4.2% with a standard deviation of 3.8%.

5.2 The complete procedure outlined in Section 3 was put through a full-fledged trial run.

a. Description of the test

1. A time-lapse movie showing a cloud cluster in the central Pacific was made from the ATS-I pictures taken on June 9, 1968. Figure 3 shows the full-earth picture taken at local noon with the "close-up" area outlined. The cloud cluster was growing quite rapidly during the study period and produced a large amount of cirrus outflow originating primarily from the area centered at 7°N, 157°W.

2. The velocity vectors were determined using the techniques described above. The divergence and vorticity measurements were made by selecting the largest polygon with a good shape which would fit in a 1000 nm. × 1000 nm. box. Since the data density for the first trial run was not as great as desired, these polygons had only three to five vertices.[1] A second set of larger polygons was also selected which were on the order of 1500 nm. × 1500 nm. with five to eight vertices. The large polygons were selected so that they corresponded with the various regimes found at the smaller scale size.

b. Results

1. Figure 4 shows the low-level and high-level trajectories plotted on the "close-up" picture taken at local noon. All pertinent

[1] When the low-data density was discovered the data were rerun and densities of four to sixteen were taken in this area. (These data have not been processed yet.)

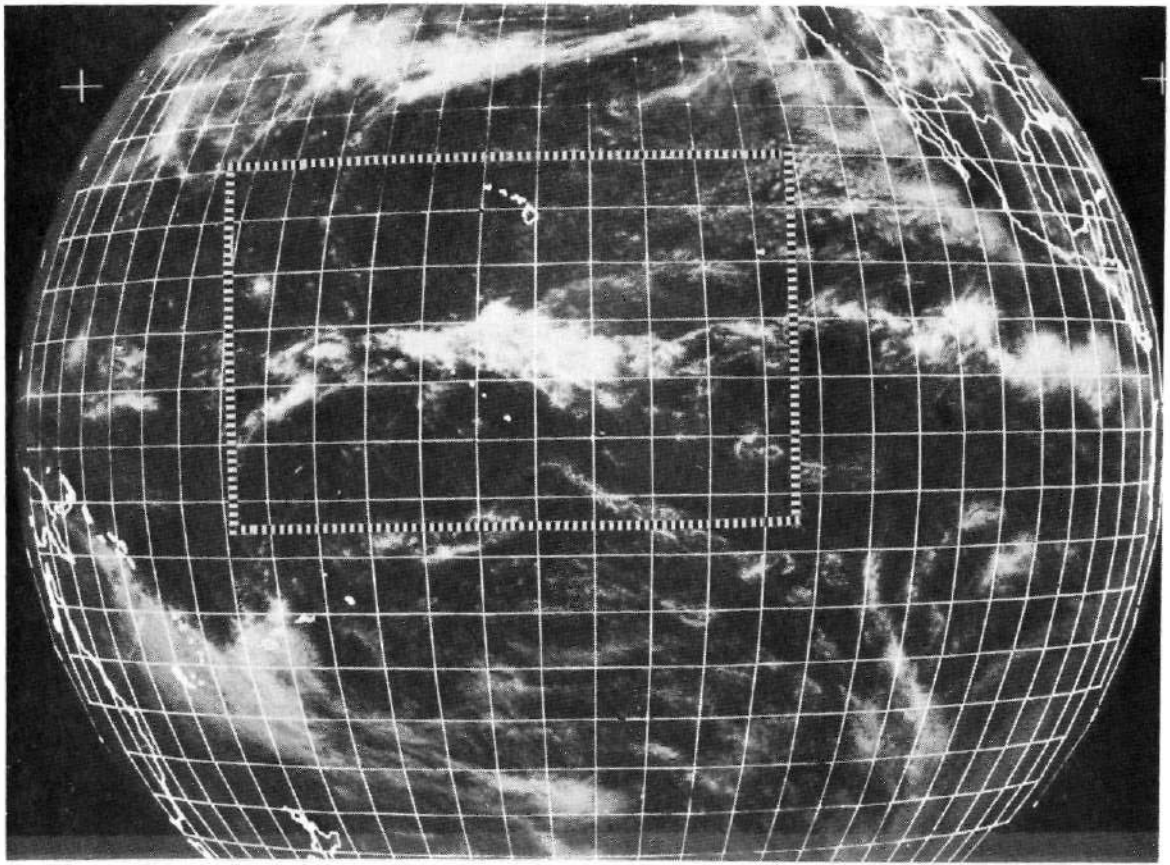

Fig. 3. ATS-I Spin Scan Camera full-earth picture taken at local noon (21 hr. 42 min. GMT) June 9, 1968 with "close-up" area outlined.

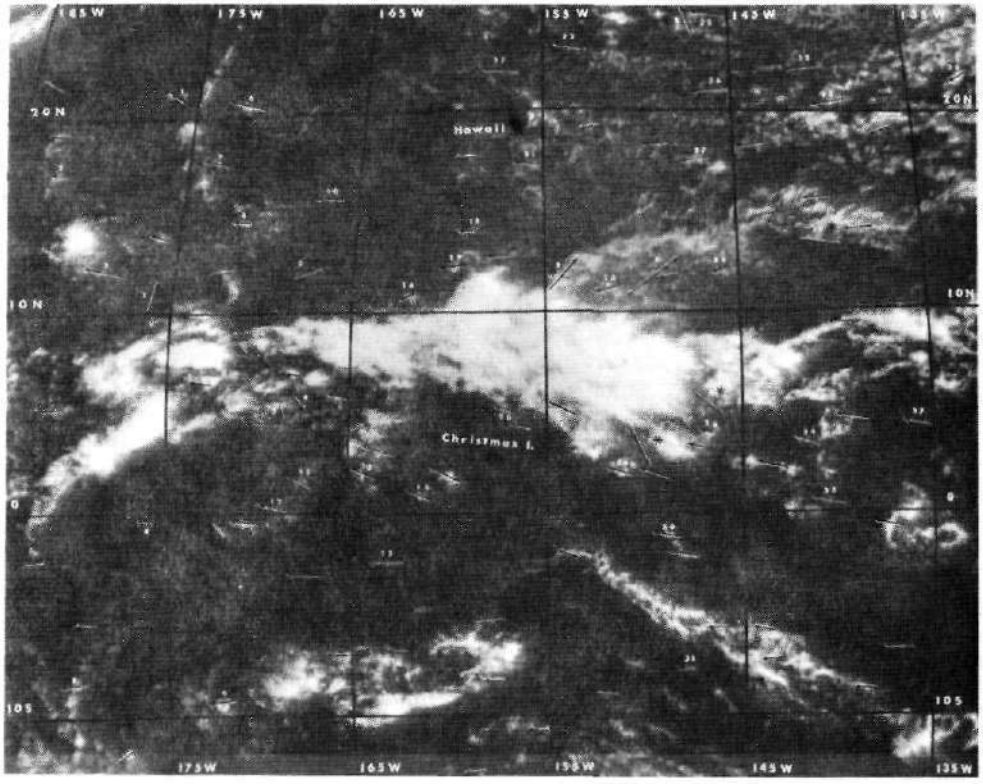

Fig. 4. "Close-up" of Fig. 3 showing the wind field around the cloud cluster. Low-level and high-level winds are plotted in accordance with Table 1. Upper-level winds are marked with asterisks. Arrows without numbers represent some of the additional low-level wind data taken on a second attempt. The coverage was much more dense, but the data have not been processed yet.

data computed from those trajectories are presented in Table 1.

2. The results of the divergence and vorticity measurements for the smaller scale polygons are shown in Figure 5. The correspondence between the regions of convergence and position relative vorticity and the region occupied by the cloud cluster is good. The convergence and vorticity values are of the right order of magnitude, but are somewhat smaller than the results of Fujita et al. (1969).

3. The results of the large-scale measurements of convergence and vorticity (see Fig. 6) show a good correspondence between the large- and small-scale sizes.

TABLE I

Low-Level and Upper-Level Wind Vector Field
(Output of Computer Program Described in Section 4.3. Note: Upper-Level Clouds are Starred.)

Cloud Number	Location at Time T_1 20 hr 31 min GMT Latitude (+ north)	Longitude (+ west)	Location at Time T 23 hr 40 min GMT Latitude (+ north)	Longitude (+ west)	Distance traveled (nm)	Speed (Knots)	U Comp. of Velocity (Knots)	V Comp. of Velocity (Knots)	Direction of Velocity Vector (Degrees)
1	21.54	176.17	21.85	176.58	29.4	9.3	-7.3	5.9	128.8
2	17.81	-177.42	17.82	-176.96	26.5	8.4	-8.4	.2	91.4
3	12.78	178.72	12.96	179.84	66.1	21.0	-20.7	3.3	99.1
4	-.49	-177.56	-.46	-177.02	32.8	10.4	-10.4	.6	93.3
5	-7.73	-179.42	-7.85	-178.67	45.5	14.4	-14.2	-2.4	80.5
6	20.58	171.44	20.99	172.42	60.1	19.1	-17.4	7.8	114.0
7	18.00	172.71	18.17	173.49	46.5	14.5	-14.1	3.1	102.5
8	13.28	170.46	13.29	171.11	38.2	12.1	-12.1	.3	91.4
9	-7.98	171.92	-8.10	172.85	55.7	17.7	-17.5	-2.2	82.8
10	15.95	166.05	16.00	166.89	48.5	15.4	-15.4	.8	93.0
11	2.37	167.52	2.71	168.16	43.4	13.8	-12.2	6.5	118.1
12	.60	168.71	.86	169.53	51.6	16.4	-15.6	5.1	108.2
13	2.77	163.78	3.09	164.48	46.1	14.6	-13.3	6.1	114.6
14	11.16	161.82	10.87	162.31	33.5	10.6	-9.1	-5.4	59.4
15	-1.60	162.65	-1.56	163.80	68.7	21.8	-21.8	.6	91.6
16	1.53	161.30	1.92	161.97	46.8	14.9	-12.8	7.5	120.5
17	22.27	157.27	22.36	158.27	55.7	17.7	-17.6	1.8	95.8
18	14.45	158.56	14.34	159.38	48.3	15.3	-15.2	-2.2	81.9
19	12.56	159.56	12.43	160.26	41.7	13.2	-13.0	-2.2	79.2
20	5.52	157.08	5.80	157.61	35.9	11.4	-10.1	5.3	117.9
21	17.38	155.66	17.42	156.35	39.3	12.5	-12.4	.9	94.0
22	23.41	153.68	23.56	156.64	53.7	17.1	-16.8	2.9	99.9
23	11.52	151.61	11.29	152.42	49.5	15.7	-15.1	-4.2	74.3
24	2.68	150.59	2.93	151.26	42.5	13.5	-12.6	4.8	110.8
25	23.84	144.83	23.98	145.50	55.1	18.8	-18.6	2.8	98.5
26	21.18	145.75	21.11	146.86	62.4	19.8	-19.8	-1.5	85.7
27	17.98	147.05	17.91	147.79	42.5	13.5	-13.4	-1.3	84.5
28	12.03	146.31	11.87	146.81	30.7	9.8	-9.3	-2.9	72.6
29	4.11	146.94	4.26	147.56	38.1	12.1	-11.8	2.8	103.5
30	-1.51	148.23	-1.42	148.93	42.2	13.4	-13.3	1.8	97.8
31	-7.84	146.71	-7.88	147.18	27.8	8.8	-8.8	-.7	85.4
32	22.52	139.99	22.17	141.09	64.1	20.4	-19.3	-6.6	71.2
33	20.60	139.47	20.30	140.45	57.6	18.3	-17.4	-5.6	72.1
34	3.81	141.74	3.55	142.43	42.4	13.5	-13.2	2.5	100.9
35	.89	140.70	1.04	141.65	57.7	18.3	-18.1	3.0	99.4
36	22.31	132.99	21.14	133.34	22.0	7.0	-6.2	-3.2	62.6
37	3.18	135.12	3.33	135.88	46.8	14.9	-14.6	2.9	101.2
1*	10.21	176.06	10.80	175.69	41.3	13.1	6.9	11.1	211.9
2*	12.12	167.11	12.30	166.42	42.0	13.3	12.8	3.5	254.6
3*	5.09	166.87	4.81	166.67	21.0	6.7	3.9	-5.4	324.3
4*	5.11	166.04	4.88	165.71	23.7	7.5	6.2	-4.2	304.1
5*	11.43	155.12	12.36	154.11	81.6	25.9	18.5	17.7	226.9
6*	10.87	150.93	11.80	149.18	117.6	37.3	32.8	17.8	241.5
7*	5.21	150.76	4.23	150.16	68.7	21.8	11.8	-18.6	328.7
8*	23.63	145.74	24.24	146.08	41.5	13.2	-6.1	11.7	152.5
9*	5.53	147.79	4.85	146.55	84.4	26.8	23.5	-12.9	298.9
10*	11.68	140.91	11.43	139.49	84.8	26.9	26.5	-4.7	280.1

FIGURE 5 SMALL SCALE

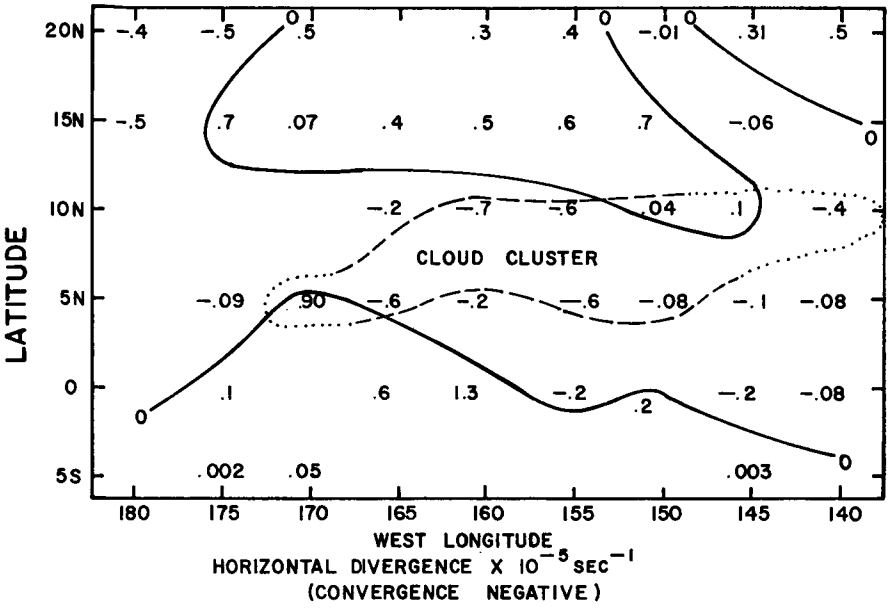

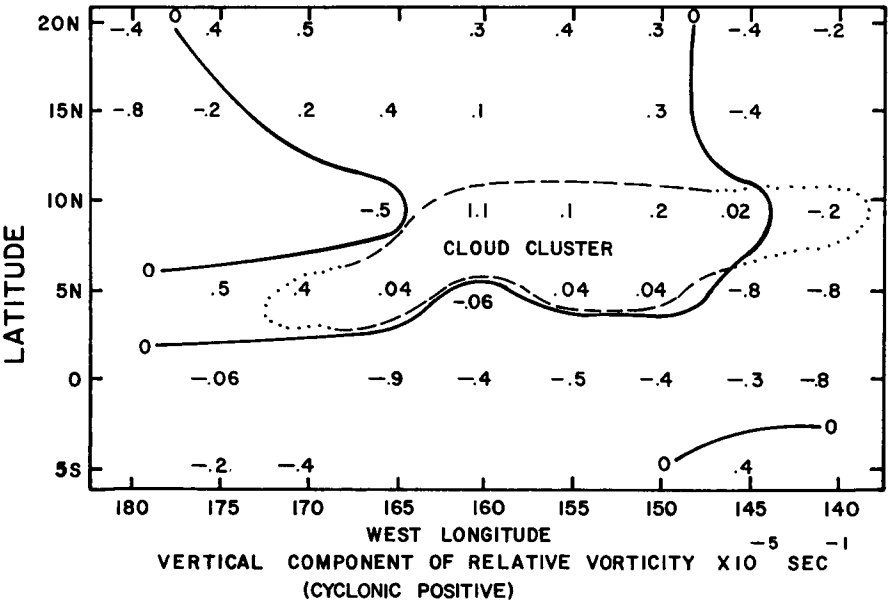

FIGURE 6 LARGE-SCALE

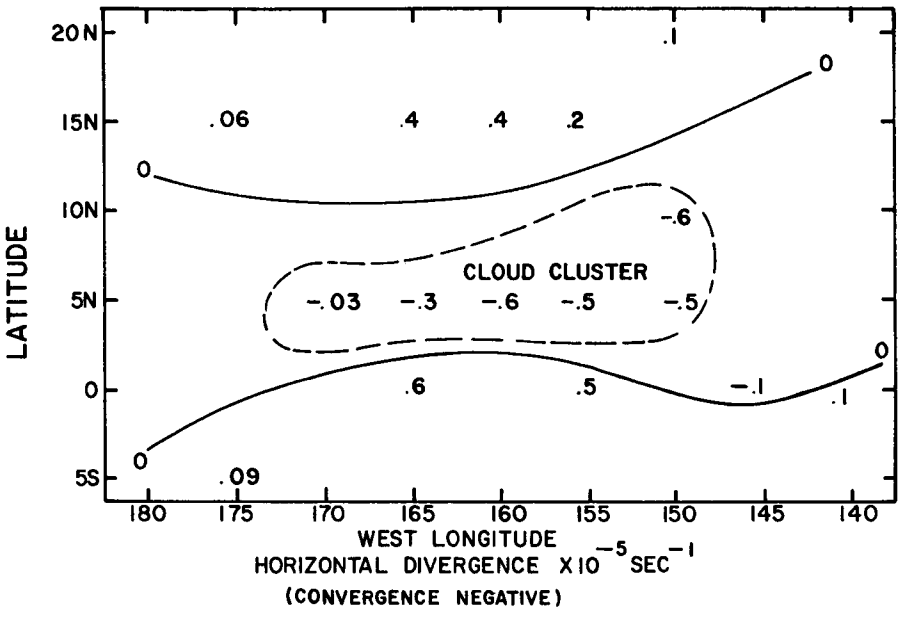

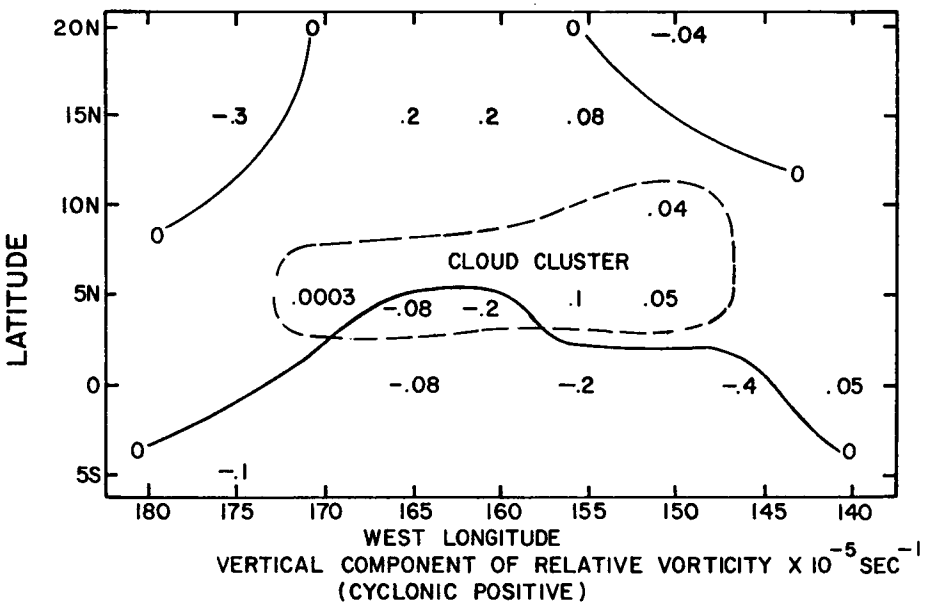

6. REFERENCES

Bellamy, J. C., 1949: Objective Calculations of Divergence, Vertical Velocity and Vorticity. Bull. of Amer. Meteor. Soc., 30, 45-49.

Fujita, T. T., K. Watanabe and T. Izawa, 1969: Formation and Structure of Equatorial Anticyclones Caused by Large-Scale Cross-Equatorial Flows Determined by ATS-I Photographs. J. Appl. Meteor., 8, 649-667.

Hasler, A. F., J. Kornfield, and L. Jensen, 1968:* A "Blink" Measuring Technique for Quantitative Measurement of Cloud Motions from ATS-I Spin Scan Camera Pictures. Weather in Motion, University of Wisconsin Press, in press.

Hasler, A. F., and J. Kornfield, 1968:* Display and Analysis of ATS-I Spin Scan Camera Pictures Through Time-Lapse Movie Techniques. Weather In Motion, University of Wisconsin Press, in press.

Joint GARP Organizing Committee, 1969: Appendix F, Report of the Study Group on Tropical Disturbances. Report of the Second Session of the Joint GARP Organizing Committee, Princeton, 27-30, January 1969.

Kornfield, J., A. F. Hasler, K. H. Hanson and V. E. Suomi, 1967: Photographic Cloud Climatology from ESSA III and V Computer-Produced Mosaics. Bull. of Amer. Meteor. Soc., 48, 878-883.

Kornfield, J., and A. F. Hasler, 1969: A Photographic Summary of the Earth's Cloud Cover for the Year 1967. J. Appl. Meteor., 8, 687-700.

National Academy of Sciences—National Research Council, 1969: Plan for U. S. Participation in the Global Atmospheric Research Program. Washington, D. C., 79 pp.

Riehl, H. and J. S. Malkus, 1958: On the Heat Balance in the Equatorial Trough Zone. Geophysica, 6, 503-538.

Schmidt, P. and D. Johnson: Vertical Profiles of Polynomial Filtered Winds, Divergence and Vertical Motion. (Unpublished paper)

Simpson, J., M. Garstang, E. J. Zipser and G. A. Deen, 1967: A Study of a Non-Deepening Tropical Disturbance. J. Appl. Meteor., 6, 237-254.

---

*Accepted for publication in 1968.

APPENDIX

A "Blink" Measuring Technique for Quantitative Measurement of Cloud Motion from ATS-I Spin Scan Camera Pictures

by A. F. Hasler, J. Kornfield, and L. Jensen
Space Science and Engineering Center

Abstract

A "blink"measuring technique for making quantitative geometric measurements of cloud displacements from a series of ATS-I pictures is explained. This technique requires two or more ATS-I pictures which are reasonably well superimposed by projectors on an electronic digitizing table. All geometric calculations, that is, distortion correction, superimposition and rectification, are done analytically through a computer program. The mathematical assumptions and operations involved are discussed in detail in the Appendix. A systematic testing program was devised to evaluate the technique first with an ideal grid and finally with real ATS-I pictures. Some possible applications of the technique include measurement of cloud trajectories (i.e., velocities), measurement of area change in clouds and cloud systems and measurement of location and orientation of cloud features. The best cloud displacement accuracy to date has been approximately nine nautical miles which provides cloud speeds within approximately three knots for clouds that can be observed for three hours. Preliminary comparisons of cloud trajectories with standard wind observations are presented.

Description of the Technique

At first thought, an excellent method for making quantitative measurements of cloud motions would be to project a time-lapse movie [1] made from ATS Spin Scan Cloud Camera (SSCC) pictures onto an electronic measuring table and to trace the motion of the clouds with a measuring head. Unfortunately, this method has the following limitations:

1. It is very difficult and time-consuming to superimpose the pictures accurately for the movie.
2. A registration error is introduced by the movie camera and the movie projector.
3. The resolution of presently available 16 mm. film is inadequate to preserve the picture quality over the full earth disk.
4. It is difficult to correct for variable distortion and size changes from picture to picture.

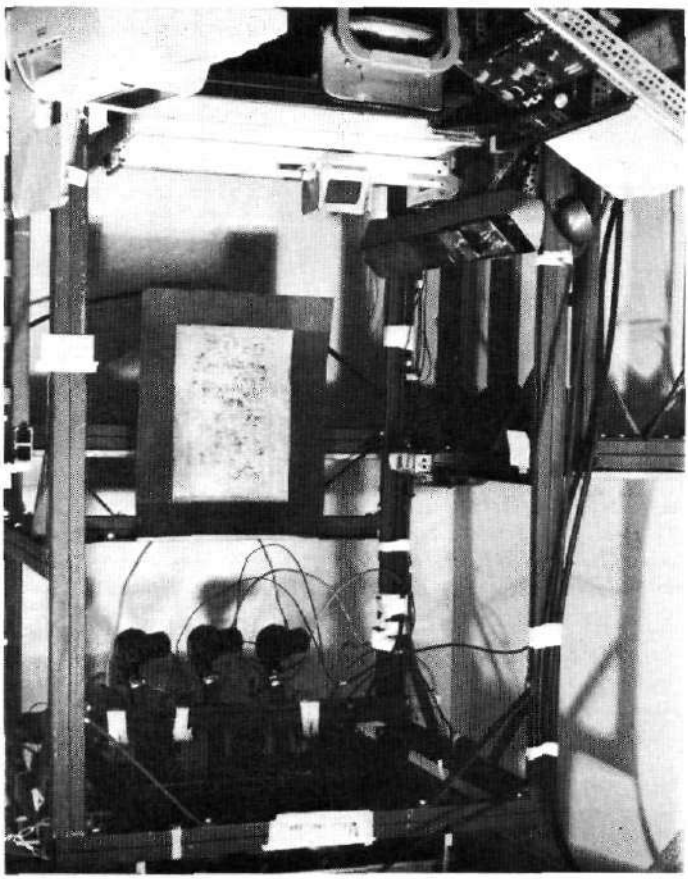

Figure 1. Projection System and Electronic Digitizing Table Used for Blink Measuring Technique. (Images from three overhead projectors are deflected onto the measuring table by a 45°-angle mirror. Projection lamp controls are on the operator's left. Operator positions measuring head by hand. The measuring head is linked to two rotary digital encoders which are interfaced through the teletype on the right to an on-line computer. X and Y coordinates of the measuring head are recorded when a foot switch is activated. The measuring system shown belongs to the High Energy Physics Group, Department of Physics, University of Wisconsin.)

A "blink" measuring system has been developed which, to a large extent, overcomes these problems. Two or three projectors are used to superimpose ATS SSCC pictures on an electronic measuring table (Figure 1). The projectors allow adjustment of the picture in the film gates such that reasonably good superimposition of images on the table is achieved. Once the images are approximately superimposed, the film remains fixed. The projection lamps are easily controlled so that it is possible to blink rapidly from one picture to another giving a "movie" effect. The electronic measuring table is a 36 in. × 36 in. projection table with a measuring head on it. The head consists of a platin with inscribed cross-hairs, which is linked to a pair of rotary digital encoders. The encoders are interfaced directly to an on-line computer. This system enables one to record the x and y coordinates of any point on any picture.

The advantages of this system are as follows: It is in fact a two- or three-frame time-lapse movie with very high resolution because of the large 70 mm. film size used. The fixed registration of the film allows the following mathematical operations: distortion correction, superimposition, rectification and all other geometric calculations to be performed on each picture individually in the computer.

Each image is located on the measuring table by determining the x and y coordinates of many points on the Earth's limb and the location of at least one landmark. The mathematical operations (discussed in detail in Part I of the Appendix) are then performed in the following manner:

1. Distortion Correction: An ellipse is fitted to the limb points by a least-squares technique and the parameters of the ellipse are computed. The Earth is then restored to a circle, correcting for any linear distortion in the picture. The pictures are scaled using the apparent Earth radii for any size variability.
2. Superimposition: The center of each circle is transposed to the origin of the measuring table coordinate system and the pictures are rotated until the landmarks coincide.
3. Rectification: The picture is regarded as that made by a conventional camera so that a tangent plane approximation can be used. Distances between any two points on one or more pictures are calculated by spherical geometry.

Test Results

A systematic testing program was devised to evaluate the technique. The measuring system and the computer programs were tested first on an ideal grid[1] and finally on real ATS-I pictures.

1. The tangent plane approximation was evaluated theoretically.[2] The error introduced by using it was found to be less than 6 nm. and was

[1] Computer-produced ATS-I grid supplied by NASA.

[2] A detailed evaluation of the tangent plane approximation is contained in Part I of the Appendix.

therefore neglected.

2. The distance-measuring calculations were carefully scrutinized for error and tested on the ideal grid by measuring distances on the measuring table. The average error in the distance between several pairs of points was only 3 nm. so the distance calculations were considered to be absolute and were used for all further evaluation.

3. The best possible accuracy with which landmarks can be located was tested by repeated measurement of the same landmark or cloud. The distance in nautical miles between successive measurements was used to give the relocation or repeatability error. For the highest quality ATS-I negatives, [3] the average error in relocating both clouds and landmarks was three nautical miles (nm), where 95% of the data points were within 6 nm. For the lower quality EIS negatives, [4] an average error of 6 nm. was found with 95% of the data points within 11 nm. When the actual measurements were made, each cloud or landmark was measured three times and the average coordinates were taken to minimize the repeatability error.

4. Next, the accuracy with which two pictures can be superimposed by the technique was tested. This was done by carrying out the superimposition routine and then measuring the apparent displacement of stationary landmarks caused by errors in the superimposition. Location errors and any distortion errors which have been neglected are also included here so that the superimposition error gives a good estimate of the total error of the technique.

For the ideal grid, grid points near the subsatellite point were found to be superimposed with an average accuracy of 3 nm. which approaches the resolution limit (about 2 nm.) of the ATS-I camera. For two different ATS-I pictures, the best superimposition achieved for points on Baja California and the Hawaiian Islands had an average error of 9 nm. These represent the best results achieved to date for real data. It has been found that clouds can often be traced for over three hours. If we use a total error of 9 nm. average cloud speeds over a three-hour period can be determined within approximately three knots. According to a COSPAR [2] report, one of the global observation data requirements for prediction with diabatic numerical models is the knowledge of the horizontal wind within four to six knots. Therefore, if it can be established that cloud speeds can be accurately related to wind speeds, we are approaching the recommended accuracy.

---

[3] Produced at The University of Wisconsin from an analog tape record of the ATS-I SSCC signal.

[4] Negatives made by the EIS (Electronic Image Systems Corporation, Boston, Massachusetts) display system at the ground station as test pictures.

Preliminary Comparison of Cloud Trajectories with Standard Wind Observations

The measuring procedure is thus: In the tropics, one selects the smallest persistent fair-weather cumulus clouds resolved by the ATS-I camera. Small cumulus clouds are used if possible because they most nearly resemble an ideal marker (i.e., a passive, infinitely small marker). Large clouds or cloud systems and large cloud decks are avoided if possible because they are more likely to affect the ambient wind field and are more likely to be propagated by wave phenomena than the smaller clouds. Distances are measured from cloud center to cloud center, as the operator determines by eye. For larger clouds whose centers cannot easily be determined, such as large convective cloud groups, bright spots or distinctive edge features are used. Cirrus clouds are less well defined and are therefore more difficult to locate accurately. However, since their velocities are usually higher, the error in location is still a small part of the distance traveled.

The first comparison of cloud trajectories with wind observations was done with data from 19 February 1967. The ATS-I SSCC pictures, taken at 2040 Universal Time (U), 2208 (U) and 2317 (U) on 19 February 1967, were selected. The ATS-I picture nearest local noon for the subsatellite point is 2208 (U). It is shown in Figure 2. Trajectories of fair-weather cumulus clouds, assumed to be low-level clouds, were compared with the surface wind observations from the US. Weather Bureau's Hawaiian analysis for 0000 (U) 20 February 1967. Trajectories of higher speed clouds, usually cirrus (assumed to be high-level clouds), were compared with the 200-250-300 millibar (mb.) wind observations from rawinsondes and aircraft doppler radar, again from the Hawaiian analysis at 0000 (U) 20 February 1967. The comparison of these data is illustrated in Figure 3. For this case, the average superimposition error was 9.3 nm. and, since the period of observation was three hours, cloud speeds can be found within approximately three knots. Of thirty cumulus trajectories and ten cirrus trajectories selected to cover the tropics as uniformly as possible, only four cases of cumulus trajectories and no cases of cirrus trajectories were found near enough (i.e., less than 200 nm.) to be compared with the standard observations. This points up the difficulty of making this type of comparison. While a more complete selection of cumulus trajectories would have given a better comparison, there were virtually no upper air wind observations near enough to the cirrus clouds visible in this picture to make any comparisons. In the four cases of cumulus trajectories, the average speed difference between cloud and surface wind was three knots or 10% of the wind speed, while the average direction departure was 10°. Transequatorial cirrus flow from north to south at approximately 145° was measured at thirty-two knots, while a "cloud jet" over Baja California and Southwestern United States, flowing to the northeast, was measured at up to fifty-two knots (see Figure 3).

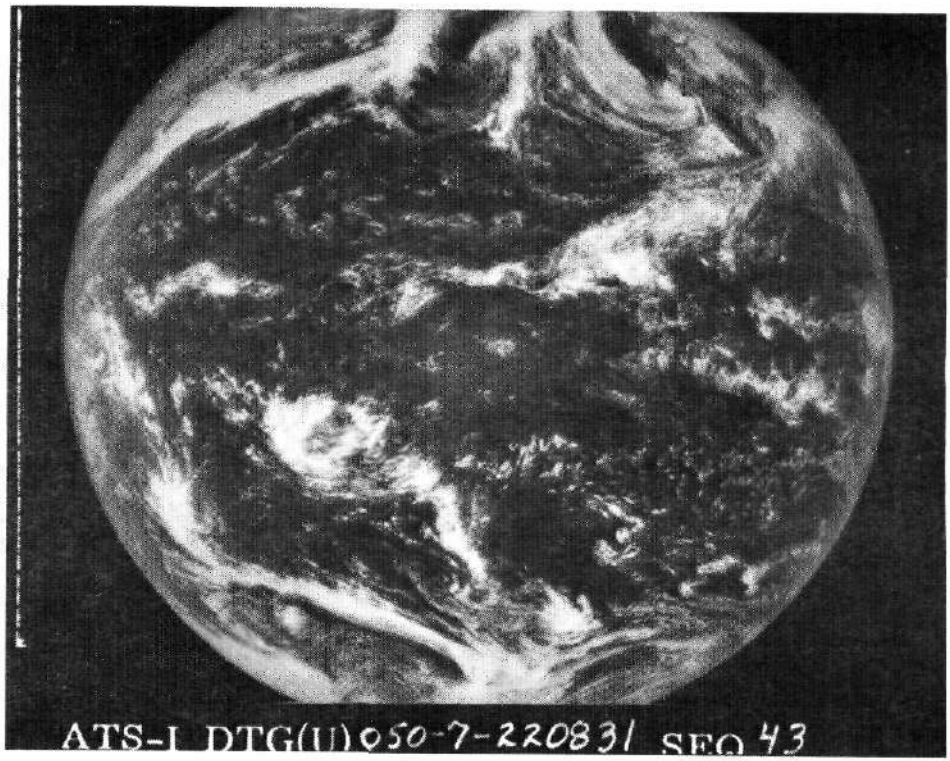

Figure 2. ATS-I SSCC Picture from 2208 (U) 19 February 1967. (Printed from a duplicate EIS negative.)

Two high-resolution negatives produced at The University of Wisconsin from analog tapes recorded at 2215 (U) on 21 June 1967 and at 0013 (U) on 22 June 1967 (Figure 4) were used for a second comparison. These negatives are much better than the duplicate EIS negatives used for the 19 February case. In fact, they preserve nearly the full resolution of the ATS SSCC. An improved comparison procedure was used for this case. First, the locations of all surface and upper air wind observations were plotted on the measuring table. The actual wind data were omitted to prevent bias on the part of the operator. Cloud trajectories were selected which coincided as nearly as possible with the wind observation locations and times. When the cloud trajectories had been measured and plotted, the wind observations were then plotted and compared, as shown in Figure 5. In this case, the average superimposition error was 18 nm. and, since the

period of observation was only two hours (negatives were not available for a longer period), cloud speeds can be found to within about nine knots. For twelve cases of tropical cumulus trajectories compared with surface wind observations, the difference between surface wind speed and cloud speed was an average of eight knots or 38% of the cloud speed, while the departure in direction averaged 15°. For four cases of cirrus trajectories compared with the 200-250-300 mb. winds, the speed departure averaged twenty knots or 46% of the cloud speed, while the direction departure averaged 30°. These are only limited preliminary results and, while some of the departure may, of course, be attributed to actual differences between cloud and wind speed, because of relatively large differences in location and unknown differences in height of the compared data, there is fairly good agreement.

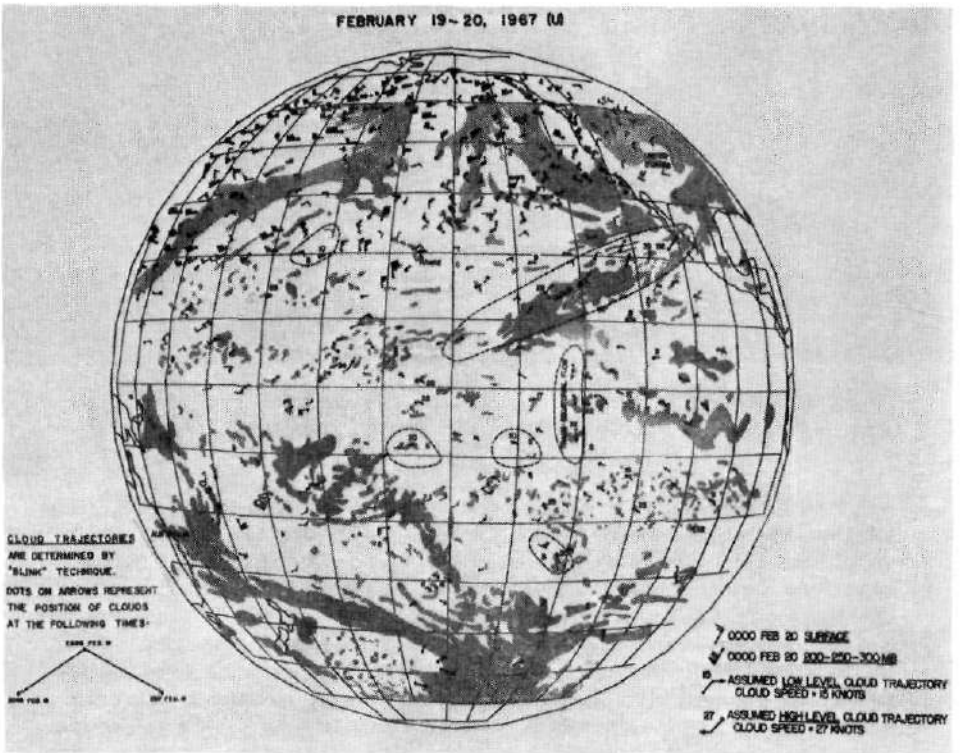

Figure 3. ATS-I Cloud Trajectories Compared with Surface and High-Level Winds (19-20 February 1967 (U)).

Figure 4. ATS-I SSCC Picture from 2215 (U) 21 June 1967. (Printed from negatives made at the University of Wisconsin from ATS-I analog tape.)

Conclusion

A practical technique for making quantitative measurements of cloud displacement from ATS-I pictures has been explained. Two ATS-I pictures were superimposed by two projectors on an electronic digitizing table. Distortion correction, superimposition and rectification were done analytically through a computer program. An estimate of the accuracy of the best results to date gave cloud speeds to within approximately three knots. A preliminary comparison of cloud trajectories with standard wind observations has been presented. Fairly good agreement was found in spite of relatively large differences in location of the compared data. Improved comparisons are planned in which cloud heights and complete wind profiles will be known.

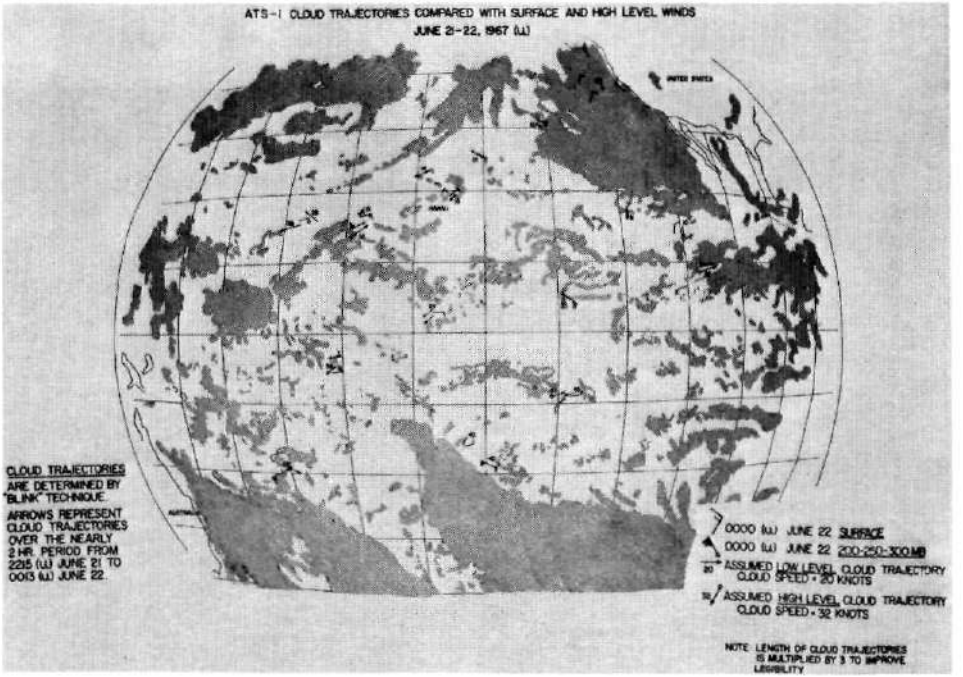

Figure 5. ATS-I Cloud Trajectories Compared with Surface and High-Level Winds. (21-22 June 1967 (U).)

Acknowledgments

This project was supported by grants from the National Aeronautics and Space Administration and Environmental Science Services Administration. The authors would like to thank Professor V. E. Suomi, principal investigator on the ATS-I Spin Scan Camera project, for his help, and NASA for providing us with the Spin Scan Camera negatives. The assistance of Ken Moss and the use of The University of Wisconsin Physics Department equipment has also been indispensable.

References

1. Hasler, A. F., and Kornfield, J.: Display and Analysis of ATS-I Spin Scan Camera Pictures Through Time-Lapse Movie Techniques. Weather in Motion, University of Wisconsin Press, in press.
2. COSPAR Working Group IV: Status Report on the Application of Space Technology to the World Weather Watch. Committee on Space Research, Paris, June 1967.

Appendix

Tangent Plane Approximation

A box camera looking directly down on the subsatellite point would produce a circular image of the Earth. An ATS picture looks the same as one taken by an ordinary box camera; however, the Spin Scan Camera picture is a display of the intensities observed by its telescope as a function of the telescope's stepping and rotation angles. In order to find how much the two pictures actually differ, we first set up a coordinate system as follows.

Let the origin of the coordinate system be at the satellite as shown in Figure A-1. The x-axis is directly along the line connecting the satellite's center and the Earth's center. The z-axis is parallel to the Earth's axis of rotation with the positive direction northward. The y-axis is perpendicular to both the x- and z-axes so as to form a right-handed coordinate system.

Angular variations in the x-z plane are designated θ and measured from the x-axis. θ is the stepping angle of the ATS camera. In the x-y plane the angular variations are designated by ϕ and are also measured from the x-axis. ϕ is the rotational angle of the satellite about its nominal spin axis z.

When viewed by an ordinary box camera, the Earth's disk would appear as a perfect circle formed by the rays tangent to the planet. To find the equation for the Earth's limb in spin scan picture coordinates, we refer to Figure A-1, in which the circle is formed by the tangents and lies in plane P'. Plane P' is described by the equation

$$x = \text{Constant} \tag{A-1}$$

If we express x in spherical coordinates, $x = R \cos\theta \cos\phi$. When R is fixed as the distance from the Earth's limbs to the satellite, one obtains the equation of the circle:

$$R \cos\theta \cos\phi = R \cos M \tag{A-2}$$

where 2M is the angle subtended by the Earth as seen from the satellite.

When the satellite's spin axis is tilted away from z by an angle, τ, we have merely a rotation about the y-axis so that the equation (A-2) becomes

$$\cos\theta \cos\phi \cos\tau + \sin\phi \sin\tau = \cos M \tag{A-3}$$

Since the Earth's limb looks quite circular on an ATS picture, we approximate equation (A-3) as

$$(\theta - \tau)^2 + \theta^2 - M^2 = 0 \qquad \text{(A-4)}$$

To test the approximation, values of θ, ϕ, τ and M were chosen that satisfied equation (A-3). The same values were used in equation (A-4). The amount by which equation (A-4) differed from zero was used to estimate the error in θ or ϕ. For a large tilt angle of $\tau = 2°$, the greatest error in θ and ϕ was less than 3×10^{-4} radians, or an error of about 6 nm. at the limb of the Earth. Since τ is normally much less than $2°$ in the pictures used and the largest error occurs only in limited areas near the limb, the error is considered to be less than 6 nm. and has been neglected.

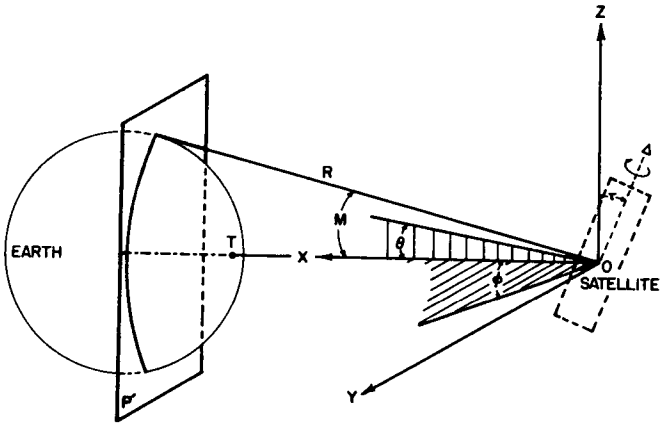

Figure A-1. ATS SSCC Coordinate System. (The origin of the coordinate system, 0, is at the center of the satellite. The x-axis is directed along the line connecting the satellite's center and the Earth's center and passes through the subsatellite point T. The z-axis is parallel to the Earth's axis of rotation. The y-axis is mutually perpendicular to the x- and z-axes. θ is the stepping angle of the SSCC telescope. ϕ is the rotational angle of the satellite about its nominal spin axis z. τ is the deviation or tilt of the satellite spin axis with respect to z. If a line is constructed which passes through 0 and is tangent to the Earth's surface, R is the distance from 0 to the tangent point. The circle defined by all of these tangent points lies in the plane P'. M is the angle between the tangent line and the x-axis.)

Distortion Correction and Superimposition

A step-by-step description of the distortion correction and superimposition process is given below and illustrated in Figure A-2. A detailed discussion of each step follows the list.

1. Fit an ellipse to the limb of the Earth (Figure A-2, Part 1).

2. Determine the angle between the major axis of the ellipse and the x-axis of the measuring table coordinate system (MTCS) (Figure A-2, Part 2).

3. Rotate the MTCS through this angle so that the x-axis is parallel to the major axis of the ellipse (Figure A-2, Part 3).

4. Determine the semi-major and semi-minor axes of the ellipse.

5. Translate the origin of the MTCS to the center of the ellipse (Figure A-2, Part 4).

6. Transform the ellipse into a circle (Figure A-2, Part 5).

Each of the pictures is processed separately as above. Then a final step with both pictures produces the final superimposed image.

7. Rotate one picture relative to another so that vectors to a landmark $\vec{L}_1$ and $\vec{L}_2$ are superimposed (Figure A-2, Part 6).

Each of these steps will now be taken up in more detail. The major distortion correction involves transforming the distorted Earth into a circle. The elliptical distortion is introduced when the SSCC scan lines are not reproduced with the proper line spacing or when linear stretching of the photographic material occurs. To determine the shape of the ellipse a least-squares fit to the limb of the Earth is made using the general equation for a conic section:

$$Z^2 + T_1 yz + T_2 y^2 + T_3 z + T_4 y + T_5 = 0 \qquad \text{(A-5)}$$

where $T_1 \ldots T_5$ are fitted coefficients and y, z are the measuring table coordinates.

A rotation of the MTCS gives the elliptical equation

$$z^2 + (\frac{S}{P})z + (\frac{Q}{P})y^2 + (\frac{T}{P})y + (\frac{T_5}{P}) = 0 \qquad \text{(A-6)}$$

where

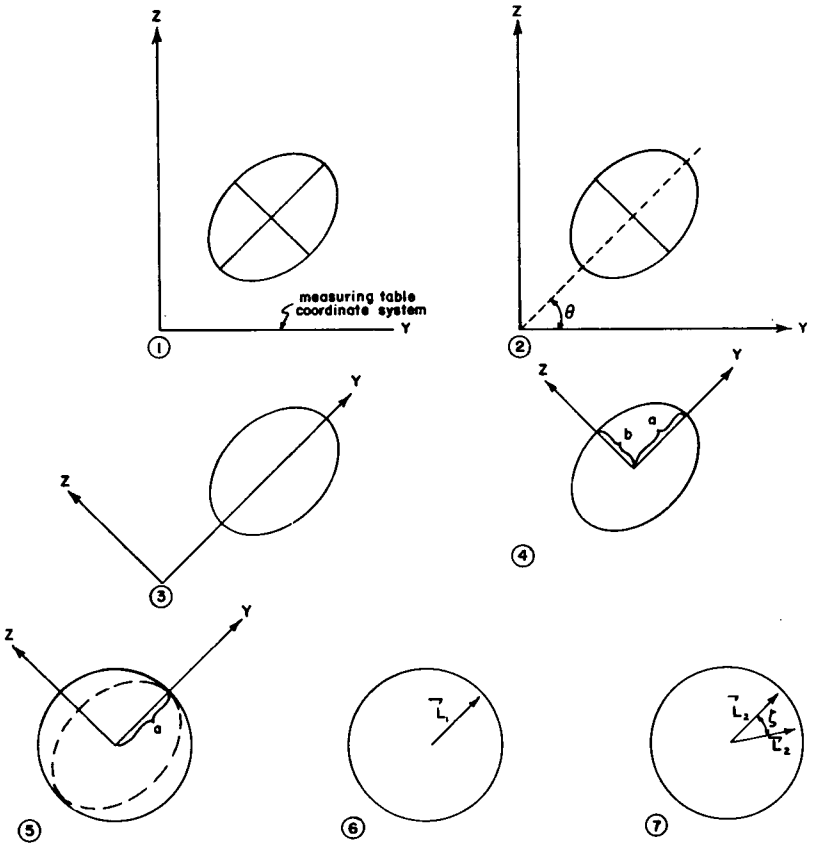

Figure A-2. Step-by-step Process of Distortion Correction and Superimposition of ATS-I SSCC Pictures. (1. The elliptically distorted Earth arbitrarily positioned on the MTCS. 2. Determination of the angle between the major axis of the ellipse and the x-axis of the MTCS. 3. Rotation of the MTCS so that the x-axis is parallel to the major axis of the ellipse. 4. Translation of the origin of the MTCS to the center of the ellipse. 5. Transformation of the ellipse into a circle of radius a. 6. Rotation of one picture relative to another such that the vectors to a landmark, $\vec{L}_1$ and $\vec{L}_2$, are superimposed.

$$P = \cos^2\theta + T_1 \cos\theta \sin\theta + T_2 \sin^2\theta$$

$$Q = \sin^2\theta - T_1 \cos\theta \sin\theta + T_2 \cos^2\theta$$

$$S = T_3 \cos\theta + T_4 \sin\theta$$

$$T = -T_3 \sin\theta + T_4 \cos\theta$$

The angle θ is the smallest angle obtained from

$$\tan 2\theta = \frac{T_1}{1 - T_2} \tag{A-7}$$

Finding equation (A-6) is equivalent to the rotation discussed in steps two and three. This equation can be modified further by completing the square and rearranging terms:

$$\frac{(x - x_0)^2}{a^2} + \frac{(y - y_0)^2}{b^2} = 1 \tag{A-8}$$

where

$$x_0 = -\frac{S}{2P} \qquad a^2 = \left(\frac{S}{2P}\right)^2 + \frac{T^2}{4PQ} - \frac{T_5}{P}$$

$$y_0 = -\frac{T}{2Q} \qquad b^2 = a^2 \frac{P}{Q}$$

The semi-major and semi-minor axes are a and b, respectively. The center of the ellipse is at (x_0, y_0). Translation of the origin is accomplished by subtracting x_0 from every measured x and subtracting y_0 from every y. Transformation of the ellipse into a circle is accomplished by multiplying the translated y coordinate by the ratio a/b. The variation of the Earth's radius from its mean value is approximately 6 nm. so we can regard the Earth to be a circle. The circle then has radius a. Every time a distance is measured on the picture, it is divided by a. This normalizes every circle so that they are equivalent.

The final rotation is accomplished using vectors $\vec{L}_1$ and $\vec{L}_2$ on pictures one and two, respectively. $\vec{L}$ is a vector from the origin to a particular landmark. The angle, ζ, between $\vec{L}_1$ and $\vec{L}_2$ is given by the dot product

$$\vec{L}_1 \cdot \vec{L}_2 = |\vec{L}_1||\vec{L}_2| \cos\zeta \tag{A-9}$$

One picture is then rotated with respect to another through the angle ζ. The procedure by which this is accomplished is discussed in the next section.

The process of superimposition is complete once the above is carried out. Displacements of clouds between the two pictures may now be computed since the two pictures can be regarded as one picture.

Rectification

The last problem is one of rectification or one of relating geometric distances on the photograph to actual distances on the Earth's surface. For the case of finding cloud trajectories, the cloud displacement D is desired.

On a spherical Earth, the subsatellite point (SSP) and the positions of two clouds can be used to locate a spherical triangle. If we know two arcs, σ_1 and σ_2, and one angle, β, the third arc, ξ (or $D = R\xi$, where R is the Earth radius and D the displacement), can be found. See Figure A-3. This situation is analogous to looking down upon the North Pole, where β is the longitude separation between two arcs of the triangle and each σ is 90° minus the latitude. D is the great circle distance between two clouds (or, in the case of one cloud, the displacement). Let us find the angles σ_1 and σ_2 first.

Using the same coordinate system as in Figure A-1, position a plane P perpendicular to x at the SSP. The arc length for σ_1 projects onto P as a straight line ℓ_1, with endpoints $(H, 0, 0)$ and (H, y_1, z_1). H is the height of the satellite above the Earth's surface. See Figure A-4.

The line r_1, from the origin through (H, y_1, z_1), intersects the Earth as shown in Figure A-5. Figure A-5 is just a cross-section from Figure A-4.

The equation of the circle with center at E is:

$$[x - (R + H)]^2 + \rho^2 = R^2 \qquad H \leq x \leq 2R + H \qquad \text{(A-10)}$$

The line r_1 has equation

$$\rho = x \tan \alpha \qquad \text{(A-11)}$$

where

$$\cos \alpha = \cos \theta \cos \phi \qquad \text{(A-12)}$$

Substituting (A-11) into (A-10) and solving for x allows us to find σ_1 from

$$\tan \sigma = \frac{x \tan \alpha}{(R + H) - x} \qquad \text{(A-13)}$$

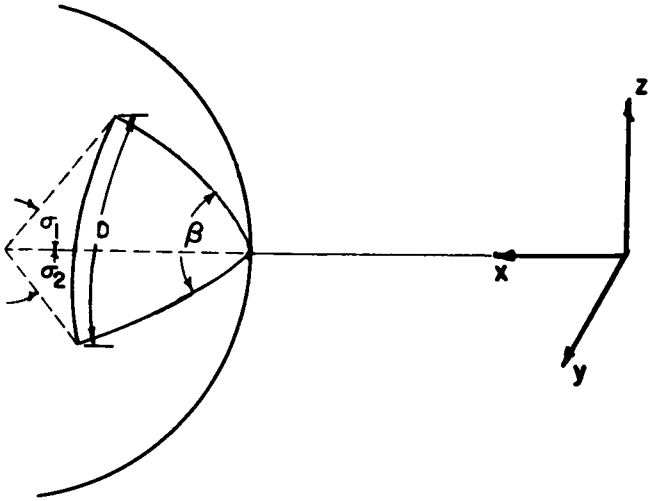

Figure A-3. Spherical Triangle Used to Calculate a Displacement, D, on the Surface of the Earth Which is Part of the Rectification Process for ATS SSCC Pictures. (If we know two arcs, σ_1 and σ_2, and one angle, β, the third side, ξ (or $D = R\xi$, where R is the Earth radius and D is the displacement), can be found.)

The process is repeated for σ_2. Thus, we have two sides of the triangle.

To find the remaining angle, β, we define the vector $\vec{\ell}_1$ as the vector of length ℓ_1 from the SSP (H, 0, 0) to H, y_1, z_1). Vector $\vec{\ell}_2$ is similarly defined. Thus, by the dot product of two vectors

$$\beta = \cos^{-1}\left(\frac{\vec{\ell}_1 \cdot \vec{\ell}_2}{|\vec{\ell}_1||\vec{\ell}_2|}\right) \qquad \text{(A-14)}$$

The final side of our triangle follows directly from the spherical trigonometric relation

$$\cos\xi = \cos\sigma_1 \cos\sigma_2 + \sin\sigma_1 \sin\sigma_2 \cos\beta \qquad \text{(A-15)}$$

whence the displacement, D, is

$$D = R\xi \qquad \text{(A-16)}$$

where R = Earth's radius.

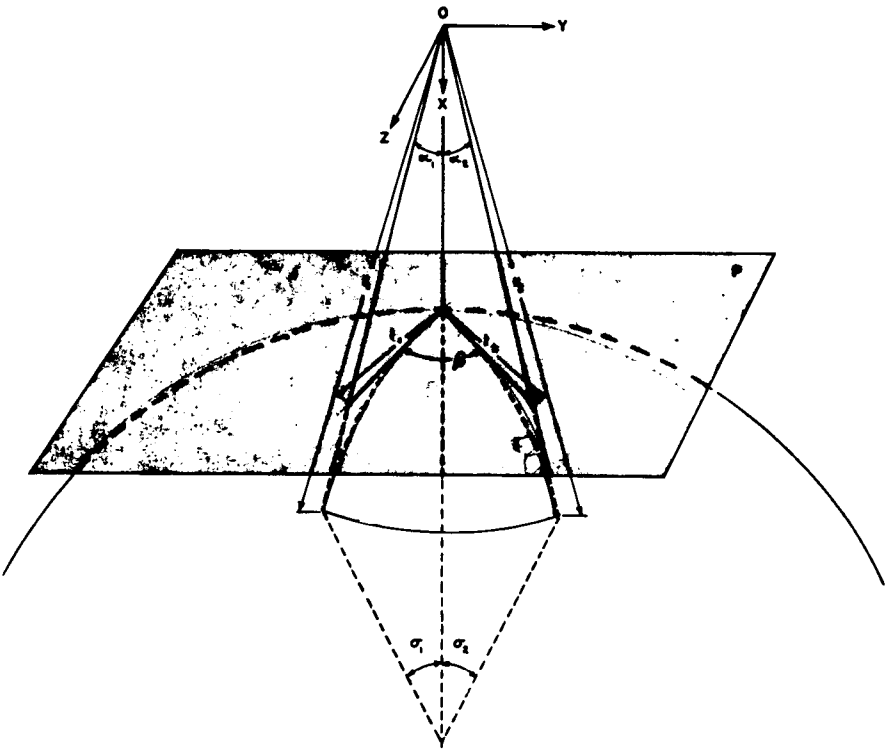

Figure A-4. Geometrical Relationships Used to Rectify ATS SSCC Pictures. (r_1 = distance from origin to surface of Earth; α_1 = angle between r_1 and the x-axis; P = plane tangent to the Earth at the subsatellite point; σ_1 = great circle angle (see Figure A-3); ℓ_1 = projection of arc length corresponding to σ_1 onto plane P; β = angle between ℓ_1 and ℓ_2, also angle between great circle segments $R\sigma_1$ and $R\sigma_2$, where R is the radius of the Earth. (See Figure A-3.)

Note: The last step of superimposition (rotation through the angle ζ as defined in equation (A-9)) is accomplished by subtracting ζ from β each time β is calculated.

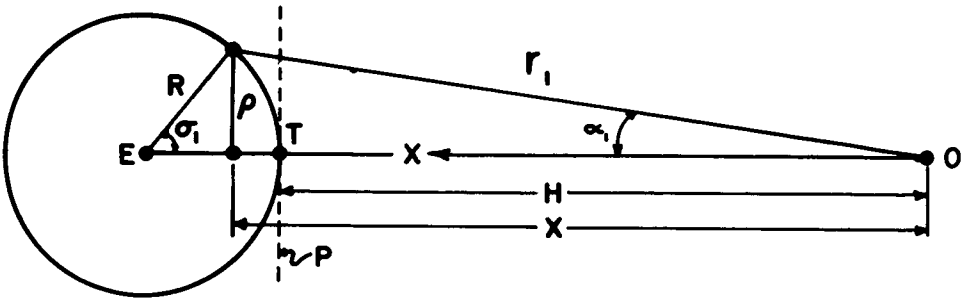

Figure A-5. Cross-Section of Figure A-4. (H = height of the satellite above Earth; ρ = half chord length; X = distance from origin to the intersection of ρ with the x-axis; R = radius of the Earth; E = center of the Earth; T = subsatellite point; P = plane tangent to Earth at subsatellite point.)

CONVECTIVE TRANSPORT OF MASS AND ENERGY IN SEVERE STORMS OVER THE UNITED STATES—AN ESTIMATE FROM A GEOSTATIONARY ALTITUDE

D. N. Sikdar, V. E. Suomi and C. E. Anderson

Abstract:

Some important characteristics of intense convection associated with tornado vortices are described in a case study based on photographs of the United States on 19 and 23 April, 1968, that were transmitted from NASA's geosynchronous satellite, ATS-III. The growth rates of a number of convection complexes as estimated from the satellite cloud photographs are studied. Based on a three-layer convection model, the upward fluxes of mass and energy in these severe storms are computed. The computed fluxes seem to be higher by at least one order of magnitude than in a moderate thunderstorm (Brown, 1967).

It is suggested that the pronounced growth rate of a convection complex as estimated on the ATS-III satellite photographs should be an indication of the presence of severe storm cells below the cirrus canopy.

1. Introduction

The thunderstorm is of major importance in meteorology, not only because it is a weather hazard but also because it is an important link in the redistribution of energy from the lower to the upper troposphere.

For many years the study of severe thunderstorms has been inhibited by lack of data, partly because of the size and nature of the storms. Thunderstorm models and theories of cumulonimbus convection have been greatly influenced by the data gathered on small thunderstorms by the Thunderstorm Project (1949). The investigators tacitly assumed that the results of these small-scale studies could be extrapolated to explain more intense storms.

The Spin Scan Camera systems, University of Wisconsin experiments onboard ATS-I and ATS-III geostationary satellites, have presented another aspect of the thunderstorm.

The purpose of this paper is to show that it is possible to isolate the regions of probable severe weather over the United States from the ATS-III satellite cloud photographs and also to estimate the convective transport of mass and energy by deep convection in the mid-latitude disturbance field. This case study pertains to a satellite-observed cloud system over the United States on 19 and 23 April, 1968, when widespread tornado activity was reported by ground stations.

The severe local storm: A model

Thermal stratifications in a severe storm

In the past two decades a number of convection models have been proposed to explain the observed dynamical properties of cumulus convection. Most cumuli exhibit temperatures and liquid water contents much lower than those of undiluted parcels and, due to buoyancy exhaustion, terminate much below the level prescribed by the classical parcel theory. Nevertheless, radar and visual observations of severe thunderstorms have shown tropopause penetrations of a few kilometers on several occasions. Large accelerations are required to produce sufficiently high speeds at the tropopause to accomplish such penetrations. These accelerations cannot be achieved unless the amount of entrainment occurring in the rising updraft is reduced. In the absence of entrainment, the maximum amount of buoyancy is realized from the condensation process and high velocities are possible. Fujita and Grandoso (1966) have proposed that the entrainment rate is inversely proportional to the cloud diameter. For a giant cloud of 20 km diameter, the entrainment is insignificant under this assumption (Fujita and Grandoso, 1966).

With this hypothesis in mind, a three-layer convection model is proposed for a severe storm. First is the layer of inflow (LOI), extending from the ground to the lifting condensation level (LCL). Second is the layer of vertical motion (LVM), which extends from the LCL to the top of the tower, where the buoyancy is exhausted. The warm moist air drawn in from the LOI is carried upward undiluted in the LVM, rotating cyclonically and losing water as it rises until finally it is ejected out of the storm in the third layer, the layer of outflow (LOF) near the tropopause. The LOF is assumed 1.0 km thick (Ludlum, 1966). The top of this layer is sharply defined by the upper surface of the anvil cloud. On the satellite cloud photographs this glaciated surface appears brighter because of the significantly greater reflectance characteristics of the ice crystals in the visible region of the solar spectrum compared with the reflectance of low and middle clouds composed mainly of water droplets. The cloud brightness, however, depends on many factors such as cloud form, depth, type, concentration, and the illumination condition.

A schematic diagram of the model is presented in Fig. 1.

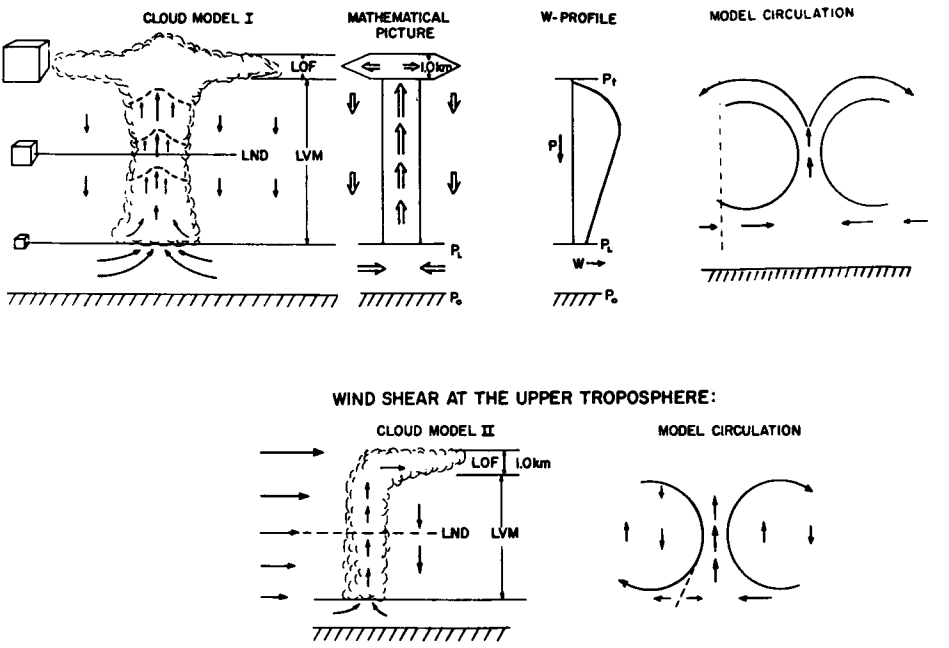

Fig. 1. Schematic diagram for the proposed convection model

Computation of latent heat flux

From the equation of state the volume flux at the LOF is derived as:

$$\frac{dV_0}{dt} = \frac{K}{\rho_L} \frac{dM_L}{dt} \tag{1}$$

where suffixes 0 and L stand for the base of the LOF and the top of the LOI, respectively; M_L is the mass; ρ_L is the air density (10^{-3} g/cm^3) assumed independent of time; and K is a constant determined from the environmental upper air soundings.

One can relate the cloud divergence at the LOF to the cloud area change (Sikdar and Suomi, 1968) by:

$$\nabla_H \cdot V_c = \frac{I}{A_c} \frac{dA_c}{dt} \tag{2}$$

where suffix c stands for cloud particles and A_c represents the cloud area.

This cloud divergence is analogous to the horizontal spread of smoke particles in the atmosphere when a rising smoke plume strikes a stable layer.

From the equations 1 and 2, the mass flux at the cloud base is given by:

$$\frac{dM_L}{dt} = \frac{\rho_L}{K}\left(\Delta Z \cdot \frac{dA_c}{dt}\right), \text{ g/sec}$$

where $\Delta Z = 1.0$ km (Ludlum, 1966; Borovikov, 1963). The term dA_c/dt is measured from successive ATS pictures.

Assuming that the equivalent potential temperature is constant at the LCL and that all water vapor passes to the condensed phase while ascending through the cloud core, the latent heat flux E_c can be determined from the equation:

$$E_c = L \cdot \Delta W \cdot \frac{dM_L}{dt} \text{ cal/sec}$$

where

$L = 597$ cal/g at 0°C,

$\Delta W = (W_L - W_0)$ g/kg,

W_L = mixing ratio at cloud base,

W_0 = mixing ratio at cloud top.

Identification of severe storm on ATS-III pictures and the technique of their analysis

Cumulus and cumulus congestus largely appear as aggregates on the ATS-III satellite cloud photographs. Identification of cumulonimbus or storm clouds in the widespread cumulus field is largely a problem of distinguishing their brightness gradients. A uniform field of broken cumulus congestus at best appears as a white haze, whereas a resolved cumulonimbus or a complex of cumulonimbi exhibits strong brightness and well-defined boundaries. Furthermore, on the time-lapse photographs one can easily distinguish the severe storm clouds by their rapid growth rates. On occasions, these rapidly growing storms are associated with clear space in their vicinity. The brightness of these cloud boundaries is significantly enhanced by the presence of a clear zone around them. Figs. 2 and 3 show a few such examples. Cloud samples shown in Fig. 2B are located over the northern part of Mexico.

The outlines of these identified storm clouds have been tracked on successive satellite photographs, each fourteen minutes apart on 19 April and

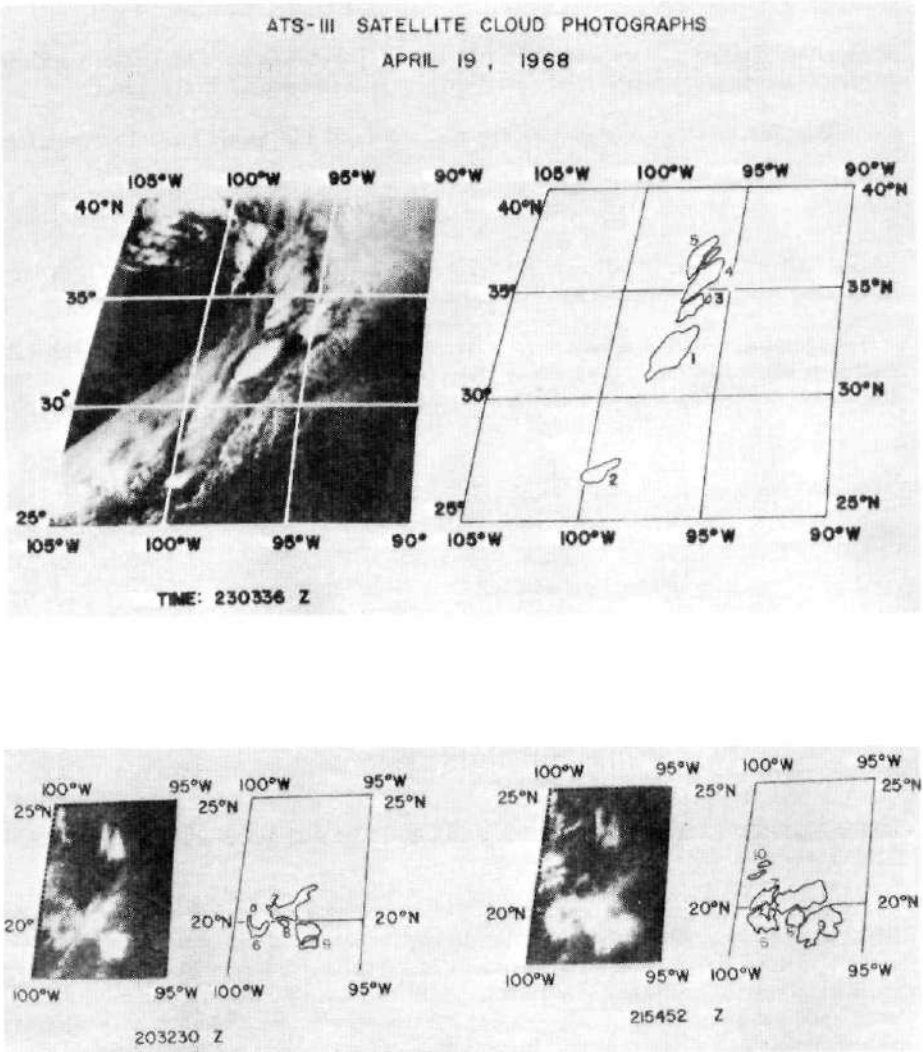

Fig. 2. Severe storm clouds over the United States on 19 April, 1968

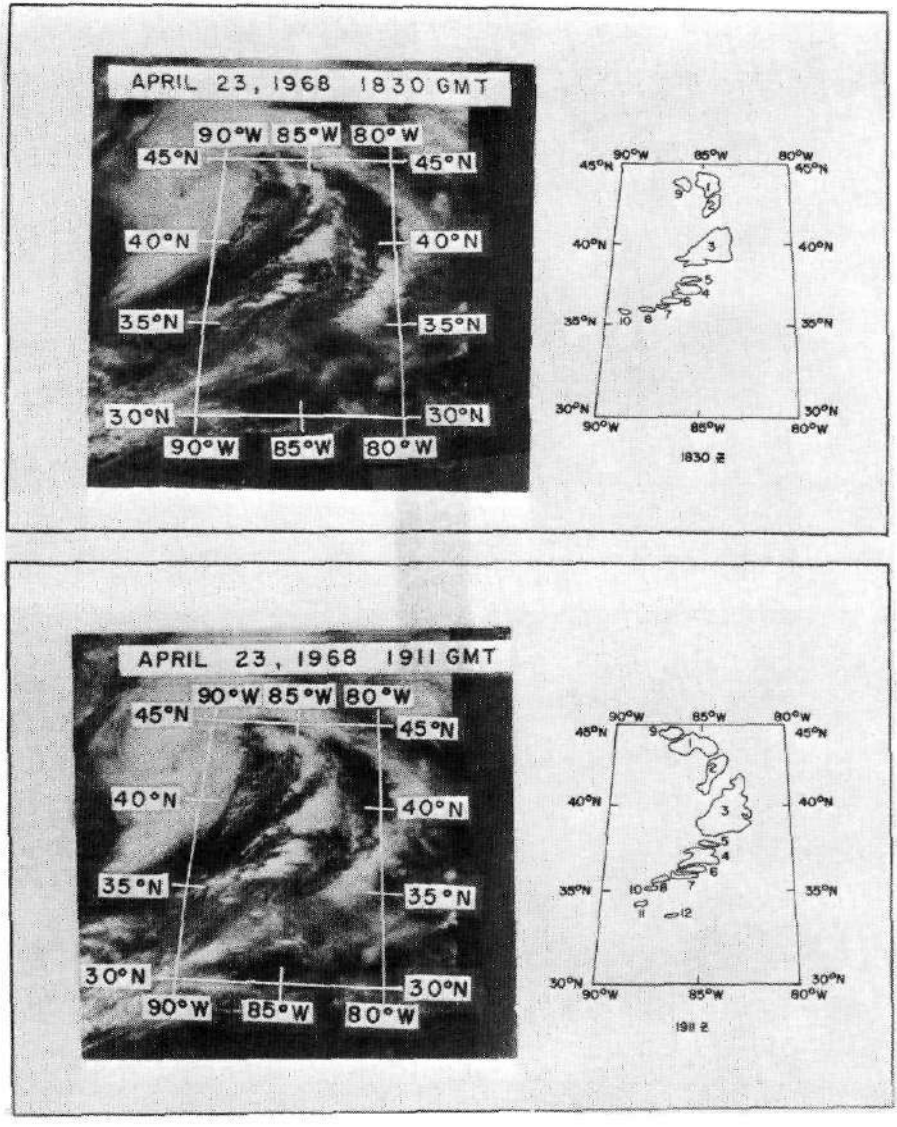

Fig. 3. Severe storm clouds over the United States on 23 April, 1968

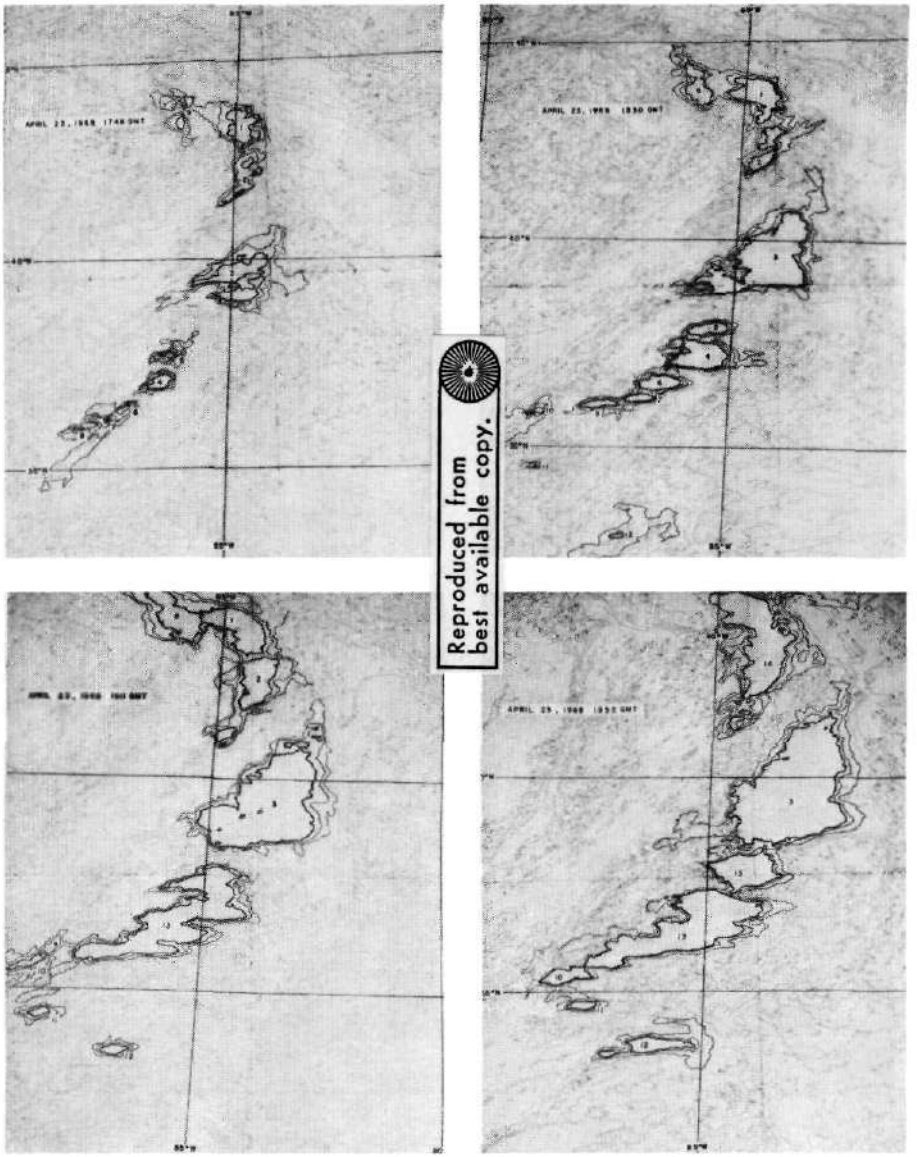

Fig. 4. Brightness contour display of severe storm clouds shown in Fig. 3.

forty-five minutes apart on 23 April. For a quick estimate of the growth rate of these storm cells this technique seems adequate. For better precision, however, one can measure the area change enclosed by a particular brightness contour corrected for solar zenith angle as a function of time. For example, Fig. 4 shows a photograph of a computer-made brightness contour actually used for preparing the 23 April data set.

Fig. 5 presents the time variation of the area of cirrus canopy evaluated from successive satellite photographs. This diagram clearly indicates a significantly rapid cirrus shield expansion over some of the storm complexes, for example, cloud numbers 1, 2, and 5 on 19 April and numbers 3 and 13 on 23 April. These pronounced growth rates obviously reflect on the degree of instability in the concerned region.

The estimates of cloud bases and cloud tops have been made using the parcel technique, from the available afternoon upper air soundings in the vicinity of the storms. Table 1 presents the thermodynamic data used in this computation scheme.

Cloud divergences and the severe storm reports over the United States on 19 and 23 April, 1968

Fig. 6 presents the cloud divergence as a function of time. These magnitudes represent the averages of a number of storm cells embedded in the com-

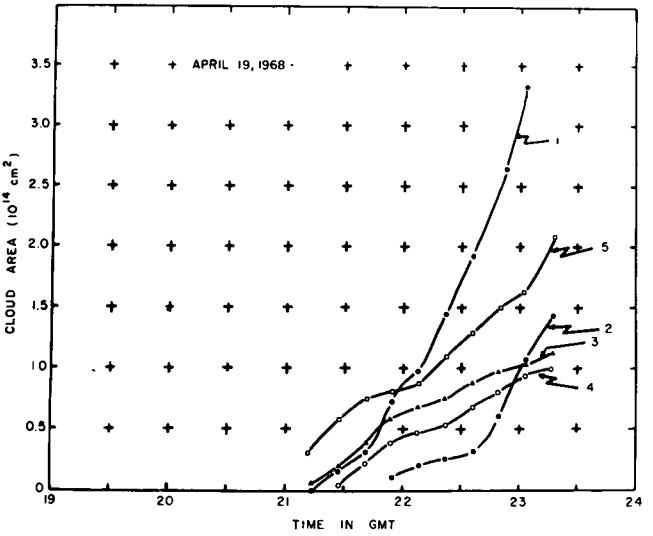

Fig. 5a Cloud area as a function of time.

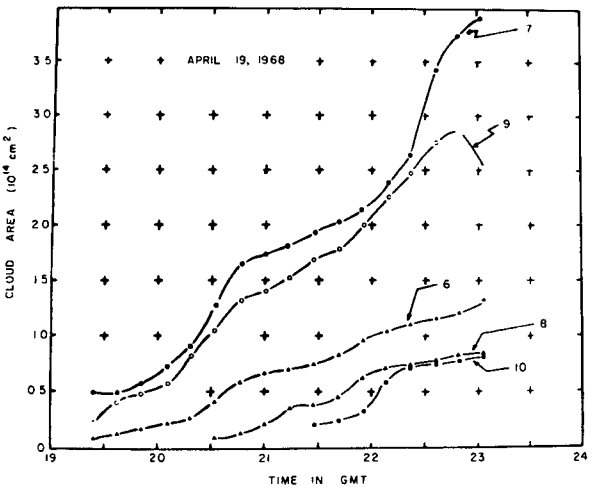
APRIL 19, 1968
CLOUD AREA (10^{14} cm^2)
TIME IN GMT
7
9
6
8
10

Fig. 5b

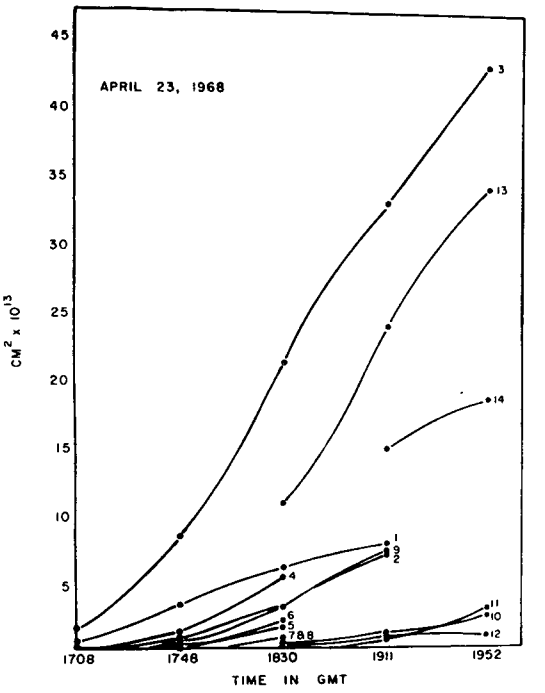
APRIL 23, 1968
CM^2 x 10^{13}
TIME IN GMT
3
13
14
1
9
2
4
6
5
7
8
11
10
12

Fig. 5c

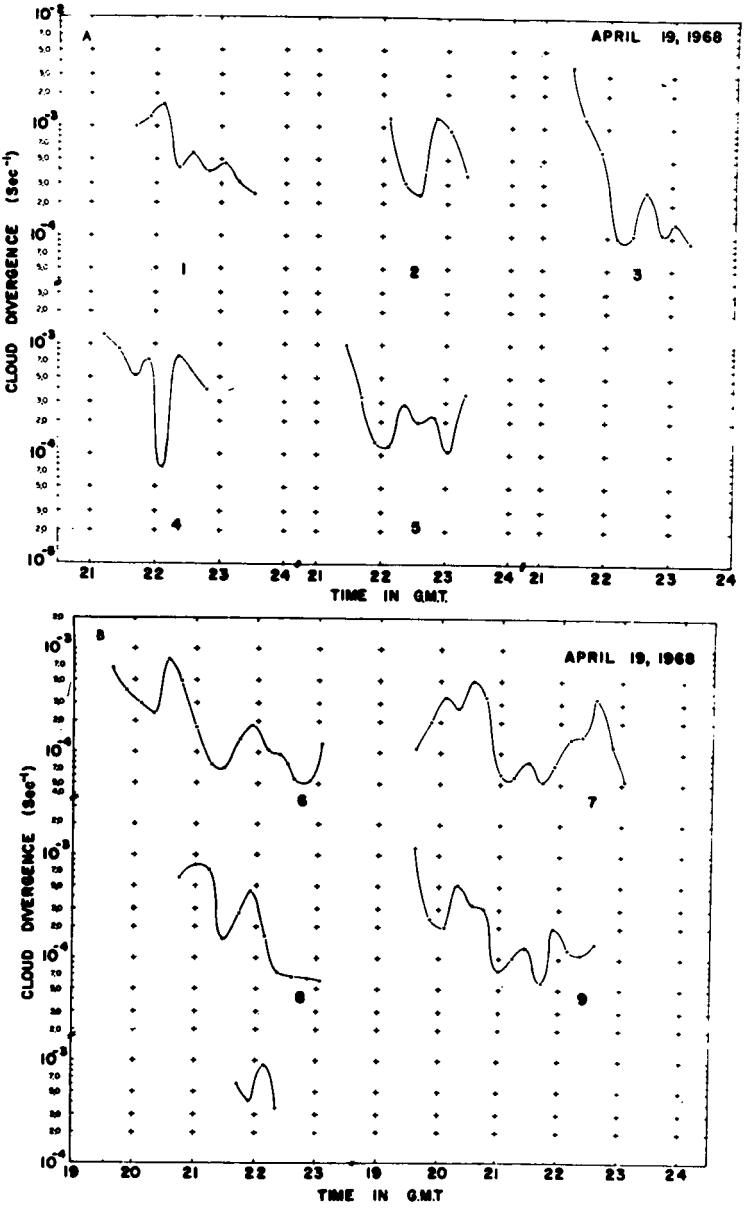
A
APRIL 19, 1968
CLOUD DIVERGENCE (Sec⁻¹)
1
2
3
4
5
TIME IN G.M.T.
B
APRIL 19, 1968
CLOUD DIVERGENCE (Sec⁻¹)
6
7
8
9
TIME IN G.M.T.

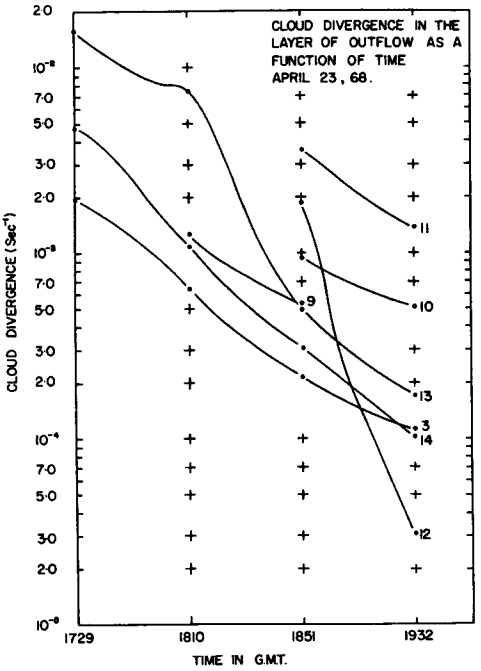

Fig. 6. Cloud divergences in the layer of outflow

Table 1. Thermodynamic data

	Cloud (mb)		Mixing ratio (g/kg)		Temperature (°K)	
Date	Base	Top	W_L	W_0	T_L	I_0
19 April, 1968	930	220	10	0.1	298	215
23 April, 1968	780	330	6	0.3	278	233

plex. In the diagrams of 19 April, wide fluctuations in the cloud divergence field can be seen. These fluctuations are probably due to eddies of various sizes participating in severe storm cloud growth. The absence of any such characteristics on 23 April is because of lower sampling frequency.

Fig. 7 presents the plot of severe storm reports over the United States

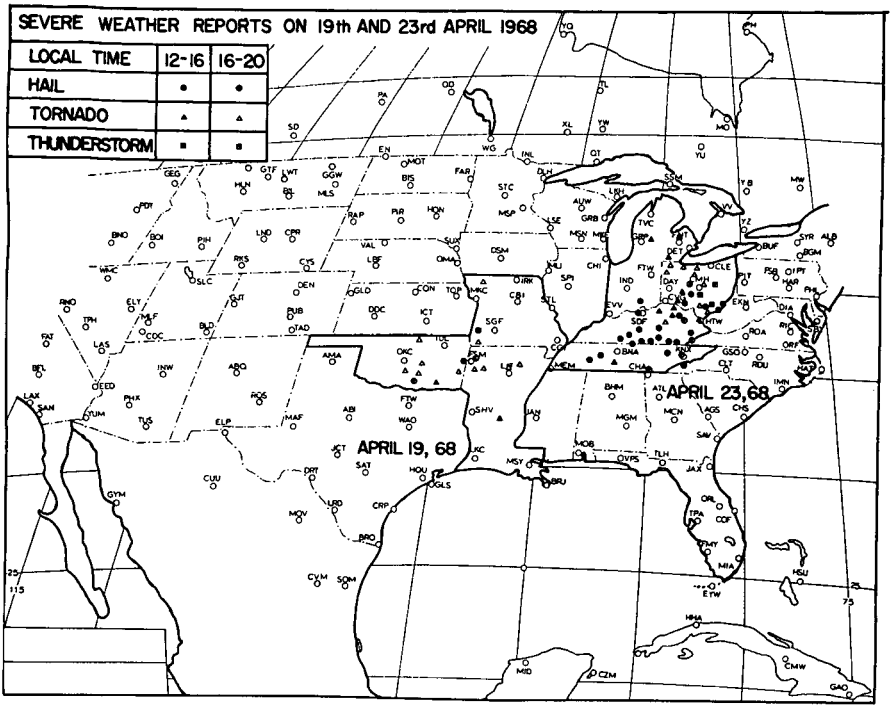

Fig. 7. Regions of severe weather over the United States on 19 and 23 April, 1968.

for 19 and 23 April, 1968. The approximate time of occurrence of each severe storm is indicated by a symbol. On 19 April, most of the severe storms occurred between 20.00 and 24.00 GMT in Oklahoma and between 00.00 and 06.00 GMT, i.e., in the late evening, in Arkansas and Missouri.

On 23 April, widespread severe weather was reported in Michigan, Ohio, Kentucky, and Tennessee in the afternoon hours. The times of occurrence indicate that the severe weather features moved east-northeastward in the late evening. These occurrences of severe weather are clearly related to the cloud systems shown in Fig. 3. The surface reports and satellite data are not adequate to correlate the specific occurrences with the cloud features observed at mesoscale; however, a number of tornados have occurred in cloud complexes 3, 13 and 14 in Fig. 3 on 23 April in the later part of the observation period.

An examination of the times of occurrence of severe weather shown in Fig. 7 and of the corresponding cloud divergence profiles shown in Fig. 6 reveals that most of the severe weather occurred during the partial decay phase of these cloud systems. Furthermore, the cloud divergence profiles on 23 April indicate significantly higher magnitudes in the growth phase than occurred on 19 April. These higher divergence rates are obviously related to the stronger vertical motion field; hence, they might be the reason for greater severity in the storms and higher density of population on 23 April. The cloud divergence at the top of an intense convection zone can be calibrated to estimate the probable severity of a particular weather phenomenon for the succeeding few hours.

Mass and energy fluxes

Fig. 8 presents the time variation of mass influx rate at the subcloud layer for cloud complexes shown in Fig. 2. Fig. 9 shows the model estimates of latent heat fluxes on 19 April and 23 April.

Brown (1967) has compiled all published data on the convective cloud growth rates (Anderson, 1960; Higuchi, 1965) and has developed a power function to estimate the growth rate and available energy. In an isolated moderate cumulonimbus cloud one expects a mass upward flux of the order of 10^7 kg/sec at lower levels. Braham (1952) also quotes the same order of magnitude for a moderate thunderstorm. Figs. 8 and 9, however, show that the orders of magnitude range from 10^8 to 10^9 kg/sec for the mass upward flux while for the heat flux the range is 10^{12} to 10^{13} cal/sec, about one to two orders of magnitude higher than in an ordinary thunderstorm.

Fig. 9B refers to the upward energy fluxes associated with a number of severe storms (see Fig. 2B) occurring over Mexico (around 20° N) on 19 April. These clouds show a strong fluctuation in the vertical transport of heat and mass. Here again, the magnitudes of energy fluxes are greater by at least one order of magnitude compared with that of a moderate thunderstorm, although their cloud structures are appreciably different from those shown in Figs. 2A and 3. These clouds exhibit structures with ill-defined fuzzy edges. The absence of sharp boundaries in these cloud systems may be attributed to the lesser moisture contrast between the cloud periphery and the clear zones, a feature generally observed in the subtropical convective systems. No definite reason for this structural difference is known to us at present. It is possible that in the subtropical storm clouds the subsidence is important at low levels.

Summary

In this paper we have shown that the convective systems causing severe weather along the frontal zones in the mid-latitude disturbance field can be identified and tracked on the ATS-III satellite time-lapse photographs. The

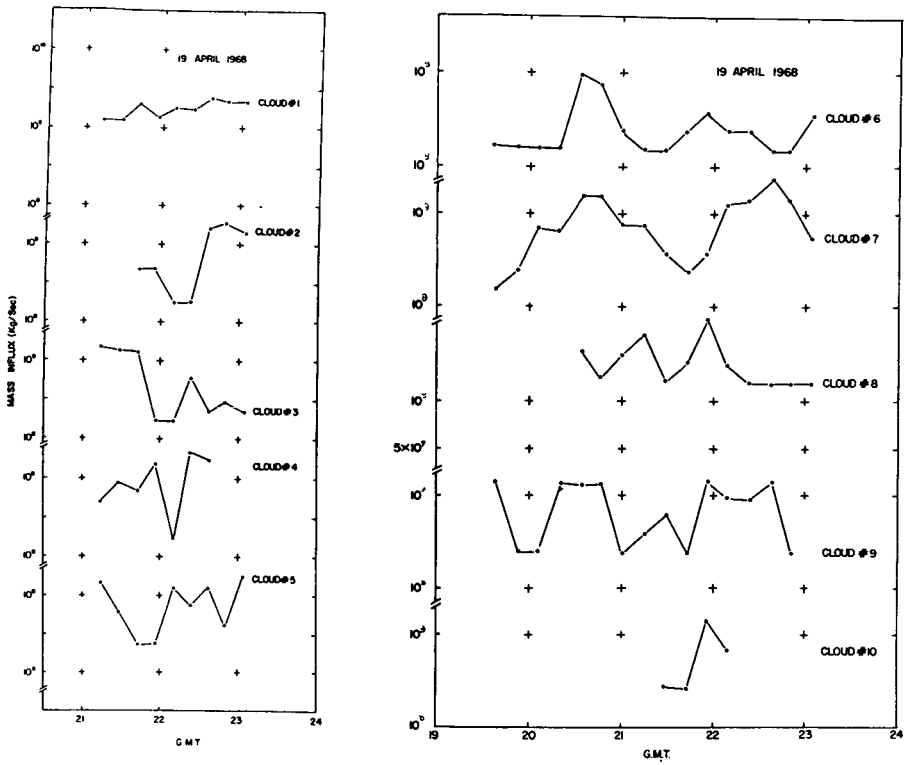

Fig. 8. Mass influx at the sub-cloud layer as a function of time.

severity of weather can probably be assessed from the growth rate of these cloud systems. A convective cloud complex indicating an average cloud divergence (6.0×10^{-4} sec^{-1} or more) in the layer of cirrus outflow is likely to be associated with severe weather, such as heavy thundershower, hail, and tornados. Most of these active convective systems transport latent heat to the upper troposphere in magnitude at least one order higher than in a moderate thunderstorm.

Another interesting feature observed is the occurrence of severe weather in these identified clouds during the period when these cloud systems enter into a partial decay phase. This is clearly shown in the cloud divergence profile as a function of time.

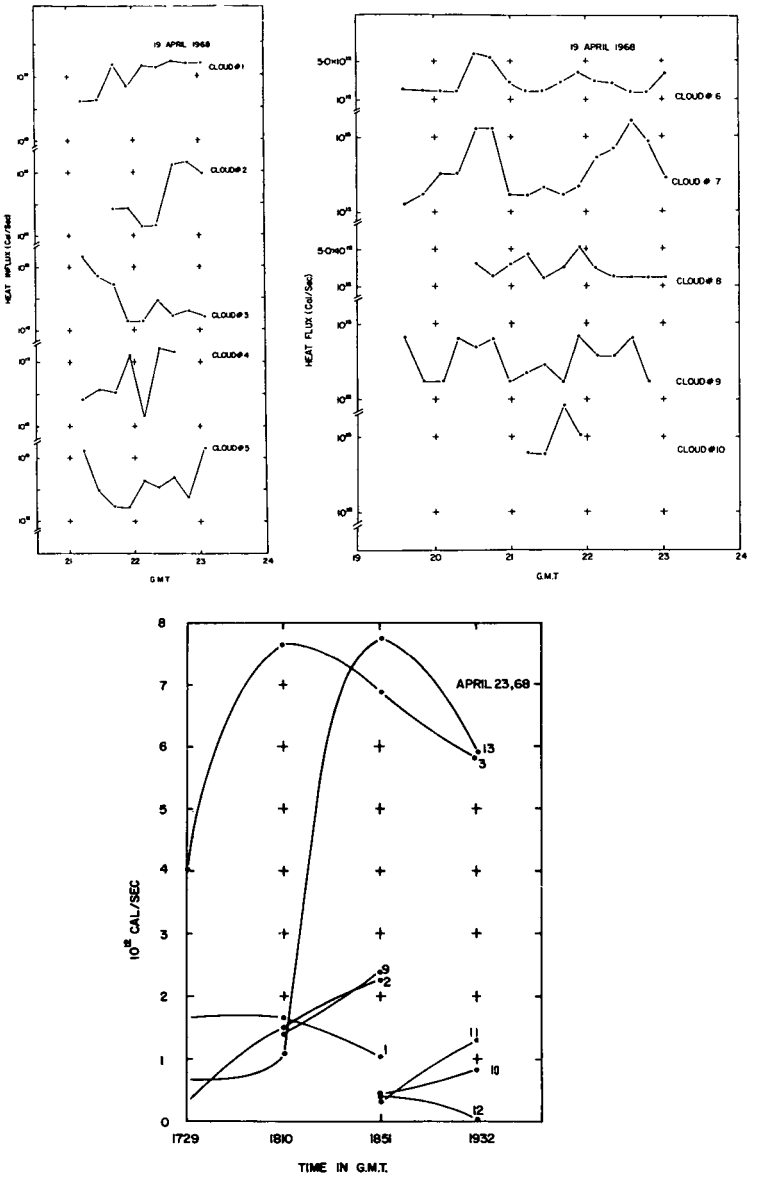

Fig. 9. Convective heat fluxes in severe storms as a function of time.

Future research

The magnitude of cloud divergence at the layer of cirrus outflow is also an indication of the character of vertical motion field in the embedded "hot towers." With the upward mass flux measurements available with the technique, one can estimate the average vertical motion field, provided the areas of the updraft core are known from the radar echoes or by some other technique such as image enhancement of the brightest portions of the photo.

An objective method of estimating the average vertical motion field in severe storms from the ATS-III photographs is being developed and will be communicated shortly. Since the vertical motion field in a storm system has a unique correlation with the rainfall rate, it may be possible to estimate the average amount of precipitation associated with this kind of growing cloud system.

Acknowledgment

The authors wish to thank Mr. Brian Auvine for measuring the cloud areas and procuring thermodynamic data for the 23 April case presented in this paper. Thanks are also due to Mr. Eric Smith, who programmed for the brightness contour display. This investigation was supported in part by the US Weather Bureau under Grant WBG 27 and partly by NASA under Grant 11542.

References

Anderson, C. E. 1960. "A study of the pulsating growth of cumulus clouds." Geophysical research paper no. 72. Air Force Cambridges Res. Lab., Mass., 136 pp.

Borovikov, A. M. et al. 1963. Cloud physics. U. S. Dept. of Commerce, Washington, D. C.

Braham, R. R. 1952. "The water and energy budgets of the thunderstorm and their relation to thunderstorm development." J. Meteor., 227-242.

Brown, R. A. 1967. "Mass and available energy in growing convective cloud." J. Atm. Sci. 24, 308-311.

Fujita, T. and Grandoso, H. 1966. "Split of a thunderstorm into anticyclonic and cyclonic storms and their motion as determined from numerical model experiments." SMRP research paper no. 62, University of Chicago.

Higuchi, K. 1965. "A three-dimensional study of cumulus cloud by the use of aerial photographs of the clouds and their shadows." J. Atmos. Sci. 22, 440-447.

Ludlum, F. H. 1966. "Cumulus and cumulonimbus convection." Tellus 8, 4, 687.

Sikdar, D. N. 1969. "Convective heat transport over the tropical mid-Pacific as estimated from a geosynchronous satellite altitude." Ph. D. thesis, The University of Wisconsin, Madison, Wisc.

Sikdar, D. N. and Suomi, V. E. 1968. "An objective technique of evaluating tropical mesoscale heat transport in the tropics from geosynchronous satellite photographs." Studies in atmospheric energetics based on aerospace probings. 1968 Annual Report, Department of Meteorology, The University of Wisconsin, Madison, Wisc.

US Government Printing Office, 1949. The Thunderstorm. Washington, D. C.

US Department of Commerce, 1968. Storm Data, vol. 10, 4.

A DEMONSTRATION OF THE INTERCONTINENTAL DISSEMINATION OF GRAPHIC METEOROLOGICAL DATA UTILIZING TELECOPIERS AND RADIO TELEPHONY

J. A. Weinman, R. C. Grosh
Department of Meteorology
S. D. Ellington
W9YT
University of Wisconsin
Madison, WI 53706 U. S. A.

R. Calheiros
Fundaçao Educacional de Bauru
G. Ferraz
PY20Y
Bauru, Sao Paulo, Brazil

C. W. van Scherpenzeel
Meteorologische Dienst v. Suriname
E. Dijra
PZ1AK
Paramaribo, Suriname

INTRODUCTION

The time scale which frequently characterizes meteorological phenomena in the tropics may be of the order of a day or less. Geosynchronous satellites provide numerous pictures of clouds in the tropics each day. It is desirable to send these pictures in real time to those most directly affected by tropical weather. Unfortunately rapid communications channels are not always available for this purpose. The test described below demonstrates the feasibility of exchanging graphic data, such as cloud photographs, between North and South America by means of amateur radio equipment and Telecopiers.

INSTRUMENTAL CONSIDERATIONS

The recent development of the Telecopier III by the Xerox Corporation[1] renders it feasible to transmit documents smaller than 21.6 cm. × 28.0 cm. by means of communications systems used for voice transmission, viz. telephones

[1] Xerox Corporation, Xerox Square, Rochester, New York, USA.

or amateur radio. Such pictures can be transmitted in about five minutes.

The Telecopier III, shown in Figure 1, is a portable machine measuring 16.5 cm. × 50.5 cm. × 40.5 cm, and it weighs 11.3 kg. The Telecopier used in this test transmission was easily transported as hand luggage between Madison and Bauru by airplane and various automobiles and buses.

The Telecopier operates on 110v., 60Hz. and it draws .5 amps. Its power consumption, size and weight thus make it attractive to utilize the present communication scheme aboard ships, aircraft and at remote stations.

The picture produced by the Telecopier consists of a raster of 19.7 lines/cm. which burns black or grey lines into specially treated paper. The picture resolution is thus comparable to that of a television picture. The Telecopier produces pictures with six shades of grey. This contrast is comparable to that which is found in newspaper pictures.

The Telecopier signal is a frequency-modulated audio frequency carrier. The picture may therefore be transmitted over voice-quality radio transmitting equipment. The audio signal level from the Telecopier is very high; care must

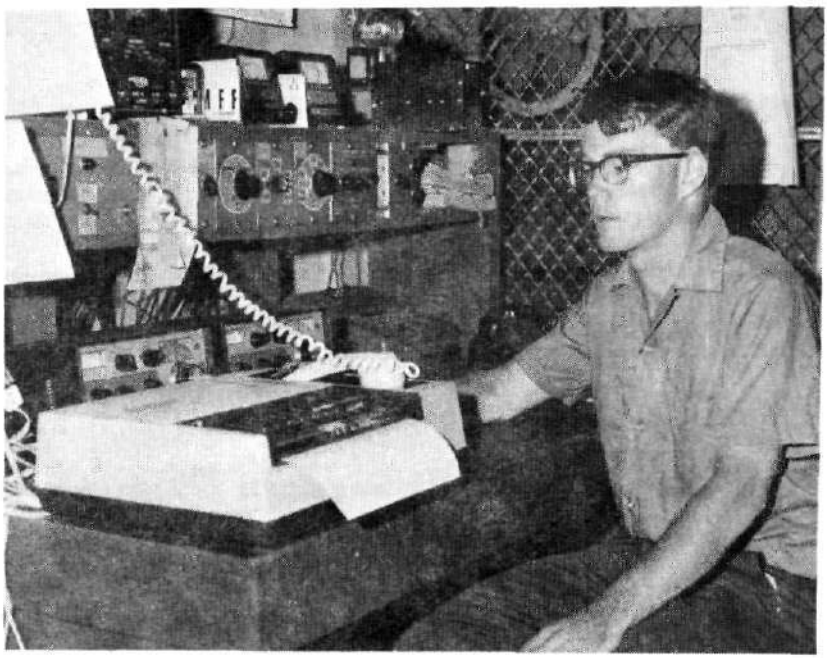

Fig. 1. The Telecopier III is shown connected to the transmitter of W9YT.

therefore be exercised not to damage linear amplifiers and other transmitting equipment. The Telecopier signal should not be transmitted with equipment rated only for intermittent voice operation.

Any amateur, single sideband receiver with a nominal 3 k Hz bandwidth seems to be sufficient to receive Telecopy pictures. Although care should be taken to tune the receiver, a small frequency error (less than 200 Hz) does not seem to degrade the picture quality. Strong signals are necessary for clear pictures because interference from other stations appears to be the greatest source of picture degradation.

RESULTS

Figure 2 shows the results of our first transmission, conducted on August 27, 1970, from Madison, Wisconsin (USA) to Bauru, Sao Paulo (Brazil). The transmission was conducted at 21 MHz, signal strength was S-8 to S-9, and propagation conditions were normal.

It is instructive to compare the picture of South America as viewed by ATS III, which was transmitted from Madison, with the picture of the east coast of Brazil received by the APT receiving equipment at the Fundaçao Educacional de Bauru. The dashed lines mark the area which was observed by the ESSA satellite. The lower picture shows the Telecopy of this ATS III picture received by PY20Y in Bauru. Both APT and ATS III pictures show the stationary front over Sao Paulo and Guanabara. The coastal clouds over Espirito Santo and eastern Bahia are visible, and the cloud-free region over Minas Gerais and western Bahia is also evident on all pictures. Note that the original pictures were of better quality than the third-generation copies shown in this figure.

The ATS III satellite produces pictures with spatial resolution between 3 km. and 12 km. Enlargements of parts of the global pictures therefore yield data on mesoscale phenomena such as showers from cumulus congestus clouds. Figure 3 shows a detailed view of Suriname obtained on September 13, 1970. The crosses represent intersection of 1° increments in latitude and longitude.

Because the Telecopier grey scale response is limited to six shades, and because the density of a photograph is not a linear function of brightness, it may be desirable on occasion to transmit maps which present the voltage output of the satellite camera signal. An isodensitracer circuit[2] with a nonlinear response was therefore constructed. The response of this circuit is linear for

---

[2] A detailed description of the isodensitracer circuit will be found in the M. S. thesis of R. C. Grosh.

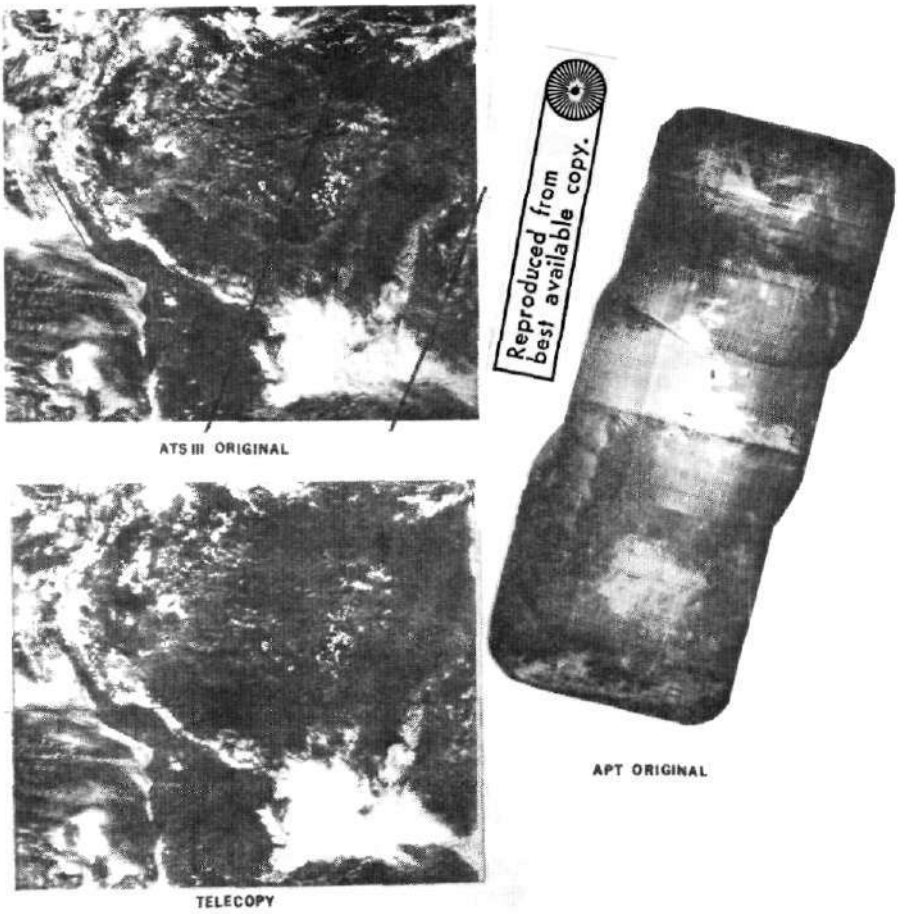

Fig. 2. Comparison of pictures of South America on 27/8/70 viewed by the ATS III satellite. This picture, transmitted from Madison, Wisconsin, is compared with the picture obtained from the Telecopier connected to the receiver of PY20Y in Bauru. The picture obtained from the APT is also shown for comparison. The dashed lines bound the area observed from the ESSA satellite.

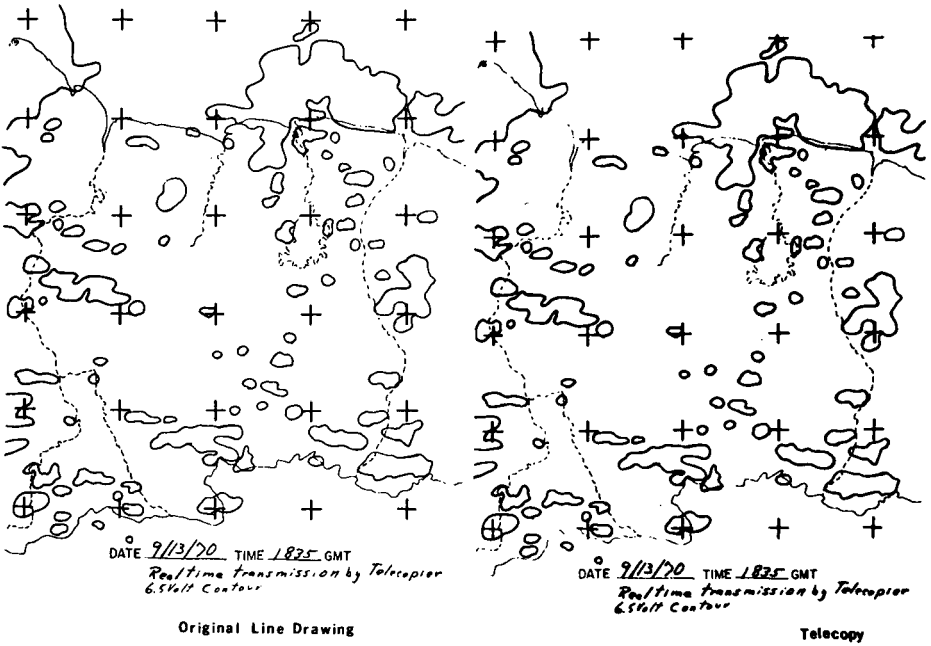

Fig. 3. Close-up view of Suriname on 13/9/70 derived from an ATS III picture. The isophots delineate regions covered by clouds whose brightness produced a signal greater than 6.5 volts.

low brightness objects such as landmarks reasonably flat, and insensitive for moderately bright objects such as cumulus humilis clouds, and it yields a very bright output signal when the input signal exceeds a predetermined voltage. Isophots corresponding to satellite camera signal voltages exceeding 6.5 volts are shown in Figure 3. It is noteworthy that Paramaribo Suriname (shown as a dot near 6°N 55°W) was subjected to a "Sibiboesi" storm at the time that the picture was taken; v mm. of rainfall were measured in Paramaribo. The area was obviously covered by bright clouds.

Figure 3 shows the original map and the copy received in Paramaribo by means of the Telecopier and the receiver of PZ1AK. The transmission was conducted at 21 MHz, signal strength was S-8 to S-9, and propagation conditions were reasonable. This test demonstrates that line drawings with good clarity can be transmitted by radio. Although we have confined our tests to the transmission of ATS III pictures, weather maps could also be distributed in this manner.

The Telecopy pictures were received in Bauru and Paramaribo a few hours after they were taken by the ATS III satellite. If such picture transmission could be conducted regularly, the delay could be reduced to one hour.

In order to illustrate the feasibility of two-way picture communication by this method, a letter of greetings was sent from Bauru back to Madison. The original letter and the received copy are shown in Figure 4.

CONCLUSION

We have demonstrated that it is technically feasible to send graphical meteorological data over great distances by means of conventional amateur radio and office copying equipment. The cost of such equipment, and the quality of the pictures obtained, compare favorably with other methods currently in use. We believe that the relatively modest cost and simplicity of the apparatus required to receive these pictures should enable meteorologists located in remote areas to obtain necessary data.

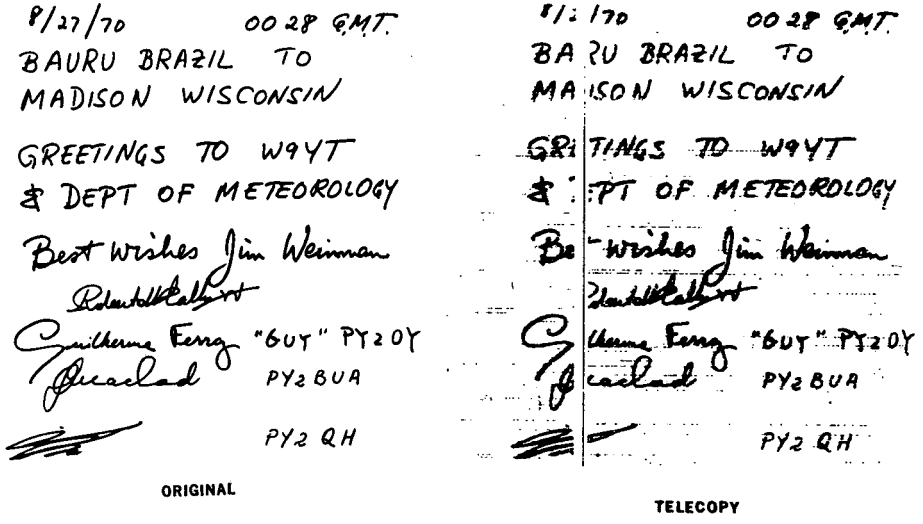

Fig. 4. Test transmission from Bauru to Madison which illustrates the feasibility of two-way graphical communication.

ACKNOWLEDGMENTS

We would like to express our thanks to Messrs. Art Boyars, and Stan Burns of W9YT who helped us establish the necessary radio links. We also wish to acknowledge the assistance of Messrs. Terry Schwalenberg and Dave Cadle whose efforts made it possible for us to obtain the ATS III pictures.

The Telecopiers were provided by Mr. H. Johnson of the Xerox Corporation; we hereby express our gratitude for his cooperation in this venture.

Funds for this experiment were provided by Fundaçao de Amparo a Pesquisa do Estado de Sao Paulo, the United States National Science Foundation and National Aeronautics and Space Administration and the Graduate School of the University of Wisconsin. We would like to thank these agencies for their support.

THE RADIATION BALANCE OF THE EARTH-ATMOSPHERE SYSTEM DURING JUNE AND JULY 1969 FROM NIMBUS III RADIATION MEASUREMENTS: SOME PRELIMINARY RESULTS

E. Raschke (Ruhr-Universität Bochum, F. R. G.)

T. H. Vonder Haar (University of Wisconsin, Madison, Wisconsin, USA)

W. R. Bandeen and M. Pasternak
(NASA, Goddard Space Flight Center, Greenbelt, Md., USA)

Abstract:

The meteorological satellite Nimbus III, launched on 14 April 1969, carries a five-channel medium resolution radiometer, whose measurements cover at least a period of one full year. In four channels the outgoing longwave radiation is being obtained in narrow spectral ranges (6.5 - 7.0 μm, 10 - 11 μm, 14.5 - 15.5 μm, 20-23 μm. Thus, the total outgoing longwave radiation (5 - 50 μm) was inferred from these spectral measurements by a multiregression method employing limb-darkening relations derived by a statistical study of Nimbus II measurements (5 - 30 μm). The albedo was inferred from measurements in the spectral range from 0.3 to 4.0 μm considering two empirically derived angular dependence relations, one over clouds and land, and the other over oceans through clear skies.

Data from periods 16 to 30 June 1969 and 1 to 15 July 1969 yield a mean planetary albedo between 29% and 30% and a mean planetary temperature between 252° to 253°K which corresponds to outgoing fluxes between 0.330 and 0.338 ly min^{-1}. Both results are in good agreement with results found from Nimbus II measurements of the same semimonthly periods in 1966.

Introduction

The average structure of the earth's radiation fields in the shortwave and longwave region is generally known from extended experimental studies with satellite measurements [1] and from empirical computations based on aero-

logical and climatological data [2]. However, highly resolved geographical distributions during periods of the order of one month were obtained only from Nimbus II radiation data over a short period of 2 1/2 months. Interannual variations of the latter results and their relation to atmospheric energetics could not be studied so far. Only satellite measurements with self-integrating radiometers provided studies of the earth's radiation fields over periods of several (up to five) years [4]. The time resolution was of the order of one season and the spatial resolution in geographical maps was about 1000 km × 1000 km^2.

Since April 1969 the Nimbus III satellite provides reliable measurements. Their analysis will enable detailed descriptions of earth's radiation fields over the period of at least one year. Such a large data analysis is not yet finished, but some preliminary results will be presented in this paper.

Evaluation Procedure and Results

The radiation measurements of Nimbus III are being made with a five-channel scanning radiometer similar to the one flown previously on Nimbus II. Thus, principle elements of the evaluation technique used in earlier evaluations of Nimbus II data [3] could be used in this analysis. Since measurements of only one satellite in a sunsynchronous orbit were available for this analysis, the results might be slightly biased over areas with pronounced diurnal variations of cloudiness.

Albedo

The albedo of an area is defined in this study to be the ratio of daily averages of reflected to incoming flux of solar radiation. For computations of the latter quantity, a value of $S_0 = 1.95$ cal cm^{-2} min^{-1} has been chosen for the solar constant ([5], [6]). Daily averages of the flux of reflected solar radiation were obtained by integration over the entire daylight period where the dependence of the directional reflectance, r, on the sun's zenith angle is taken into account with a relation derived empirically from airplane, satellite and balloon measurements. Here two different relations have been applied to areas of high reflectance (clouds or land) and low reflectance (cloud-free ocean). These two relations are shown in Fig. 1 and, compared with that, one used in earlier work with Nimbus II data. The slope of the curve labelled "ocean" is much steeper than of the two others; thus it can be expected that albedo values obtained of oceanic areas will be slightly higher than those from Nimbus II data. On the other side, albedo values over extended land, clouds and snow cover will be somewhat lower. An example of results, a map of the mean albedo during the period 16 to 30 June 1969, is shown in Fig. 2. The patterns in this map clearly reveal the location of areas of high cyclonic activity whose cloudiness causes albedoes of more than 40%. The albedo over subtropical oceans whose cloudiness is very low is about 2% to 3% higher than it was found from Nimbus

II data while the albedo of the Sahara and Arabian desert areas was found 3% to 4% lower. Global averages are compared below in Table 1.

Outgoing longwave radiation

The total radiance of outgoing longwave radiation was calculated from simultaneous measurements of four channels (6.5 - 7 μm, 10 - 11 μm, 14.5 - 15.5 μm, 20 - 25 μm). Each of these four measurements may be assumed to be representative of the mean water vapor content of the upper troposphere, the surface temperature, the lower stratospheric temperature and the lower tropospheric water vapor content, respectively.

A multiregressional relation has been derived from calculated radiances of eighty different atmospheric models, which relates the total radiance to these filtered radiances. The correlation between independently calculated total radiances and those from this formula is nearly complete (Fig. 4) and the standard error of estimate is less than 1.5% of the total radiance even over very cold areas ($N < 50$ W cm^{-2} ster^{-1}). The limb-darkening of the earth-atmosphere system in the infrared has been taken into account with simple relations derived from Nimbus II measurements.

In Fig. 3 is shown the geographic distribution of the mean out-going longwave radiation during the period 16 to 30 June.

Radiation balance

The geographical distribution of the radiation balance or net radiation at the top of the atmosphere is shown in Fig. 4. Its pattern is similar to that found from Nimbus II data. Except over parts of Sahara, Greenland and the Arctic ice shield the northern hemisphere at this season (north-summer) absorbs more solar radiation than it loses by emission to space. The southern hemisphere is the major deficit area. A similar geographical distribution has been found also for the period 1 to 15 July 1969.

Global budget

Global averages of daily means of incoming solar radiation, S, the albedo, A, the outgoing longwave radiation flux, E, and the radiation balance, Q, are summarized in the following table:

Table 1. Global Budget

	A [%]	S	E	Q
		cal cm^{-2} min^{-1}		
16 - 30 June 1966*	30.9	0.472	0.345	-0.016
16 - 30 June 1969	28.9		0.333	+0.002
1 - 15 July 1966*	29.8	0.472	0.346	-0.015
1 - 15 July 1969	29.4		0.337	-0.004

*for S_0 = 1.95 cal cm^{-2} min^{-1}

The global planetary albedo has been found from Nimbus III data to be 1% to 2% lower than 1966. This discrepancy may be due, partly, to some lower cloud cover, but it might be caused primarily by the different reflectance laws(Fig.1) used in these calculations. Also the outgoing longwave radiation has been found to be about 2.5% to 3% lower than in 1966. Here, again, the different limb-darkening relations might be responsible for this discrepancy. But also the assumptions necessary for the derivation of the multi-regressional relation which is being used to calculate the total longwave radiance from simultaneous measurements of four narrow-band channels can be responsible for it. A detailed error analysis will be published together with all results in a forthcoming article.

Concluding Remarks

The results from this study of the earth's radiation budget agree in general with those found for the year 1966. Together, the Nimbus data from satellites II and III thus far show the same features of large-scale energy exchange with space measured also by other satellite sensors. These results encourage further, more detailed evaluations as long as Nimbus III measurements will be available with sufficient accuracy.

References

1. Vonder Haar, T. Ph. D Dissertation, The University of Wisconsin (1969).

2. London, I. and Sasamori, T. Paper A. 2. 1, COSPAR XIII, Leningrad (1970).

3. Raschke, E. and Bandeen, W. J. Appl. Met., 9 (1970).

4. Vonder Haar, T., and Suomi, V. J. Atmos. Sci. (to be published, 1970).

5. Labs, D. and Neckel, H. Z. Astrophys., 69 (1968).

6. Drummonel, A., Hickey, T., Scholes, T., and Lave, E. Nature, 218 (1968).

Note: We thank all who contributed to the success of the satellite experiment, especially Mr. A. McCulloch, Mr. H. Powell and Mr. J. Barksdale. Part of this work was supported by NASA under contract NAS5 - 11542.

FIGURE 1

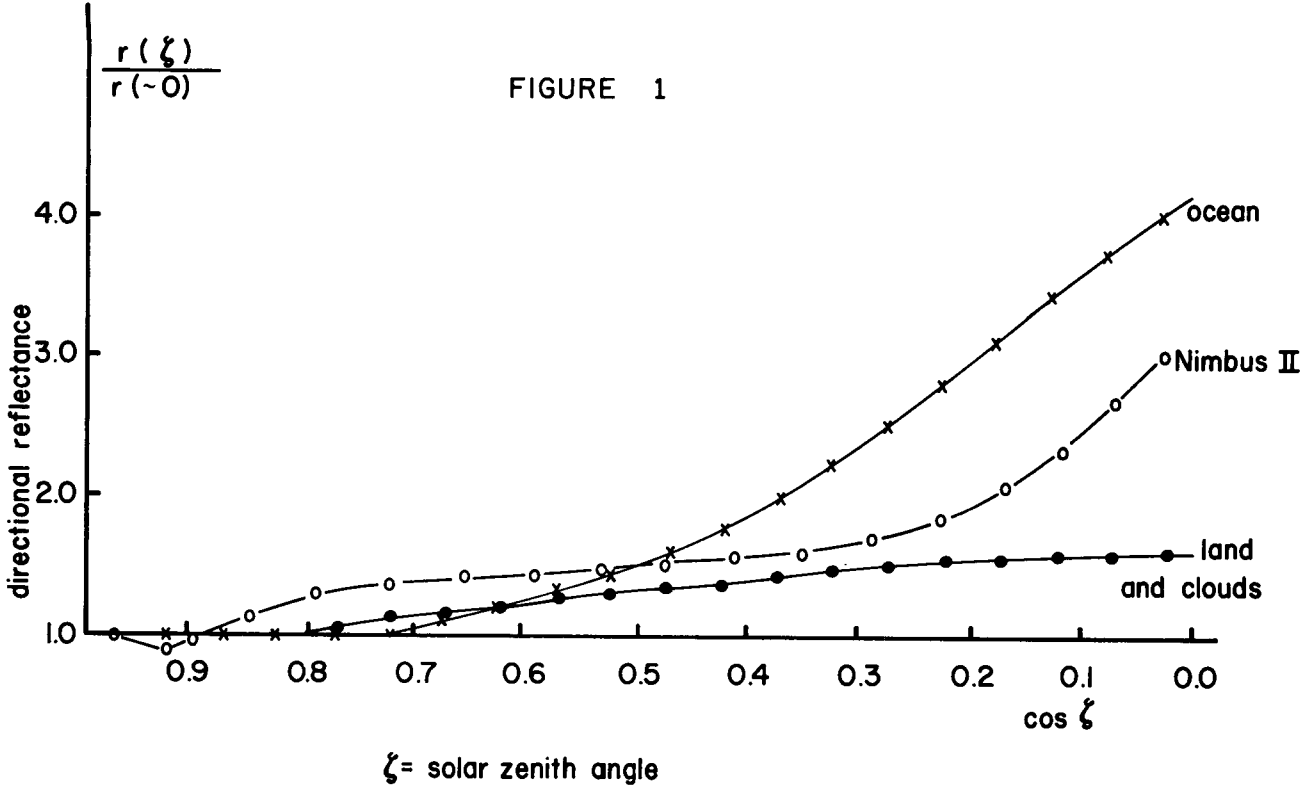

ζ= solar zenith angle

ALBEDO (%)

NIMBUS III, 16-30 JUNE, 1969

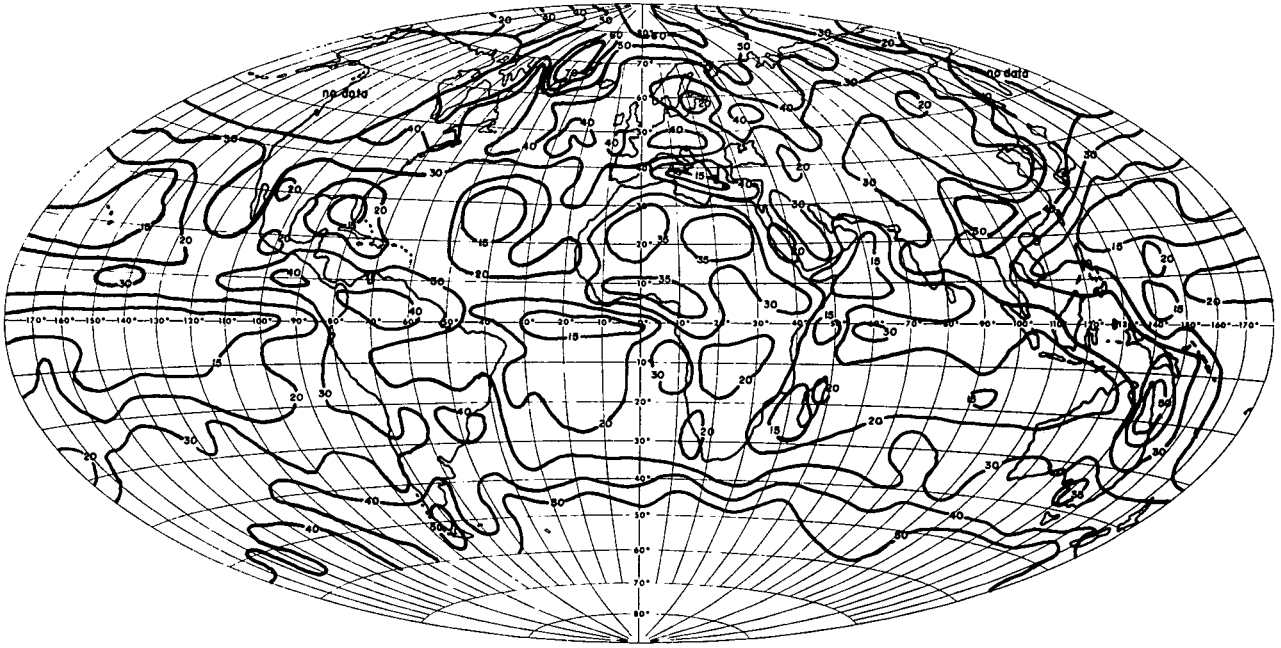

FIGURE 2

OUTGOING LONGWAVE RADIATION (cal $cm^{-2} min^{-1}$)

NIMBUS III, 16-30 JUNE, 1969

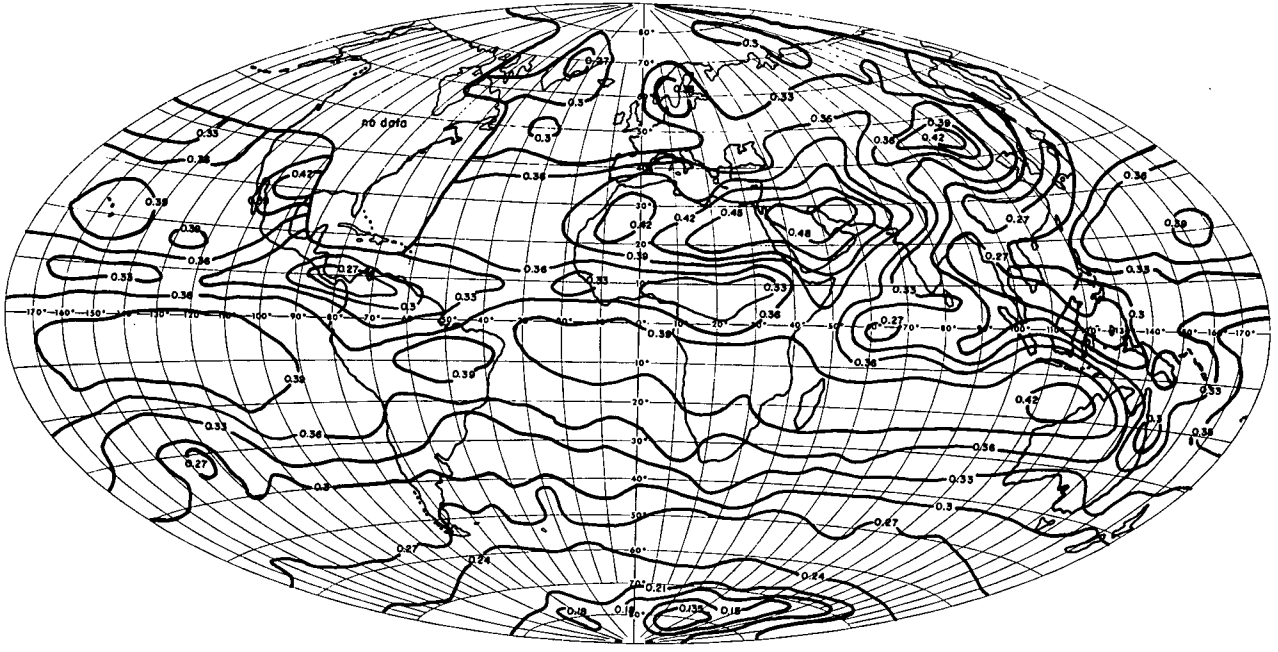

FIGURE 3

RADIATION BALANCE (cal cm^{-2} min^{-1})
NIMBUS III, 16-30 JUNE, 1969

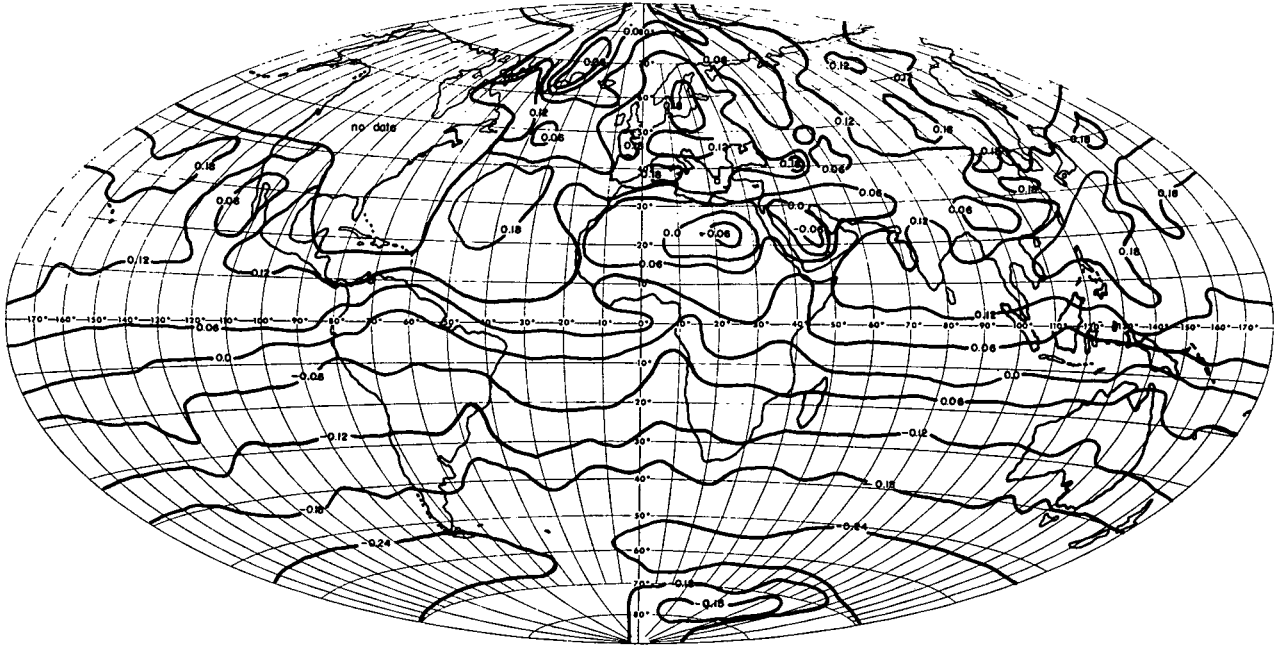

FIGURE 4

APPLICATION OF SIMULTANEOUS INFRARED RADIATION MEASUREMENTS AND CLOUD PHOTOGRAPHS FROM SATELLITES

Thomas H. Vonder Haar

Introduction

It is well recognized that sensors on meteorological satellites return vast amounts of measurements, although meteorological information in these data can often be as well hidden on a magnetic tape or reel of film as in nature itself. In addition, scientists often wish to study satellite measurements over relatively large time and space scales (i.e., time periods greater than one day and spatial coverage approaching global extent). Since such studies always require the piecing and fitting of many individual information bits, methods which lucidly present large numbers of measurements are important to users.

As we begin our second decade of the meteorological satellite program with the second generation of operational meteorological satellites (ITOS), much of the satellite data processing problem has already been overcome. Bristor et al. (1966) routinely process the reflected solar radiance measurements (photographs) from the advanced vidicon camera systems on the ESSA satellites. They have similar computer mosaic methods for ATS satellite spin-scan camera measurements and for ITOS scanning radiometer data. Examples of the use of the ESSA satellite products are discussed by Booth and Taylor (1969) and Taylor and Winston (1968).

Even before the computer methods were finalized, Kornfield et al. (1967) developed an economical multiple-exposure photographic method to "average" the ESSA satellite photographs. Such averages aid in the study of longer time periods of observation and have been used extensively for research (Kornfield and Hasler, 1969) and for educational purposes. In addition, since 1966 the ATS satellites (in geosynchronous orbits) have provided nearly continuous views of cloud conditions during the daytime over a large portion of the earth (Suomi and Vonder Haar, 1969). From these measurements (and to a lesser extent from once-a-day ESSA data) time-lapse movies can be made to display the observations of development and change of meteorological situations. Chang (1970) has shown a semiobjective technique that allows study of time variations over limited areas without use of the movies.

All of the above methods and others allow the daytime satellite measurements of reflected solar energy to be used in a practical way for various applications. This note discusses the addition of even more meteorological information to the photographic output of these techniques. It presents an analysis of infrared (IR) radiation measured at nearly the same time as the cloud photographs were obtained. Superposition of these two types of measurements on the same map base aids their mutual interpretation. The IR data add a gross estimate of the height and/or type of clouds shown by bright areas on the photographic cloud averages.

Such a combination has been demonstrated previously. Bandeen (1962) reviews work of Fujita who had used such a joint analysis on the synoptic scale. Dittberner (1969) notes its usefulness for his study of seasonal variations of the Asiatic summer monsoon. This note, however, emphasizes application on a global scale and for relatively long time intervals. Since simultaneous high-resolution longwave and shortwave measurements will be available from the present ITOS satellites and from the coming SMS (Synchronous Meteorological Satellite), the example in this report is essentially a preview of global satellite data processing possibilities in the near future.

Global analysis of infrared radiation on a photographic cloud average

As indicated, the data were obtained by using measurements from two satellites, the vidicon camera output from ESSA-IX and the total IR radiant emittance derived from a scanning radiometer on Nimbus-III. The ESSA-IX measurements were obtained from the National Environmental Satellite Center in the form of mosaics on a Mercator base. For the same fifteen-day period (16 to 30 June 1969) the infrared values* were obtained as part of a separate study of the earth's radiation budget.

During this time period the satellites were both in near-polar, sun-synchronous orbits with ascending nodes near local times of 1130 and 1430, respectively, Nimbus being the former. The vidicon system on ESSA made only daytime measurements while the IR pattern contains both day and night measurements (near local noon and midnight over the area shown). The infrared analysis was drawn independently of the photographic cloud average.

In order to aid interpretation of a sample measurement set, Fig. 1 illustrates a simple version of the four major physical situations encountered in a simultaneous longwave and shortwave radiation analysis. It shows the

*The absolute values of the infrared data are in preliminary form pending routine checking of the data tapes and technique of reduction. This fact does not significantly affect their use in the present study.

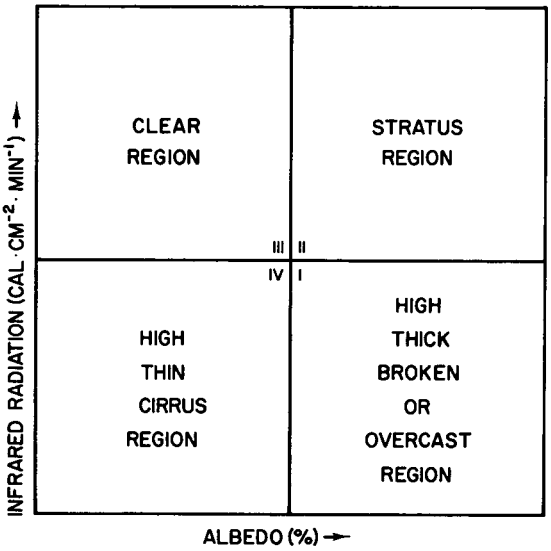

Fig. 1. Simple depiction of relation between infrared radiation, albedo (normalized reflected solar radiation), and condition of earth-atmosphere scene viewed from a satellite (after Dittberner, 1969).

possible qualitative combinations of a scene (clouds and/or surface) that may be warm, cold, bright or dark. Of course, for special cases such as bright desert or ice, the simple picture is not valid.

Figure 2 displays measurements from all longitudes from 35N to 30S. The cloud depiction is continuous but the IR data show gaps in regions of poor coverage. All dark (relatively cloud-free) regions show high values of outgoing IR radiation. These include the southwestern United States, subtropical high pressure regions in both the Atlantic and Pacific in both hemispheres, northwest Australia, and the Brazilian central plateau. Of these, the outgoing radiation is highest near the United States and Australia, indicating not only cloud-free conditions during 16 to 30 June, but also the probability of low atmospheric water vapor content. Considering the dark subtropics of both hemispheres overall, the IR emission is generally greater in the Southern Hemisphere.

The highest value of outgoing radiation (0.48 cal cm^{-2} min^{-1}, effective blackbody temperatures of 4C) is measured over the eastern Arabian peninsula and Persian Gulf. This region is not one of the darkest on the cloud average because it is largely desert sand and rock. From the IR data, however, we can note this region as being significantly cloud-free and dry. To a lesser

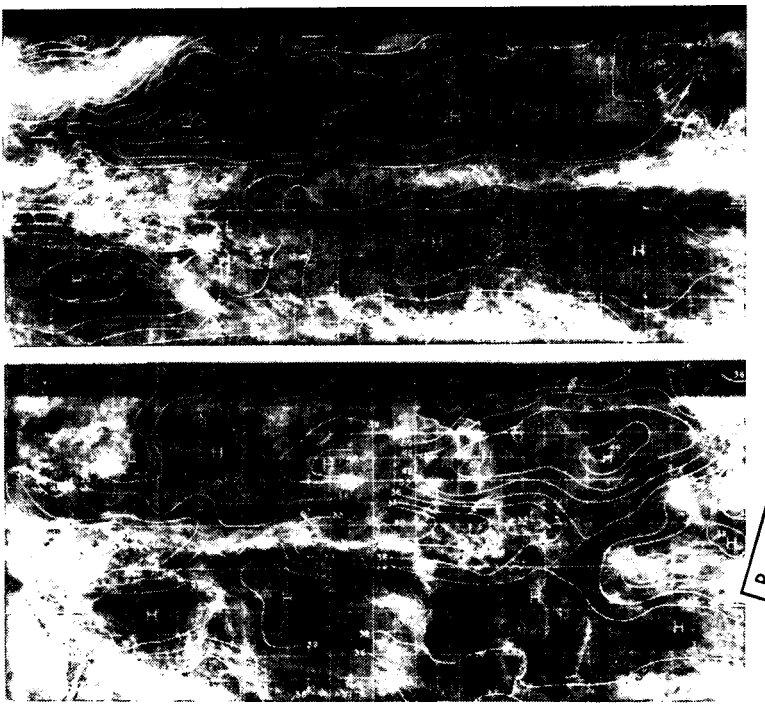

Fig. 2. Analysis of total infrared radiant emittance (10^{-2} cal cm^{-2} min^{-1}) measured with the MRIR on Nimbus-III superimposed on a photographic cloud average obtained from ESSA-IX measurements over the same 15-day period (16-30 June 1969).

extent, the same relationships are apparent over the central Sahara.

Since no ice-covered regions are included in the portion of the earth shown in Fig. 2, the brightest areas on the cloud photo-average indicate regions of persistent, nearly overcast cloud conditions. These include areas off the west coasts of South and Central America; the region of the Asiatic summer monsoon over eastern China and Japan; throughout the Indonesian region; in the south-central Pacific; and into the South Atlantic from southern Brazil and across the northwest portion of the South American continent.

The infrared data allow a quantitative intercomparison of these various "bright" regions. They show, for example, that the lowest values of IR

emission (0.24 cal cm^{-2} min^{-1}, effective temperature -40C) are measured from the narrow band of clouds over the East China Sea. This low value indicates persistent middle and high clouds, which is consistent with an analysis by Wagner (1969) who reports that there was an abnormally strong jet stream over this area during June 1969. At the other extreme, the very bright region west of Chile shows no infrared minimum, indicating the presence of warm low stratus clouds found over the cold ocean current of that area. Additional regions of extensive high and middle cloud can be inferred over Columbia and the intertropical convergence zone (ITCZ) just to the west, in the Bay of Bengal, and throughout the "subtropical front" extending southeast from Indonesia.

Considering IR measurements over the areas of medium brightness on the photo, we note indications that (except for the extreme eastern Pacific) the ITCZ across the Atlantic was "stronger" than its counterpart in the Pacific. The IR values are generally lower in the Atlantic. Both of these convergence zones are located between 5-10N. With the aid of the infrared it is seen that the strongest equatorial convergence during 16 to 30 June 1969 existed directly on and to the south of the equator in the Indian Ocean.

Further scan of Fig. 2 shows that two regions of nearly the same brightness, off the west coast of South Africa and northeast of Puerto Rico, can be easily separated in the infrared. The former is warm stratus, the latter is measured colder. Wagner notes that a number of weak disturbances and waves moved from this region during June, thus giving a plausible explanation for the presence of high and middle clouds indicated by the infrared. Over the Solomon Islands region we observe relatively low values of IR radiation over a relatively dark area on the cloud photograph. Such a combination indicates a region of persistent cirriform cloudiness, a type generally transparent to the solar energy, but effectively opaque to IR energy from the warm ocean below.

Summary

The use of computer-produced or photographically averaged cloud depictions based on satellite measurements of reflected solar energy is a powerful method to condense a great deal of meteorological information into a lucid presentation for research and for education. When simultaneous measurements of IR radiation are superimposed on such a cloud depiction the usefulness is increased for both applications and most probably for operational use as well. Although the present study treats only total spectrum measurements, the extension of the methodology to selected spectral intervals may offer special advantages (e.g., the "window" radiation near 11 μm and the near-IR regions for pollutant detection). From current and future meteorological satellite measurements, such simultaneous analyses will be possible over a wide range of space and time scales.

Acknowledgments

E. Raschke, M. Pasternak and W. Bandeen are collaborating with the author in the use of Nimbus-III data. Their efforts and those of others at NASA were important to this study. D. Cadle and D. Otto of the Space Science and Engineering Center performed the photographic processing. This work was sponsored by NASA under Contract NAS5-11542.

References

Bandeen, W. R., 1962: "Data processing from meteorological satellites." NASA Rept. SP-16, 23-31 (available from Superintendent of Documents).

Booth, A. L., and Taylor, V. R., 1969: "Mesoscale archive and computer products of digitized video data from ESSA satellites." Bull. Amer. Meteor. Soc., 50, 431-438.

Bristor, C. L., Callicott, W. M., and Bradford, R. E., 1966: "Operational processing of satellite cloud pictures by computer." Mon. Wea. Rev., 94, 515-527.

Chang, C. P., 1970: "Westward propagating cloud patterns in the tropical Pacific as seen from time-composite satellite photographs." J. Atmos. Sci., 27, 133-138.

Dittberner, G. J., 1969: "A study of the Indian monsoon using satellite-measured albedo and longwave radiation." M. S. thesis, Department of Meteorology, The University of Wisconsin, Madison.

Kornfield, J., Hasler, A. F., Hanson, K. J., and Suomi, V. E., 1967: "Photographic cloud climatology from ESSA III and V computer produced mosaics." Bull. Amer. Meteor. Soc., 48, 878-883.

_____, and Hasler, A. F., 1969: "A photographic summary of the earth's cloud cover for the year 1967." J. Appl. Meteor., 8, 687-700.

Suomi, V. E., and Vonder Haar, T. H., 1969: "Geosynchronous meteorological satellite." J. Spacecraft Rockets, 6, 342-344.

Taylor, V. R., and Winston, J. S., 1968: "Monthly and seasonal mean charts of brightness from ESSA III and V digitized pictures, Feb. 1967-Feb. 1968." Tech. Rept. No. 46, Nat'l Environmental Satellite Center, ESSA, Washington, D. C.

Wagner, A. J., 1969: "The weather and circulation of June 1969—A predominately cool and wet month." Mon. Wea. Rev., 97, 684-690.